UCLouvain

epl

École polytechnique de Louvain

A backpack-like balance assistance device using CMG technology

Proof of concept

Author: **Cyril GRANCITELLI**
Supervisor: **Renaud RONSSE**
Readers: **François HEREMANS, Benoît RAUCENT**

Academic year 2020–2021
Master [120] in Electro-mechanical Engineering

Contents

Chapter 1

Introduction

In 2015, the World Health Organization reported that by 2050 the population of elderly aged 60 and over will increase from 900 million to 20 billion. From this population, $28-35\%$ will occur a fall each year which can have severe consequences as anxiety to walk, reduced life satisfaction, and limited mobility but also physical like a head trauma or a hip fracture [1]. Someone suffering from the latter injury has 25% of chance of dying between 6 to 12 months [2]. Despite the human factor, a fall should cost approximately 30,000 Dollars to the hospital. It takes into account the medical staff but also the longer rehab time for the elderly that occupies as room [3].

A fall can come from diverse origins such as osteoporosis, muscle weakening and neurological conditions that impair some abilities. From walking gait analysis, abnormalities linked to neurodegenerative diseases responsible for 66% of the falls can be detected [4].

Therefore, to preserve the elderly health, it is urgent to reduce the number of falls. Several technologies exist such as exoskeletons like ReWalk [5] or Ekso RN [6] that are used in a controlled environment as rehab devices. But recently, a team at the University of Delft in the Netherlands led by Prof. Vallery work on designing a backpack-like walking assistance device using Control Moment Gyro (CMG). The latter are well-known for their use in spatial applications for agile control. Compared to the reaction wheel, for the same amount of power this technology can deliver a way bigger output torque [2].

The aim of this master thesis is to assess the developed technology with the information given in the published papers. To verify the capability of this technology, the objective is to design a down-scaled inverted pendulum mounted with a CMG modeling the human body. The main specification for this system is to weight ± 1 kg. In this work will be presented the designed control law as the mechanical dimensioning. This process required the derivation of the dynamical equations of the system and the use of dynamical scaling relation.

Chapter 2

Walk dynamics and the causes leading to falls

To design such an assistance device, one must first understand the walking biomechanics and its gaits to understand the mechanical and neurological failures leading to a fall. This is useful to implement and detect incipient falls to extract the torque at stake for the system to design.

2.1 Walking dynamic

Walking is a cyclic process with two distinct phases. The first one, called the *Stance phase*, corresponds to the time when the foot is in contact with the ground, while the portion of time where the leg is swinging is called the *Swing phase*.

The transition between those two phases is characterised by two events. The first one is when the heel enters in contact with the ground and is called *Left or Right heel contact*, at that time the leg switch from the *Swing phase* to the *Stance phase*. The second event occurs when the toe is lift off the ground and is called *Left or Right toe-off*, at that time the leg switch from the *Stance phase* to the *Swing phase*. The illustration of those phases for someone walking at constant speed and on level ground is depicted in Fig.2.1. One can see that most of the time the legs are in different phases except for a small duration where the weight is transferred from one leg to the other and both are in stance [7]. Also, one can observe that the *Stance phase* lasts longer than the *Swing phase*, the distribution is respectively 60% and 40% of the total cycle time [8].

To achieve those movements, our body requires the excitation of five distinct groups of muscles where each one will be involved in a specific movement; the

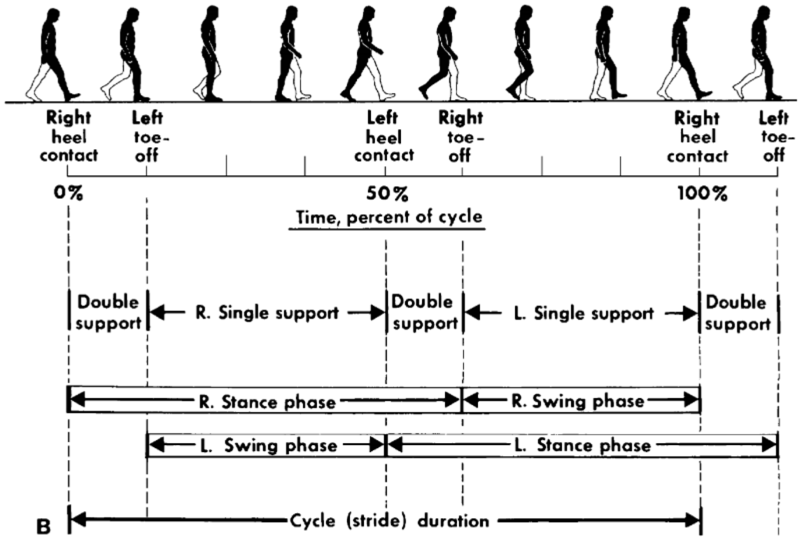

Figure 2.1: Illustration of the walking cycle on a straight line at constant speed where the left and right limbs are depicted in white and black respectively. A leg cycle can be divided into two specific phases, the *Stance phase* when the foot is touching the ground and the *Swing phase* when the leg swings freely in the air. The transition from one phase to another happens either when the heel enters in contact with the ground, *Left or Right heel contact*, or when the toe is lifted off the ground, *Left or Right toe-off.* While walking, the body will either be supported by a single leg or by both. [7]

pelvic rotation, the pelvic tilt, the knee flexion for the leg, and the ankle and toe flexion.

Those five degrees of freedom and the ability of muscles to act like dampers allow a person to walk smoothly with very little oscillations of the center of mass along the frontal plane while walking. Moreover, it was observed that while walking at constant speed on level ground along a straight line, there was no back and forth movement of the pelvic on the sagittal plane. Those observations are depicted in Fig.2.2 where the plot's axis is along the frontal plane and one can see that the center of mass oscillation follows an "8" pattern. The experiment was performed for 3 different walking speeds, $3.5\,km/h$, $5.1\,km/h$ and $6.2\,km/h$, for which one can see that the shape of the center of mass's oscillation is getting stronger and steeper as the velocity increase. Thus one can see that for a relatively high walking speed, $6.2\,km/h$, the vertical and horizontal oscillations are of more or less $4\,cm$ [7].

During stance, the leg muscles have three distinct tasks. They must ensure the

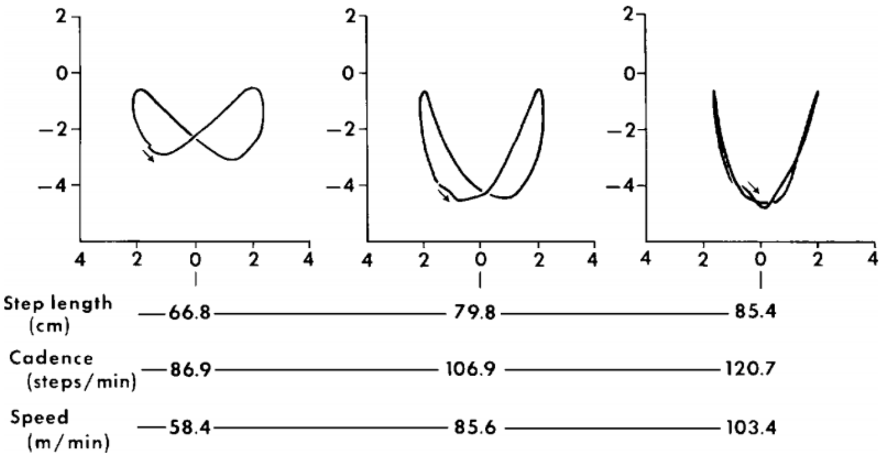

Figure 2.2: Oscillation of the center of mass in function of the walking speed along the frontal plane. Measurements of the center of mass position were performed at three different speeds, $3.5\,km/h$, $5.1\,km/h$ and $6.2\,km/h$. [7]

support of the body by counteracting the downward pull of gravity, they are also responsible for accelerating the body forward and for controlling the mediolateral balance at each step.

The first two functions are ensured by five muscles: the gluteus maximus, gluteus medius, vasti, soleus, and gastrocnemius. The three first account for the hip extension, hip abduction, and knee extension respectively during the first half of the stance. The ankle plantar-flexion is ensured by the 2 last muscles during the other half.

To understand muscle coordination during locomotion, the individual contribution of each of them must be studied [9]. Therefore, by measuring the contribution to the vertical, fore-aft, and mediolateral ground reaction forces of the five muscles at slow, preferred, and fast walking speed, it was highlighted that muscle coordination is affected by slower walking speed. As depicted in Fig.2.3, one can see that when the walking speed increase compared to the preferred velocity, the three functions allocated to the leg muscles during stance are ensured. On the other hand, when walking slowly, the hip and knee extensors (GMAX and VAS) are negligible in their role of support and deceleration of the center of mass. It is the hip abductor (GMED) and the limb posture (LP) that will ensure this support function. This shows that muscles coordination changes when humans walk slower than their preferred speed [10].

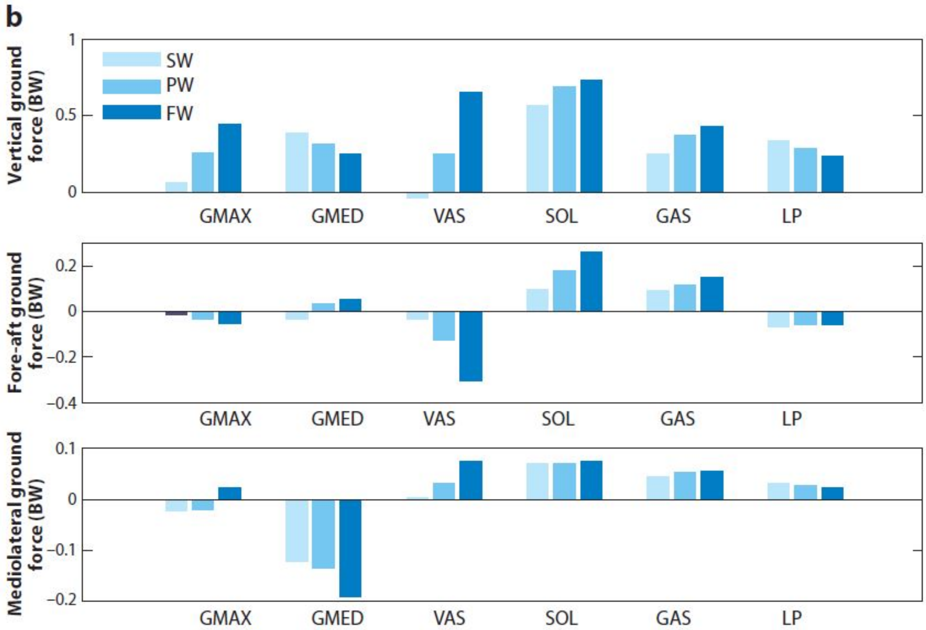

Figure 2.3: "Abbreviations: SW, slow walk; PW, preferred walk; FW, fast walk. (b) Peak contributions of selected muscles and limb posture (LP) to the vertical, fore-aft, and mediolateral ground reaction forces for slow walking (SW, 0.7 $[m/s]$), preferred walking (PW, 1.4 $[m/s]$), and fast walking (FW, 2.1 $[m/s]$). LP represents the contribution of all gravitational forces to the ground reaction force and describes the resistance to the downward pull of gravity provided by the bones and joints of the stance leg. Results are the mean of the calculated values obtained for five subjects. Muscle symbols: GAS, medial and lateral portions of gastrocnemius combined; GMAX, medial and lateral portions of gluteus maximus combined; GMED, anterior and posterior portions of gluteus medius/minimus combined; SOL, soleus; VAS, vastus medialis, vastus intermedius, and vastus lateralis combined. Data from Y-C Lin, M. Jancic, and M.G. Pandy, unpublished analysis." From [10]

2.2 Causes leading to falls

For a healthy elderly only affected by muscles fatigues and losses due to aging, one can foresee an increase of the instability and thus the risk of falling if the gluteus medius is not strong enough when the muscle coordination is changed. Therefore, maintaining a sufficient walking speed is primordial for older adults. From monitoring gait velocity, one can predict fall probability and adverse health events [11].

Nevertheless, a fall does not only occur when someone walks slowly but also from some neurological diseases impairing biomechanical functions. Gait abnormalities such as a reduced gait speed, step length, or poor postural balance can appear and might end up causing the person to fall. Some of the neurological conditions exhibit characteristic gaits patterns as some of them highlighted below.

The most prevalent disorders are Parkinsonism and sensory ataxia. The first one is a well-known neurodegenerative disease with resting tremor and rigidity manifestation as the main conditions. People suffering from Parkinson's disease have a reduced stance and swing phase time compared to a control group. They also present gait abnormalities such as slow walking and a reduced stride length with increased variability of the stride. Moreover, patients can suffer from a short and temporary inability to move their feet forward that often leads to a fall. This event is commonly called freezing of gait.

The sensory ataxia is a condition that impairs muscle movement coordination as people suffering from it are unable to locate the different parts of their body with respect to each other and the ground. They will exhibit hard foot strike on each step and staggering gait pattern.

Only to mention, other neurological conditions such as stroke, traumatic brain injury, Alzheimer's disease, multiple sclerosis,... lead to gait abnormalities and falls [4].

Chapter 3

State of the art of assisting technologies to prevent falls and CMG

Gait analysis algorithms are used to detect and study neurological diseases dysfunctions in a patient. They provide digital gait characteristics that can play a crucial role in planning interventions, physical or pharmaceutical. To perform that, non-wearable or wearable sensors can be used in devices.

Wearable technologies have gained interest for monitoring gaits during daily activities at home and in the community like the G-WALK from BTS Bioengineering [12] or the MoveMonitor from McRoberts [13] that allow clinicians to follow their patient activities like their postural balance deficits. For the data assessment of wearable devices, magnetic, inertial measurement, and force sensors can be used [4].

Therefore, in this chapter, the state of the art of balancing assistance devices to prevent falls is covered. Then, a description of the Control Moment Gyro technology is given before its state of art.

3.1 Walking assistance devices

While there is a fullness of devices to monitor and detect when someone falls, to actively prevent it is more challenging, and such technologies are more scars. Indeed, many bulky and expensive rehab assisting devices like Lokomat, a lower limb exoskeleton on a treadmill, is used for gait training on patients how had a stroke.

It is only in recent years that a craze for lightweight and easier exoskeleton to assist walking balance for patients that lost their walking ability due to a condition, stroke, trauma,...

From such devices, the exoskeleton ReWalk depicted in Fig.3.3 can be mentioned, a wearable device that powers the hip and knees. It is the first FDA-approved device of the kind for personal and rehabilitation use that can be fully customized. It mimics the natural gait of the legs by transferring the weight from limb to limb that initial the steps [5].

Figure 3.1: ReWalk exoskeleton [5]

Similarly, Ekso Bionics commercialises the Ekso NR [6], a lower limb exoskeleton, that also has motors at the hip and knees joints to initiate and assist the patient's steps.

Depending on the condition state of the patient in rehab, those technologies can be used with crushes.

A more evolved device comes from Cyberdyne with HAL-5 that not only assists but also increases the physical functions of the wearer. To achieve that, it uses electromyography techniques such as electrodes placed on the skin to measure the muscle's electrical activities that are treated as a torque command for the exoskeleton. The signal can be either used for the suit to be synced with the desired movements voluntarily commanded or to realise human-like movements.

Less bulky and invasive, Honda has developed the walking assist, a device that is worn on the hip and actuates only the legs as depicted in Fig.3.2. With an angle sensor, the motors are activated to improve the symmetry of timing during the swing phases and to increase the step stride.

Figure 3.2: The Honda walking assist device [14].

While the latter were active exoskeleton, there exists passive devices such as the Kickstart walk assist system that is spring-loaded. The advantage of such a passive technology is primarily the weight and cost reduction but also in this case, how easier it is to operate [15].

Figure 3.3: Kickstart walk assist system, image taken from [15].

Lastly, a device of interest for this master thesis and developed at the University of Delft that takes the form of a backpack using Control Moment Gyro (CMG) to assist balance during quiet stance or walking. The technology is developed under the leadership of Prof. Vallery [2]. It has the particularity that, unlike the aforementioned devices, no sensors or actuators need to be attached to the lower limb or the hips. All the torque generation happens in the backpack which is less invasive and more comfortable if it was to be worn outside daily to assist elders in their common tasks.

3.2 Control Moment Gyro technology

A CMG is a simple mechanism that consists of a high-speed spinning wheel maintained by one or more actuated gimbals. By changing the angular position of the plane in which the wheel is spinning, a gyroscopic torque is generated. Compared to the reaction wheel technology that accelerates and decelerates to induce a torque, the power efficiency is better. Indeed, rotating a gimbal requires less power than continuously change the speed of the wheel.

3.2.1 Principal behind the CMG

Newton's second law states that to change the velocity of an object, a force needs to be exerted on it toward the change.

If a rotating wheel is taken, at time t_0, a point of the wheel has a velocity vector $\vec{v}_{t0}$ in a specific direction. Now, if the wheel was tilted by a certain angle, the same point would see its velocity vector $\vec{v}_{t1}$ change of direction as illustrated in Fig.3.4.

Following Newton's second law, a change in velocity implies a force $\vec{F}_{t1}$ coming from an actuator tilting the wheel. If now the event is observed from the top view of the CMG as illustrated in Fig.3.5, the opposite point to the one that was just

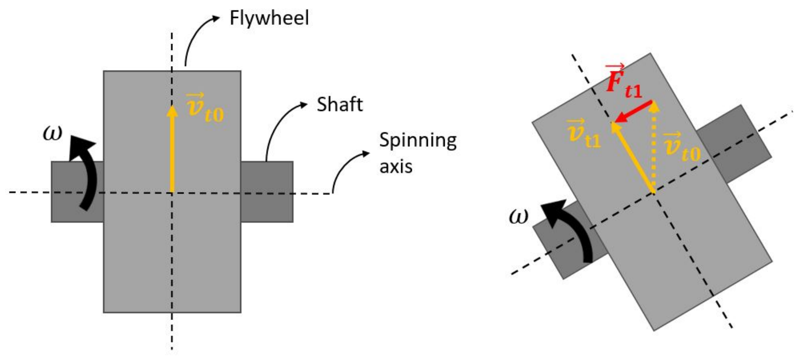

Figure 3.4: Scheme of the front plane of a flywheel and its shaft rotating with an angular speed ω to illustrate what happens when the wheel is tilted. In Yellow are the speed vectors at time t_0 and t_1 and in red the force vector.

observed designated by a prime ' is also under the same perturbation. But with its velocity vector $\vec{v'}_{t1}$ in the opposite direction, the force $\vec{F'}_{t1}$ is also. One can see that their sum is null but torque is generated in between.

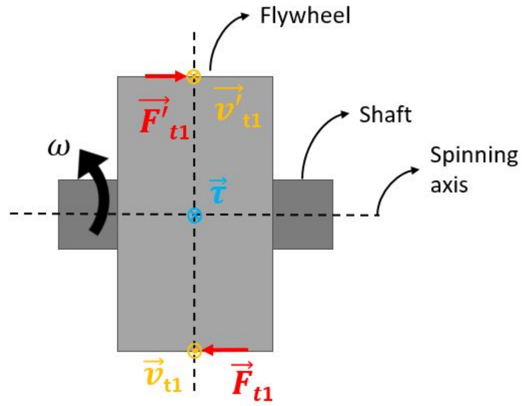

Figure 3.5: Scheme of the top plane of a flywheel and its shaft rotating with an angular speed ω to illustrate what happens when the wheel is tilted. In Yellow are the speed vectors at time t_1, in red the force vectors and in blue the torque.

By action-reaction, the opposite forces are applied from the wheel on the gimbal, the torque generated by the CMG τ_{CMG} is the opposite to the one depicted τ.

Therefore, for a wheel rotating about an axis x and mounted on a single gimbal with its degree of freedom along the axis y, the torque generated when the latter rotates is along the axis z. This orthogonal frame xyz is fixed to the gimbal, therefore the axis on which the torque is generated follows the gimbal rotation.

3.2.2 Control Moment Gyro state of the art

CMGs are a technology that is usually used for attitude control of spacecraft such as in the ISS but also on satellites for target tracking on the ground. This technology suits very well the space applications as it requires a little power to maintain the wheel speed and to tilt it.

CMG for space application can be bought directly from Airbus that offers their last generation CMG being compact, cost-effective, and performances with two more orders of magnitude than conventional CMG [16].

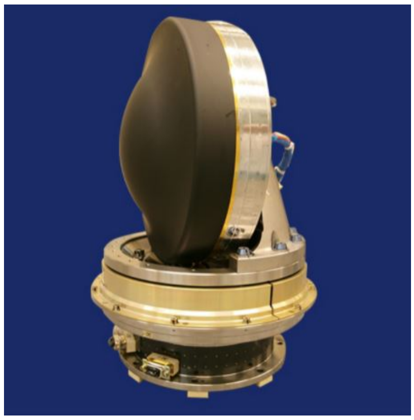

Figure 3.6: CMG from Airbus [16]

Then, CMGs became a solution to control the roll of a boat at sea [17]. The system will continuously measure the tilt of the boat and by actuating the gimbal, a counter torque is produced and the roll is drastically reduced. The product can operate in boats from 5 Tons and 7 meters up to a boat of 100 Tons and 26 meters.

Figure 3.7: CMG in boat roll control application [17]

More recently, a collaboration between NASA and Cornell University designed a rover using only a single CMG to move around [**rover**].

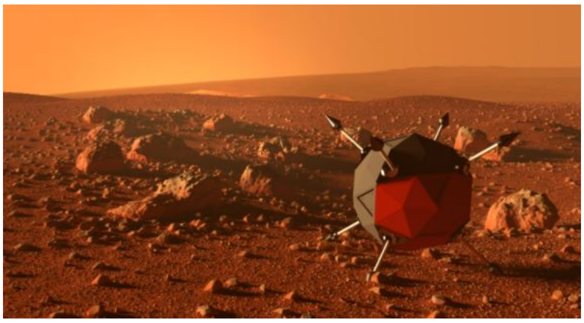

Figure 3.8: Rover designed to move around with a single CMG [18].

The device developed by the team of Prof. Vallery [2] aims at assisting the balancing of elders that are subject to conditions impairing their walking ability. Their goal is to design a backpack as depicted in Fig.3.9 that will use a set of CMG to control the generate torque and reorient someone falling.

Figure 3.9: Backpack like design of the assistance device developed by the team of Prof. Vallery [2].

Compared to the others technologies presented in the first section, the latter is less invasive as it does not require the wearer to place sensors on its different limbs nor to put an exoskeleton on. Also, most of them require the presence of a skilled operator due to the complexity of the suits while for the backpack, once designed and its safety assessed, it can be worn casually without the need of a third party.

The fact that all of what is needed to reorient someone can be gathered in a backpack that can be put on and off easily and characterized by a high power efficiency makes it promising.

Therefore, to assess the capacity of this technology numerically, the dynamical equations describing the system need to be derived before simulations can be run.

Chapter 4

Derivation of the dynamic equations for the inverted pendulum and CMG

While modeling bipedal walking is a challenge using gait analysis techniques because of the number of degrees of liberty in the lower limb, a body can be represented as a simple inverted pendulum tracking the center of mass. It is a sufficiently representative model of the stabilization of the pelvis during walking to study incipient falls. Indeed, with the pivot of the latter just below the bust when standing, the walk balancing as depicted in Fig.2.2 can be monitored and seen as oscillations of the pendulum [7].

As illustrated in Fig.4.1, the pendulum is composed of a ball joint, a mass-less beam and at its tip a ball corresponding to the body's position of center of mass (CoM) and of mass m.

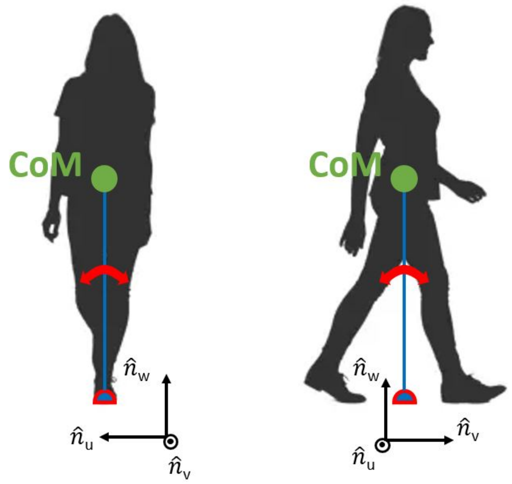

Figure 4.1: Use of an inverted pendulum as a simplified model of a body where the tip of the rod would correspond to the center of mass with a mass m. It can swings along with the $\hat{n}_u$ and $\hat{n}_v$ axis thanks to a ball joint. [Adapted from [19]]

Nevertheless, the torque produced by the CMG along a controlled orientation can easily be decomposed into two orthogonal components. If the oscillation can be controlled in one vertical plane, it can be done in any other vertical plane. Therefore, the pendulum can be reduced to one degree of freedom with a hinge joint instead of a ball joint to study the oscillations in the frontal plane for example. With this simplification, only one CMG is needed to generate the required torque for the inverted pendulum to remain in the defined equilibrium position.

This section aims to derive the necessary dynamical equations that will be used later in the control diagram of the system. First, the dynamic equation of an inverted pendulum is derived. Then the expression of the torque produced by the CMG is obtained through the Euler's equation of rotational motion and linked to the first equation.

4.1 Inverted pendulum dynamic equation

The equation characterizing the dynamics of an inverted pendulum is a well-known expression. Indeed, it has many applications in the engineering field as, among others, a model to simplify a more complex system like in the case of this master thesis. The following equation relates to the inverted pendulum dynamic and can be obtained in different ways.

$$ml^2\ddot{\phi} - mgl\sin(\phi) = \tau_{inv\_pend} - f_\phi\dot{\phi} \tag{4.1}$$

The equation is composed of the inertial term, ml^2, a viscous/ damping term, f_ϕ, the gravitational term, mgl, and an external torque, τ_{inv_pend}.

The different parameters characterizing the dynamics of the pendulum are: the length l in meter from the joint to the center of mass of mass m in kg. The torque τ_{inv_pend} in Nm produced by the CMG along the axis $\hat{n}_v$. The viscous damping coefficient f_ϕ is expressed in $Nm\cdot s/rad$ and refers to the damping naturally present in human physiology. This parameter induced by muscles and other visco-elastic tissue reduces oscillations. It also decreases the angular position of the pendulum exponentially with time [20] which can be demonstrated by solving the homogeneous part of the differential equation 4.1. The form of the latter solution is:

$$\phi_{(t)} = A\,e^{x_1 t} + B\,e^{x_2 t} \qquad \text{with} \quad x_{1,2} = \frac{-f_\phi \pm \sqrt{f_\phi^2 + 4gm^2l^3}}{2ml^2}$$

Where $x_{1,2}$ are the roots of the characteristic polynomial and with the initial condition of $\phi = 0$ at $t = 0$, the constant A and B are equals. Thus, the solution can be simplified as:

$$\phi_{(t)} = C\, e^{\frac{-f_\phi t}{2ml^2}} \cos\omega_0 t \qquad\qquad \text{with} \quad \omega_0 = \frac{\sqrt{f_\phi^2 + 4gm^2l^3}}{2ml^2}$$

4.2 Derivation of the equations characterizing the dynamics of Control Moment Gyro

The external torque τ_{inv_pend} defined in Eq.4.1 corresponds to the component of the torque generated by the CMG τ_{CMG} along the $\hat{n}_v$ axis. The latter torque is the coupling variable between the pendulum and CMG dynamics.

Whenever a rigid body is rotating, Euler's equation of rotational motion can be used. The latter links all the torques τ applied on the body with the rate of change of angular momentum $\dot{H}$.

$$\dot{H} = \tau \tag{4.2}$$

To study the dynamic of the assisting device, a CMG is mounted on the inverted pendulum defined above as depicted in Fig.4.2. From it, several parameters are defined.

The different frames defined to solve the problem are:

- N the reference frame fixed on the ground $\{\hat{n}_u, \hat{n}_v, \hat{n}_w\}$
- B the pendulum reference frame $\{\hat{b}_u, \hat{b}_v, \hat{b}_w\}$
- G the gimbal reference frame $\{\hat{g}_s, \hat{g}_t, \hat{g}_g\}$
- W the wheel reference frame $\{\hat{w}_s, \hat{w}_t, \hat{w}_g\}$

The different variables defined to solve the problem are:

- ϕ, $\dot{\phi}$ the tilt angle and the angular velocity of the inverted pendulum respectively w.r.t the reference frame N
- γ, $\dot{\gamma}$ the tilt angle and the angular velocity of the gimbal respectively w.r.t the reference frame B
- Ω the angular velocity of the wheel w.r.t the reference frame G
- m the body mass
- l the distance from the hinge to the center of mass

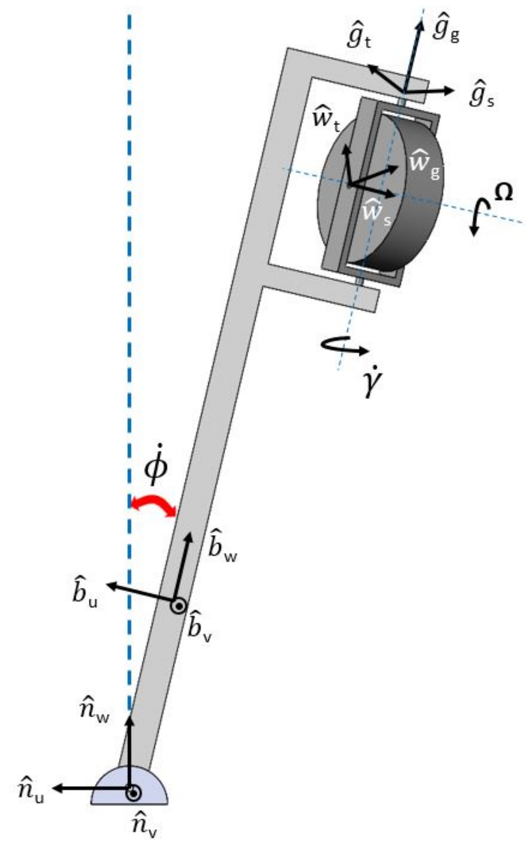

Figure 4.2: Lookalike illustration of what is to be prototyped, an inverted pendulum mounted with a CMG and its degrees of freedom. In this illustration, the different reference frames and variables (state or parametric) are represented.

Single gimbal control moment gyro have only two degrees of freedom that are the wheel and the gimbal free to rotate. Because it was decided that the flywheel rotates at constant angular velocity, Ω is a parametric variable. The state variables are thus the tilt angle and the angular velocity of the pendulum and gimbal.

The development to obtain the dynamic equations of the assisting device is strongly inspired by the work of J. Junkins and H. Schaub in their book [21]. If one wishes to read the complete adapted development, the demonstration is in the Appendix Section 11.1.

To solve Eq.4.2, the first step is to derive the expression of the angular momentum of the system in frame B. Which is defined as the product between the inertia matrix and the angular velocity. Also, the parameter $\mathbf{H}$ can be decomposed in the sum of the gimbal and wheel angular momentum expressed in frame B.

$$\mathbf{H}_{CMG} = \mathbf{H}_G + \mathbf{H}_W \qquad\qquad \mathbf{H} = [I]\,\boldsymbol{\omega} \tag{4.3}$$

Once the expression of $\mathbf{H}_{CMG}$ is obtained, it can be derived to obtain the following equation:

$$\begin{aligned}\dot{\mathbf{H}}_{CMG} = \hat{\mathbf{g}}_{\mathbf{s}} &\left[(J_s - J_t + J_g)\,\dot{\gamma}\dot{\phi}\cos(\gamma) + J_s\ddot{\phi}\sin(\gamma)\right] \\ &+ \hat{\mathbf{g}}_{\mathbf{t}}\left[I_{W_s}\dot{\gamma}\Omega + (J_s - J_t - J_g)\,\dot{\gamma}\dot{\phi}\sin(\gamma) + J_t\ddot{\phi}\cos(\gamma)\right] \\ &+ \hat{\mathbf{g}}_{\mathbf{g}}\left[J_g\ddot{\gamma} + \dot{\phi}^2\sin(\gamma)\cos(\gamma)\,(J_t - J_s) - I_{W_s}\Omega\dot{\phi}\cos(\gamma)\right]\end{aligned} \tag{4.4}$$

Where J_s, J_t and J_g are the diagonal components of the inertial matrix of the CMG system, composed of the wheel and the gimbal; I_{W_s} is the inertial component of the flywheel along its axis of rotation.

Equation 4.4 can be simplified because the angular speed of the wheel Ω is several orders of magnitude higher than the angular speeds of the gimbal $\dot{\gamma}$ and pendulum $\dot{\phi}$. The equation above thus becomes:

$$\begin{aligned}\dot{\mathbf{H}}_{CMG} = \hat{\mathbf{g}}_{\mathbf{s}} &\left[(J_s - J_t + J_g)\,\dot{\gamma}\dot{\phi}\cos(\gamma) + J_s\ddot{\phi}\sin(\gamma)\right] \\ &+ \hat{\mathbf{g}}_{\mathbf{t}}\left[I_{W_s}\dot{\gamma}\Omega\right] \\ &+ \hat{\mathbf{g}}_{\mathbf{g}}\left[J_g\ddot{\gamma} - I_{W_s}\Omega\dot{\phi}\cos(\gamma)\right]\end{aligned} \tag{4.5}$$

The torque needed to actuate the gimbal corresponds to the component along the $\hat{\mathbf{g}}_{\mathbf{g}}$-axis of $\dot{\mathbf{H}}_{CMG}$ from Eq.4.5 and defined as τ_{GM}.

$$\tau_{GM} = J_g\ddot{\gamma} - I_{W_s}\Omega\dot{\phi}\cos(\gamma) \tag{4.6}$$

Finally, the component along the $\hat{\mathbf{g}}_{\mathbf{t}}$-axis of $\dot{\mathbf{H}}_{CMG}$ from Eq.4.5, the expression of the torque generated by the CMG, τ_{CMG}, is given.

$$\tau_{CMG} = I_{W_s}\dot{\gamma}\Omega \tag{4.7}$$

To couple the dynamic equations of the pendulum with the one of the CMG, the expression above must be transposed from frame G to frame B such that:

$$\begin{aligned}\tau_B &= \tau_{CMG}\sin(\gamma)\hat{\mathbf{b}}_{\mathbf{u}} + \tau_{CMG}\cos(\gamma)\hat{\mathbf{b}}_{\mathbf{v}} \\ &= \tau_{CMG}\sin(\gamma)\hat{\mathbf{b}}_{\mathbf{u}} + \tau_{inv\_pend}\,\hat{\mathbf{b}}_{\mathbf{v}}\end{aligned} \tag{4.8}$$

It is also interesting to note that the bigger the angle of the gimbal is, the higher the angular speed would have to be for generating a similar torque.

$$\dot{\gamma} = \frac{\tau_{inv\_pend}}{I_{W_s}\Omega\cos(\gamma)} \tag{4.9}$$

4.3 Summary

From this chapter, the equations characterizing the different systems were derived.

The first one, concerning the dynamics of the pendulum, was obtained from the Euler-Lagrange equation. The result reminded bellow takes into account an external torque, τ_{inv_pend}, which is applied by the CMG on the pendulum; and a viscous damping, f_ϕ, which accounts for the damping naturally present in the human physiology.

$$ml^2\ddot{\phi} - mgl\sin(\phi) = \tau_{inv\_pend} - f_\phi\dot{\phi}$$

The second system studied was the CMG. More complex, the equations characterizing the latter have been obtained from the rate of change of angular momentum $\dot{H}$ that is equal to a torque. By solving this relation in the appropriate frame, B, the expression of the torque generated by the CMG was obtained along each axis of the frame by the CMG is obtained.

The torque obtained along the $\hat{\mathbf{b}}_\mathbf{v}$-axis corresponds to the effective torque that the CMG will apply on the pendulum.

$$\tau_{inv\_pend} = I_{W_s}\dot{\gamma}\Omega\cos(\gamma)$$

The second torque expression of interest is along the $\hat{\mathbf{b}}_\mathbf{w}$-axis. Indeed, it corresponds to the amount of torque needed to make the gimbal rotates.

$$\tau_{GM} = J_g\ddot{\gamma} - I_{W_s}\Omega\dot{\phi}\cos(\gamma)$$

Those three equations put together characterize the dynamics of the pendulum mounted with a CMG. With those information, the behaviour of the system can be studied when it is subjected to perturbations. For this, a law allowing to control the dynamic model of the pendulum and CMG must be designed and implemented in Simulink.

Chapter 5

Control of the inverted pendulum

Now that the equations describing the dynamics of the inverted pendulum and CMG have been derived, the design of the control system can be made. The aim of this chapter is, first, to build the dynamics models of the systems and their controllers which are inspired by the diagram depicted in the article published by the team of Prof. Vallery [22].

Then, the unknown parameters will be estimated and an algorithm to keep the gimbal at the desired angle will be added to the control diagram.

Finally, the stability of the overall system will be studied through the poles and zeros of transfer functions of the linearized system.

5.1 Design of the systems to control and their controllers

In control theory, models and algorithms are developed to control dynamic systems so that they are driven to a desired state. There are two types of control design; open-loop control in which the controller does not consider the output of the system. This leads to errors between the expected and real controlled parameters. On the other hand, a closed-loop feedback control does consider the output generated by the system. If there is a difference between the expected and real controlled parameters, the controller is aware of it and a correction is made.

For the inverted pendulum control, the second type of design is preferred and a representation of the latter is depicted in Fig.5.1. The reference also called the setpoint is the desired state for the system to reach. The measured error is the difference between the setpoint and the measured output of the system, its state. The system input or command is the parameter that commands the modelled system to control.

The block *system* also called *plant* corresponds to the model of the system to control. In this master thesis, the system is the modelled dynamics of the inverted pendulum and CMG.

Then, the block *controller* is the algorithm that will generate the adequate command to drive the system to the desired state based on the error. The controller can include a Proportional, Integral, and/or Derivative controller and take the form of a P, PI, PID, or PD controller. The proportional term amplifies the error while the integral term integrates the error to cancel it and the derivative term damps the response.

Finally, the block *Sensor* is the measured parameter compared to the reference value. In this work, the sensor corresponds to an accelerometer measuring the tilt of the pendulum [23].

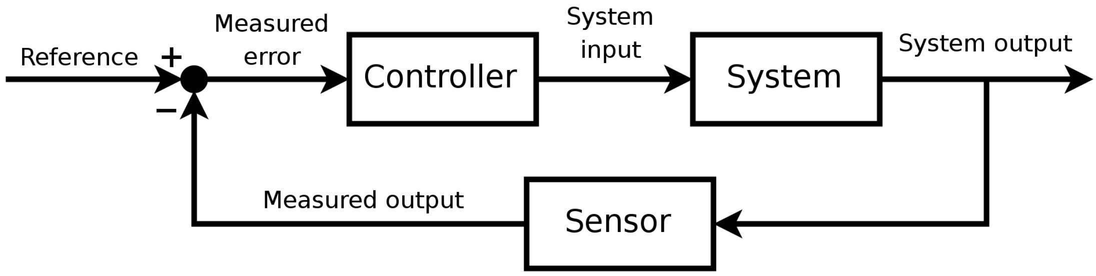

Figure 5.1: A generic representation of closed-loop feedback control including the system to control, a controller, and the feedback [23].

This general representation is used to design the closed-loop feedback control of the system. With the latter is composed of two sub-systems, the dynamics of the inverted pendulum and CMG, the diagram will be composed of a High-level feedback loop for the pendulum and a Low-level feedback loop for the CMG.

High-level feedback loop design

The high-level feedback loop depicted in Fig.5.2 has for plant the modelled dynamic of the inverted pendulum. This block is characterized by the equation derived in the previous chapter and reminded in the figure. The objective of the controller is to maintain the pendulum in a vertical position therefore the reference variable is the angular position of the pendulum ϕ. The command is naturally the external torque τ_{inv_pend} that will be generated by the CMG. Therefore, the angular acceleration of the pendulum $\ddot{\phi}$ is first obtained, and then by integration, $\dot{\phi}$ and ϕ are found.

For the control law, a proportional controller is chosen. With the dynamics of the pendulum characterized by a damping term, adding a derivative term is not relevant. No integral action is implemented either as it is in the lower level feedback control that the error will be corrected. The controller takes the form of a virtual spring as described in Eq.5.1 with the proportional coefficient $k_v s$. Whenever the pendulum moves away from the desired position, a torque in the opposite direction is requested as a spring pulling back a mass moving off.

$$\tau_{inv\_pend} = k_{vs} \varepsilon_\phi \tag{5.1}$$

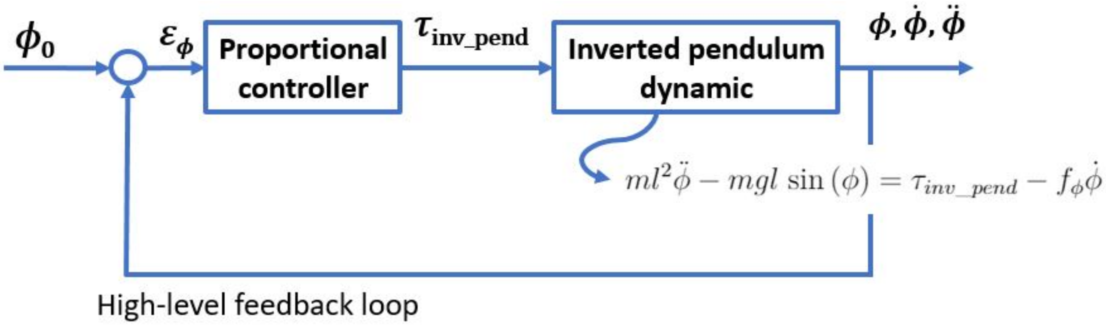

Figure 5.2: High-level feedback loop with the inverted pendulum dynamic to control with a proportional controller. The reference parameter is the angular position of the pendulum and the command is the external torque applied on the latter.

Low-level feedback loop design

Similarly, the low-level feedback loop depicted in Fig.5.3 has for plant the modelled dynamic of the CMG. This block is characterized by the equation derived in the previous chapter and reminded in the figure. This equation is the expression of the torque along with the axis $\hat{\mathbf{b}}_\mathbf{w}$ corresponding to the torque needed to rotate the gimbal. Therefore, the command is the torque τ_{GM} and the variable controlled is the angular velocity of the gimbal $\dot{\gamma}$. Indeed, the latter is chosen instead of the angular position as the torque generated by the CMG, reminded in Eq.5.2, depends on $\dot{\gamma}$ and not γ.

$$\tau_{CMG} = I_{W_s}\dot{\gamma}\Omega \tag{5.2}$$

The latter being part of the derived dynamical equation, it is considered in the plant. The torque generated by the CMG and transmitted to the pendulum is the parameter of interest.

One can see that the system is not SISO but MIMO because of the dynamic of the two subsystems. Indeed, one can see that Eq.4.6 depends on the angular speed of the pendulum $\dot{\phi}$. With τ_{GM} and $\dot{\phi}$, the angular acceleration of the gimbal $\ddot{\gamma}$ is obtained, and by integration, $\dot{\gamma}$ and γ are found to compute the effective torque generated.

For the control law, a Proportional-Integral controller is chosen to make sure that the gimbal angular velocity required is correctly tracked as it is directly linked to the generated torque.

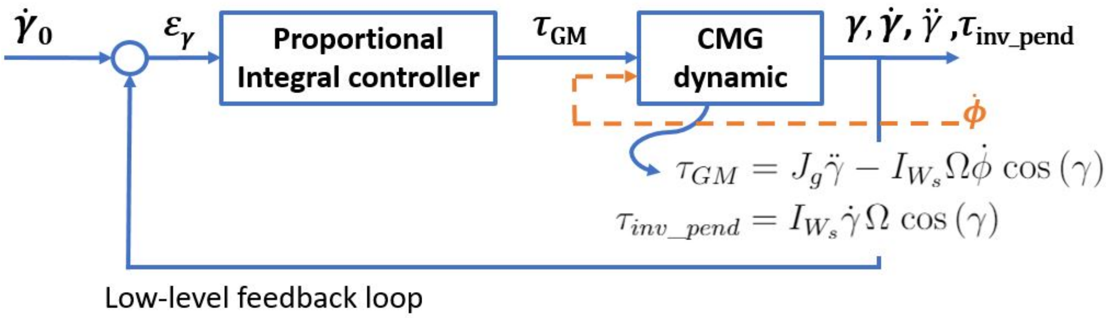

Figure 5.3: Low-level feedback loop with the CMG dynamic to control with a PI controller. The reference parameter is the angular velocity of the gimbal and the command is the torque applied on the gimbal to rotate it.

Incorporating the Low-level feedback control into the High-level feedback control

The integration of the Low-level feedback loop into the High-level feedback loop is done in between the controller and the plant of the latter. As the expression of the torque transmitted to the pendulum τ_{inv_pend} derived at the output of the low-level feedback loop system block can directly be linked to the input of the high-level feedback loop plant.

On the other hand, the input of the low-level feedback loop is the angular velocity of the gimbal. The transition between the required torque at the output of the Proportional controller and $\dot{\gamma}$ is possible with an allocation law as defined in the paper published by the team of Prof. Vallery [22]. This law is expressed in Eq.4.9 and reminder below.

$$\dot{\gamma} = \frac{\tau_{inv\_pend}}{I_{W_s}\Omega\cos(\gamma)}$$

The overall control diagram implemented in Simulink is depicted in Fig.5.4. One can see the high- and low-level feedback loop framed in the orange and green dashed lines respectively. The system blocks are the two on the far right, the CMG dynamic and pendulum dynamic blocks. While the other three blocks, the virtual spring, the allocation law, and the PI blocks, are the controllers to control the system.

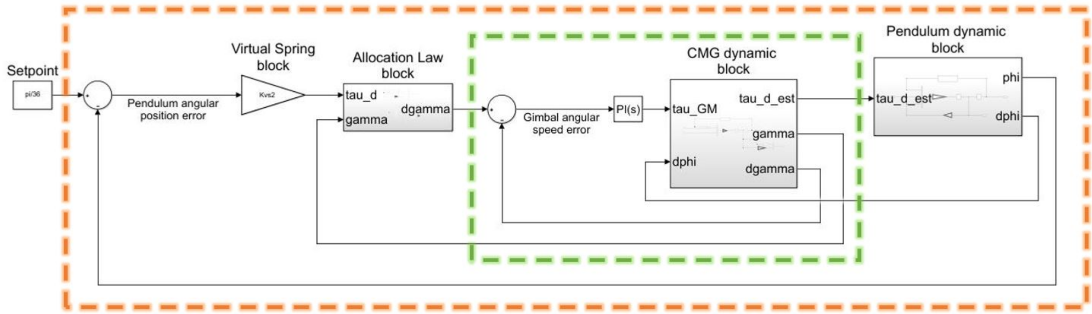

Figure 5.4: The overall diagram to control the inverted pendulum mounted with a CMG implemented in Simulink. The low-level controller is framed by green dashed lines while the high-level controller is framed by orange dashed lines.

Compared to the control diagram depicted in the article by the team of Prof. Vallery [22], one can see that the gimbal actuator unit block is missing. It corresponds to the physic of the motor used to actuate the gimbal. In this work, the actuators are assumed ideal explaining the missing block in the diagram.

5.2 Simulation of the dynamic system

5.2.1 Parameters definition

To run the simulation, the different parameters characterizing the dynamic models and controllers have to be estimated. To get an idea of some values orders of magnitude, the paper published by the team of Prof. Vallery reported some of their data [22]. In Tab.5.1, the parametric variables are listed with their values if given in the article.

In the paper, with the objectives to make the wearable device as thin and light as possible, they have made the design decision that the device will be equipped with three CMG. Each one should generate an effective torque of $90\,Nm$ during $0.1\,s$ to reorient a human at a 10 degree angle of $1.7\,m$ tall and weighing $70\,kg$.

For this model, the same design choice is made to keep the parameters order. Therefore, to take into account the three identical CMG in the control of the system, the torque required after the virtual spring block is divided by three while the output torque of the CMG dynamic block is multiplied by three.

Table 5.1: The parameters characterizing the models of dynamic systems and controllers.

Parametric variables	Symbols	Values	Units
Mass	m	70	kg
Elder height	h	1.7	m
Height of the CoM	l		m
Viscous damping	f_ϕ		$Nm\,s/rad$
Inertia of the flywheel along the s-axis	I_{W_s}	0.02	$kg\,m^2$
Inertia of the CMG along the g-axis	J_g		$kg\,m^2$
Angular speed of the flywheel	Ω	5400	rpm
Virtual spring constant	k_{vs}	600 to 1200	Nm/rad
Proportional constant of the PI controller	k_P		$Nm\,s/rad$
Integral constant of the PI controller	k_I		Nm/rad

Parametrization of the weight and height of the pendulum

The average weight and height of elders are data found in anthropometry papers that measure human body proportions. From articles based on healthy aged populations from Taiwan [24], Australia [25], United States [26], and Belgium [27], the average stature and weight of males and females of the latter populations are gathered in Tab.5.2.

For the design of the wearable device, the parameters must be selected so that most of the targeted population can benefit from the technology. When looking at data from different regions of the world, one can see that males are taller and heavier than females such that their average height is $168\,cm$ and weight is $74\,kg$. The values selected in the paper by the team of Prof. Vallery are therefore relevant as it is lighter but taller.

As explained in Chapter 4, for the design of the pendulum modeling the human body, its mass is located at its tip representing the center of mass. The latter is said to be located at 57% of a male height so for someone $1.7\,m$ tall, its center of mass is at $0.97\,m$ [28].

Table 5.2: Average anthropometry of elderly males and females from different countries.

Country	Age	Stature $[m]$	Weight $[kg]$	Year of measures
Male				
Taiwan [24]	71	1.64	63	1989-1991
Australia [25]	76	1.66	72	2001
United state [26]	Over 60	1.74	85	2003-2006
Belgium [27]	65-80	1.67	75.8	2005
Average	\	1.68	74	\
Female				
Taiwan [24]	71	1.51	56	1989-1991
Australia [25]	77	1.51	61	2001
United state [26]	Over 60	1.6	72	2003-2006
Belgium [27]	65-80	1.57	68.4	2005
Average	\	1.55	64.4	\

Parametrization of the viscous damping of the pendulum

For the viscous damping, a paper on the stiffness and damping in postural control reported measurements of the latter on seven adults aged 68 to 81 years and ten younger ones aged 21 to 30 years. For the damping, they distinguished the active damping neurally mediated implying a delay from the passive damping that does not. The latter comes from the intrinsic visco-elasticity of muscles and stiffness of tendons producing a gravity counter-force. The result of the experiment showed that older adults are stiffer with normalized active and passive damping of $4.9\,s^{-1}$ and $0.6\,s^{-1}$ respectively [29]. In the case of this work, it is assumed that there is no delay so that the viscous damping f_ϕ is equal to $5.5\,s^{-1}$.

Therefore, one could wonder how much damped the model of the pendulum dynamical system is. In system theory, a transfer function of order two and higher is characterized by a damping ratio ζ, a natural frequency ω_n, and a gain K. The canonical form of such a second order function is given in Eq.5.3.

$$Tr_{(s)} = K\frac{\omega_n^2}{s^2 + 2\zeta\omega_n s + \omega_n^2} \tag{5.3}$$

The damping ratio characterizes the frequency response of the system as the damping reduces or prevents oscillations. The energy stored in the latter is dissipated through processes that produce the damping [30]. According to the value of ζ, the system is said:

- Undamped for $\zeta = 0$
- Underdamped for $0 < \zeta < 1$
- Overdamped for $\zeta > 1$
- Critically damped for $\zeta = 1$

A critically damped system has for main properties that it has no overshoot and the fastest response time which is often looked for in a mechanical design.

To evaluate the damping ratio of the pendulum, its dynamical equation reminded below is linearized while considering there are no external forces applied to the system.

$$ml^2\ddot{\phi} + f_\phi\dot{\phi} - mgl\,\sin(\phi) = 0$$

The linearization of the equation is done using the Taylor approximation on the states variables, ϕ and $\dot{\phi}$, around a fixed point $\overline{x} = [\pi; 0]$, the pendulum downward. From the approximations, the matrices of the state-space representation for each block are obtained and so their transfer function.

State-space representation:

$$\begin{cases} \dot{x} &= A\,x + B\,u \\ y &= C\,x \end{cases} \qquad \Rightarrow \text{Transfer function:} \quad Tr = C\,(s\,I - A)^{-1}\,B$$

With u the command vector, y the output vector, I the identity matrix, and s the Laplace transform variable.

The transfer function obtained, Eq.5.4, is compared to Eq.5.3 to find the damping ratio ζ for $f_\phi = 5.5 \cdot I_{pend}$. The inertia of a pendulum is equal to ml^2 for which the values obtained above are used. The viscous damping f_ϕ is thus equal to $362.25\, Nm\, s/rad$.

$$Tr_{pend(s)} = \frac{\frac{1}{ml^2}}{s^2 + \frac{f_\phi}{ml^2}s + \frac{g}{l}} \tag{5.4}$$

The damping ratio found is equal to 0.864 which means that the system is underdamped. To be critically damped, $\zeta = 1$, the viscous damping must be equal to 418.83 $Nm\, s/rad$.

A comparison of the pendulum dynamic system with both values of f_ϕ is depicted in Fig.5.5. For this simulation, the control was removed to let the pendulum fall freely from 170 to 180 degrees, a stable position.

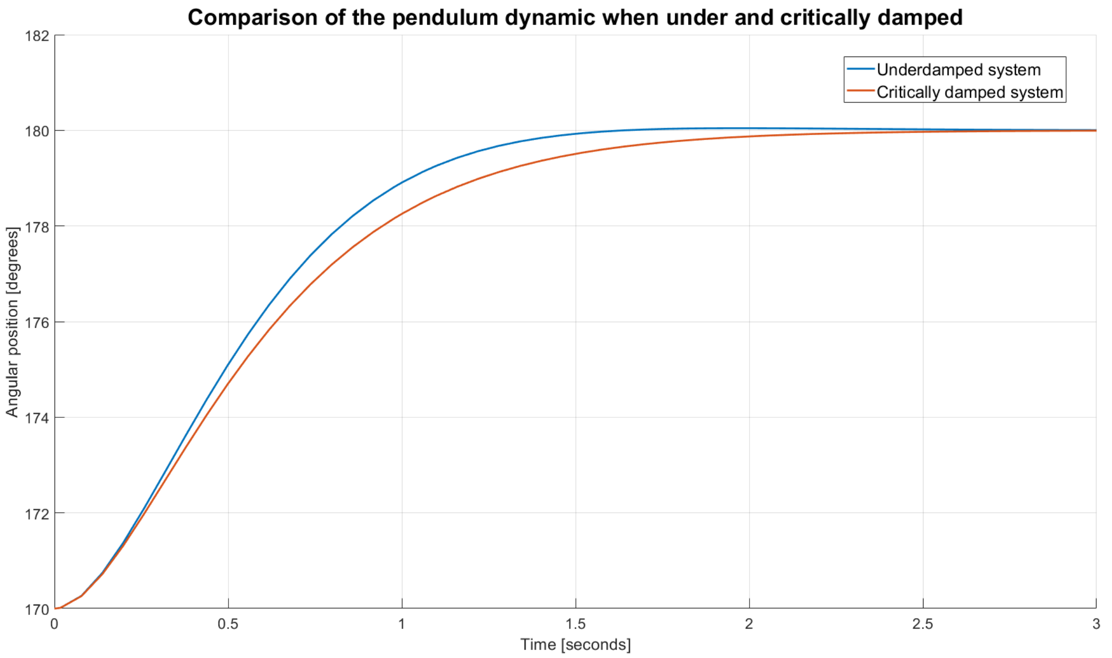

Figure 5.5: A comparison of the system behaviour when it is underdamped, $f_\phi = 362.24\, Nm\, s/rad$, and critically damped, $f_\phi = 418.83\, Nm\, s/rad$.
The pendulum is under no control and let free to fall from 170 to 180 degrees.

One can see that the underdamped system only has a tiny overshoot compared to the critically damped one. To respect the model of the human body represented by the pendulum, the first value obtained for the viscous damping is kept.

Parametrization of the inertia of the CMG

While the inertia of the flywheel along its spinning axis was given in the paper, the inertia of the CMG along the actuated axis of the gimbal was not. This parameter being proper to the design, it was impossible to estimate it directly. Nevertheless, in articles giving both inertia magnitude [31, 32], it was observed that J_g was usually the half of I_{W_s}. Therefore, the missing inertia can be estimated at $0.01\,kg\,m^2$.

5.2.2 Simulation of the inverted pendulum controller

To run the simulation, the three coefficients of the feedback controllers, k_{vs}, k_P, and k_I, need to be tuned. For the virtual spring constant, several values were given in the paper by the team of Prof. Vallery [22]. The higher the parameter amplitude, the stronger the answer to a perturbation is. Therefore, after several tests on a model without the low-level feedback loop implemented, the value for k_{vs} is set to $1200\,Nm/rad$. This amplitude leads to a fast system response without requiring too much torque, equivalently, the controller will ask the system to generate $21\,Nm/degrees$.

The PI parameters have also been determined through trail and error on the complete system that led to a k_P of 40 and a k_I of 20.

To perform those parameters tuning, the initial condition on the angular position ϕ of the pendulum is set to 3 degrees. This small perturbation is sufficient to validate the controllers and dynamic models implemented.

Then, with the parameters settled, the perturbation is increased to 10 degrees which represents a bigger challenge and is closer to what the designed device should correct. Nevertheless, the parameters selected are not high enough for the controllers to bring the pendulum back to its vertical position. To validate this milestone, the angular velocity of the wheel Ω and both inertia I_{W_s} and J_g are increased for the three CMG to generate greater torque. The value of the parameters used to successfully control the angular position of the pendulum are gathered in Tab.5.3.

This experiment is also the one described in the article by the team of Prof. Vallery [22], the pendulum initially tilted by 10 degrees.

Table 5.3: The new parameters characterizing the models of dynamic systems and controllers to successfully bring back the pendulum.

Parametric variables	Symbols	Values	Units
Mass	m	70	kg
Elder height	h	1.7	m
Height of the CoM	l	0.97	m
Viscous damping	f_ϕ	362.25	$Nm\,s/rad$
Inertia of the flywheel along the s-axis	I_{W_s}	0.02 $\rightarrow$ 0.06	$kg\,m^2$
Inertia of the CMG along the g-axis	J_g	0.01 $\rightarrow$ 0.03	$kg\,m^2$
Angular speed of the flywheel	Ω	5400 $\rightarrow$ 8000	rpm
Virtual spring constant	k_{vs}	1200	Nm/rad
Proportional constant of the PI controller	k_P	40	$Nm\,s/rad$
Integral constant of the PI controller	k_I	20	Nm/rad

In Fig.5.6 are depicted the angular positions of the pendulum and gimbal with the effective torque generated by one CMG. One can see that the control model succeeded in pulling back the inverted pendulum to the desired position. The behaviour of the controller involves no overshoot, and a rapid settling time.

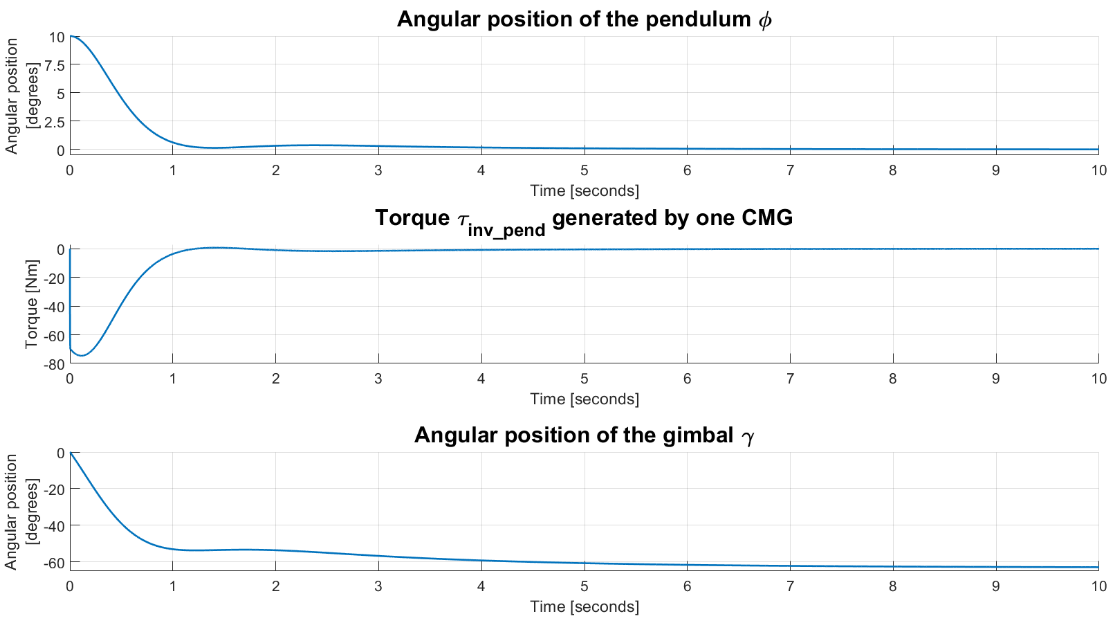

Figure 5.6: Control of the inverted pendulum tilted by 10 degrees with the corrected values of the parameters.

On the second plot, the torque generated by a single CMG reaches $75\,Nm$ at its peak; it is smaller but close to the magnitude of the torque required in the article from the team of Prof. Vallery [22].

Finally, the angular position of the gimbal is displayed. One can see that the gimbal has stopped past 60 degrees which is close to the singularity. Indeed, the torque transmitted to the pendulum is the cosine of the one generated by the CMG and in this configuration, only half of it is effectively transmitted. Thus, the more the gimbal rotates, the smaller the effective torque is applied on the system. Moreover, the sign of the torque depends on the one of the angular velocity of the gimbal. Therefore, if the stabilized pendulum was subjected to a second perturbation in the same direction, $\dot{\gamma}$ would have to be negative again, and γ get closer to the singularity.

$$\tau_{inv_pend} = \tau_{CMG} \cos\gamma \qquad\qquad \tau_{CMG} = I_{W_s}\dot{\gamma}\Omega$$

5.2.3 Attractive potential field

A contribution of this Master thesis has been to augment the gimbal controller with a mechanism forcing it to move back to its initial angular position. With the effective torque being the cosine of the one generated by the CMG, leaving the gimbal in an angular position other than 0 degree to counter a perturbation is not efficient and can lead the gimbal to the singularity.

It exists an algorithm in robotics called "*Potential Field path planning*" used for navigation that creates attractive and repulsive gradients, $\nabla U_{att}(q)$ between the desired position and the robot, and $\nabla U_{rep}(q)$ between an obstacle and the robot [33, 34]. The concept is defined in Eq.5.5 with $F(q)$ the resulting force applied on the system, $U(q)$ the resulting potential field, and q the states variables that in our case corresponds to γ. Variations of this algorithm have already been used with CMG to avoid singularities with super-quadratic iso-potential contours function of the gimbal angle [35]; by considering singularities as obstacles [36]; or to prevent the saturation of the momentum in the attitude controller and to steer gimbal [37].

$$F(q) = -\nabla U(q) \qquad \text{with} \quad U(q) = U_{att}(q) + U_{rep}(q) \tag{5.5}$$

Because the device will work in a defined environment and the objective is for the gimbal to come back to its initial position, only the attractive field is relevant. Nevertheless, if the gimbal was to get too close to the singularity because of a too important perturbation, the controller should be stopped.

The attractive potential is defined in Eq.5.6 as a parabolic function with a positive scaling factor k_{att}.

$$U_{att}(q) = \frac{1}{2} k_{att} \rho^2_{goal}(q) \qquad \text{with} \quad \rho_{goal}(q) = \parallel q - q_{goal} \parallel \tag{5.6}$$

By solving Eq.5.5 using Eq.5.6, the expression of the attractive force is derived. The desired angle is represented by γ_{goal} and the actual angle by γ.

$$F_{att}(\gamma) = -k_{att} (\gamma - \gamma_{goal}) \tag{5.7}$$

In Fig.5.7, one can see a top view representation of the CMG rotated from γ with respect to frame B. In this configuration, the attractive gradient should pull frame G toward frame B, thus the $\hat{b}_u$ component of F_{att} should be positive.

To respect the sign of F_{att} and its parameters definition, the negative sign in the expression of Eq.5.7 is removed. Leaving it makes the gimbal rotates more and thus add perturbation to the system.

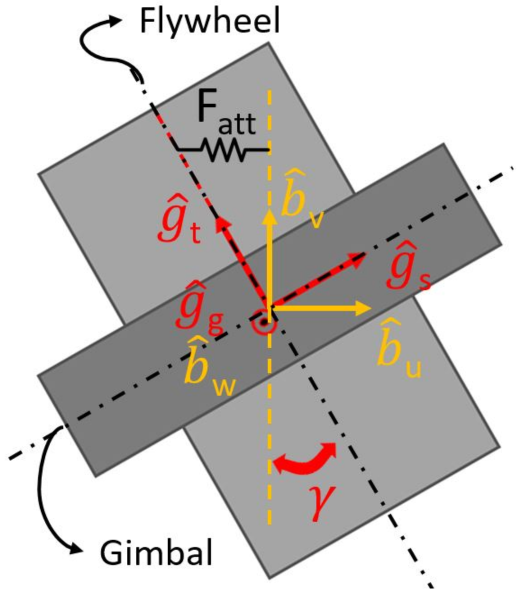

Figure 5.7: Top view of a CMG scheme with the attractive gradient F_{att} and the references frames of the gimbal G in red and pendulum B in yellow.

To test this algorithm, the attractive gradient is added to the reference angular velocity $\dot{\gamma}_0$ in the allocation law block as depicted in Fig.5.8. The scaling factor is set to 0.4 such that it does not interfere with the control of the pendulum when it is subjected to a perturbation. This value was chosen by trial and error with the objective for the pendulum to be stable and for the gimbal to be back to its initial angular position in under 10 seconds.

The validation of this new control law is done in the same environment as for the first system, the angular position of the pendulum ϕ initially tilted by 10 degrees.

In Fig.5.9, one can observe the effect of the potential field algorithm integrated into the control diagram. One can see already that the attractive potential field succeeded in its task to bring the gimbal back under the 10 seconds. A greater constant k_{att} will reduce even more the time for the gimbal to reach its initial orientation but will generate a more important torque on its way back. Oscillations would then be observed.

One can see that the pendulum takes much longer to reach the desired upright position and now has an overshoot with the new steering law. When the gimbal rotates back to its initial configuration, a torque is generated justifying the longer response time. The gimbal is then in its optimal position to respond to the next perturbation. Also, no significant differences are observed regarding the torque generated by the CMG.

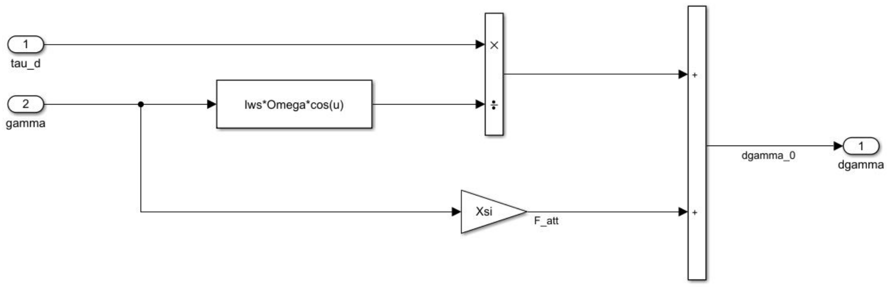

Figure 5.8: The implementation of the attractive potential field added into the allocation law block in simulink.

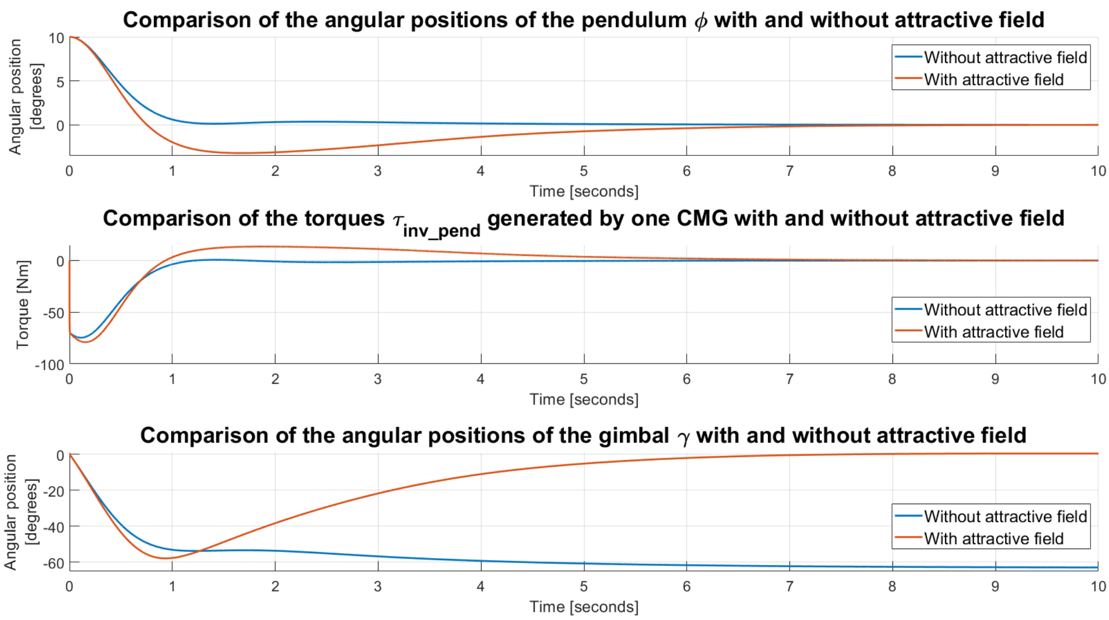

Figure 5.9: Comparison of the controller behaviour with and without the effect of the potential field algorithm. The same conditions were applied to the pendulum as in Fig.5.6.

5.3 Analysis of the control diagram stability

To study the stability of the controller, each of the blocks must be linearized using the Taylor approximation on the states variables around a fixed point $\overline{x}$ as explained earlier. The latter are for the pendulum ϕ and $\dot{\phi}$ with the fixed points at $[0;0]$, and for the gimbal γ and $\dot{\gamma}$ with the fixed points at $[0;0]$. From the approximations, the matrices of the state-space representation for each block are obtained and so their transfer function.
State-space representation:

$$\begin{cases} \dot{x} & = A\,x + B\,u + D\,v \\ y & = C\,x \end{cases} \qquad \Rightarrow \text{Transfer functions:} \quad Tr = C\,(s\,I - A)^{-1}\,B$$

$$Tv = C\,(s\,I - A)^{-1}\,D$$

With u the command vector, y the output vector, v the disturbance, I the identity matrix, and s the Laplace transform variable. The transfer function from the setpoint to the output is Tr while Tv is from the disturbance to the output.

Each block that has multiple inputs and/or multiple outputs (MIMO), has multiple transfer functions that relate the system outputs to its inputs. Therefore, the allocation law, the CMG dynamic, and the pendulum dynamic blocks have several transfer functions stored in matrices of size [*nbr_output* x *nbr_input*]. A MIMO system can thus be written as:

$$\begin{bmatrix} o_1 \\ o_2 \end{bmatrix} = \begin{bmatrix} Tr_{11} & Tr_{12} & Tr_{13} \\ Tr_{21} & Tr_{22} & Tr_{23} \end{bmatrix} \begin{bmatrix} i_1 \\ i_2 \\ i_3 \end{bmatrix}$$

In Fig.5.10, the linearized control diagram is depicted with each block transfer functions. The complete expression of those transfer functions as their state-space matrices are gathered in Appendix Section 11.2.

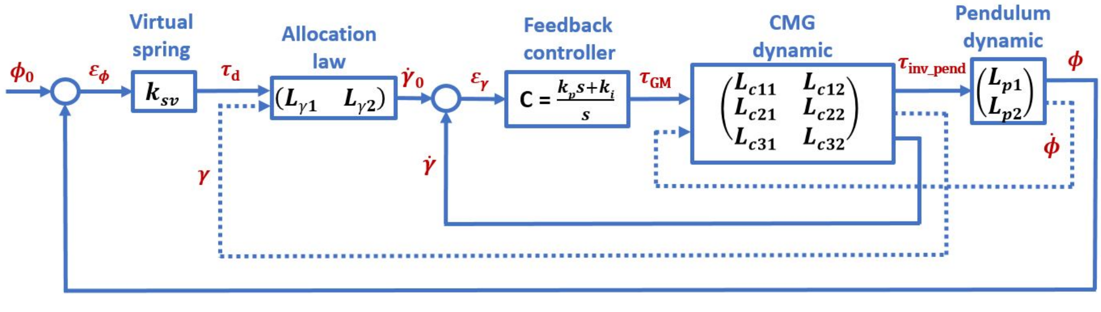

Figure 5.10: Representation of the linearized control diagram with their transfer functions in matrix form.

5.3.1 High-level controller stability - closed loop setpoint to output

With the obtained transfer functions, the one from ϕ_0 to ϕ is computed and displayed in Eq.5.8. The poles and zeros of this function have relevant information about the stability of the system's overall control.

Numerically, the equation is of order 8 and has 5 zeros where each of them have their real part negative attesting of the system's stability around $\phi = 0$ as one could have observed in the previous experiments. The poles-zeros map of the overall controller is depicted in Fig.5.11 with the poles and zeros.

$$Tr = \frac{\phi}{\phi_0} = \frac{\dfrac{\frac{CL_{p1}L_{c11}L_{\gamma 1}K}{1-C(L_{\gamma 2}L_{c21}-L_{c31})}}{1-L_{p2}\left(L_{c12}+\frac{CL_{c11}(L_{\gamma 2}L_{c22}-L_{c32})}{1-C(L_{\gamma 2}L_{c21}-L_{c31})}\right)}}{1+\dfrac{\frac{CL_{p1}L_{c11}L_{\gamma 1}K}{1-C(L_{\gamma 2}L_{c21}-L_{c31})}}{1-L_{p2}\left(L_{c12}+\frac{CL_{c11}(L_{\gamma 2}L_{c22}-L_{c32})}{1-C(L_{\gamma 2}L_{c21}-L_{c31})}\right)}} \tag{5.8}$$

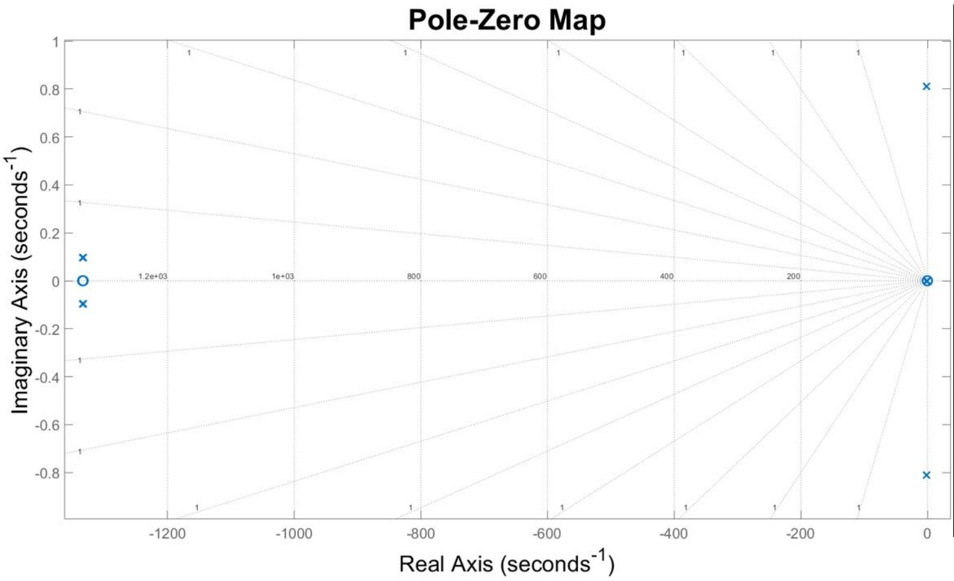

Poles
-1334.21 + 0.1i
-1334.21 - 0.1i
-1333.22 + 0.1i
-1333.22 - 0.1i
-1.26 + 0.81i
-1.26 - 0.81i
-1.51
-0.6
Zeros
0
-1333.23
-1333.23
-1334.2
-0.5

Figure 5.11: Poles and zeroes map of the high-level feedback loop from the setpoint ϕ_0 to the output ϕ attesting of the system's stability.

5.3.2 High-level controller stability - closed loop disturbance to output

In the same manner, the transfer function from the disturbance to the output ϕ is obtained and given below. The latter has its five poles with their real part negative, and one zero out of three has its real part positive. The response of the system controlled to an external perturbation is then stable. The poles-zeros map of the feedback loop is depicted in Fig.5.12.

$$Tv = \frac{\phi}{v} = \frac{L_{p1}\left(1 + \frac{L_{p2}\left(L_{c12}+\frac{CL_{c11}(L_{\gamma 2}L_{c22}-L_{c32})}{1-C(L_{\gamma 2}L_{c21}-L_{c31})}\right)}{1-L_{p2}\left(L_{c12}+\frac{CL_{c11}(L_{\gamma 2}L_{c22}-L_{c32})}{1-C(L_{\gamma 2}L_{c21}-L_{c31})}\right)}\right)}{1+\frac{\frac{CL_{p1}L_{c11}L_{\gamma 1}K}{1-C(L_{\gamma 2}L_{c21}-L_{c31})}}{1-L_{p2}\left(L_{c12}+\frac{CL_{c11}(L_{\gamma 2}L_{c22}-L_{c32})}{1-C(L_{\gamma 2}L_{c21}-L_{c31})}\right)}} \tag{5.9}$$

Because of the positive zero, the system is said to be at a non-minimum of phase and should show an inverse response at first. To observe that, a torque perturbation is added to τ_{inv_pend} between the two dynamic blocks which is similar to someone is giving a push to the physical pendulum. The amplitude of the external torque added is chosen such that the tilt induced by the latter reaches 10 degrees.

With the result depicted in Fig.5.13, one can see the inverse response in the gimbal angular position and generated torque.

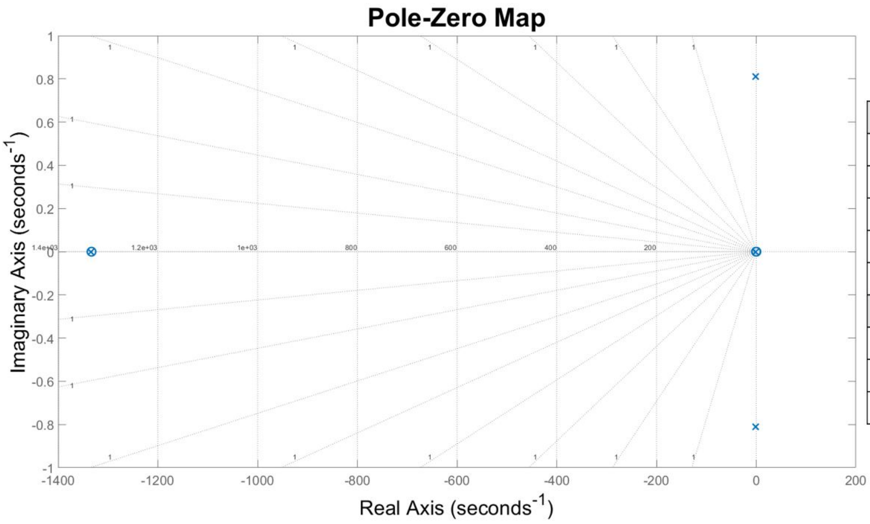

Poles
-1334.2
-1.26 + 0.81i
-1.26 - 0.81i
-1.51
-0.6
Zeros
-1333.23
-0.5
0.4

Figure 5.12: Poles and zeroes map of the high-level feedback loop from the disturbance v to the output ϕ attesting of the system's stability and its non-minimum phase characteristic.

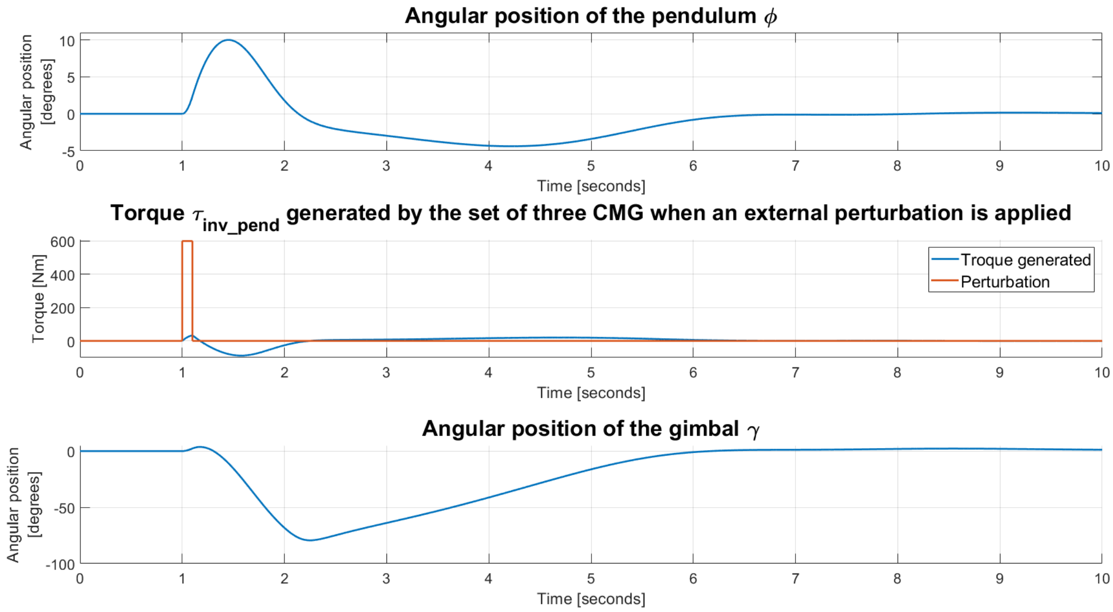

Figure 5.13: System behaviour when an external perturbation of 600 Nm is applied during 0.1 second on the pendulum with the potential field algorithm. The gimbal angular position and the generated torque show the inverse response expected from the positive zero.

5.4 Summary

In this section, the control diagram of the dynamic system and control law was designed based on the information given in the paper published by the team of Prof. Vallery [22]. From the latter, some of the parameters were obtained but three of them needed to be increased, the required gimbal angular velocities were different, and thus the generated torques. The unknown parameters were either obtained from papers or trail and error for the controllers' coefficients. Those parameters are all gathered in Tab.5.4.

In addition, to make the gimbal return to its initial position, a potential field algorithm was integrated into the controller. It added some time for the system to reach the equilibrium state but the CMG is now in the optimal orientation to deal with the next perturbation. Indeed, the transmitted torque is related to the generated torque by the cosine of the gimbal angle.

Finally, the system stability was analyzed by linearizing each block of the diagram and computing the transfer function of the high- and low-level feedback loops. The results showed that the system controlled is stable and present a non-minimum phase behaviour under external perturbations.

Table 5.4: The selected parameters characterizing the models of dynamic systems and controllers.

Parametric variables	Symbols	Values	Units
Mass	m	70	kg
Elder height	h	1.7	m
Height of the CoM	l	0.97	m
Viscous damping	f_ϕ	362.25	Nms/rad
Inertia of the flywheel along the s-axis	I_{W_s}	0.06	kgm^2
Inertia of the CMG along the g-axis	J_g	0.03	kgm^2
Angular speed of the flywheel	Ω	8000	rpm
Virtual spring constant	k_{vs}	1200	Nm/rad
Proportional constant of the PI controller	k_P	40	Nms/rad
Integral constant of the PI controller	k_I	20	Nm/rad
Attractive potential factor	k_{att}	0.4	$1/s$

Chapter 6

Dynamic scaling of the inverted pendulum

Since the objective of this work is to prove the concept that the team of Prof. Vallery designed with a scaled-down system [22], the parameters in Tab.5.4 characterizing a full-scale human must be converted. This model must therefore have the same dynamics as observed in the previous chapter for a mass of about $1\,kg$. Only one parameter should remain constant for design specifications, the angular velocity of the flywheel, $\Omega = 8000\,rpm$.

6.1 Dynamic scaling theory

Scaling a system to a size other than the one intended is particularly challenging, but its complexity is reduced by the use of dynamic scaling. The latter uses a set of relationships that maintains the geometric, kinematic, and dynamic properties between a system and its scaled version without the need for the dynamic model. Moreover, it has the advantages of preserving, among other things, the stability and relative speed of systems [38].

For two systems to be geometrically similar, they must have the same shapes. It implies then for the scaled model to have its dimensions proportional to a constant factor α_L and that all angles are kept the same.

To ensure similar steady-state motions, kinematic similarity requires that a point of the system and its equivalent in the model have scaled velocities and in the same direction. Since a constraint on the distance is already fixed with α_L, a constraint factor on the time α_T is sufficient to satisfy the condition on the velocity.

For the transient response, the dynamic similarity requires for the forces to be scaled by a constant factor α_F.

Depending on the system to scale, other relations can be added to require elastic similarity or stress similarity [38].

In his thesis, Bruce D. Miller [38] explains two approaches to obtain dynamic scaling relations.

The intuitive one focuses on the force-balance approach that compares two similar dynamic systems. The scaling factors are therefore obtained by comparing the two equations to find the relationships, which can be tedious.

The second method is based on the dimensional analysis of fundamental physical quantities such as length, time, and force. From the latter three, the scaling factors of all the other system variables are obtained.

In Tab.6.1, one can see the parameters that needs to be down scaled with their units expressed in the three fundamental quantities; F for newton, L for meter, and T for second.

Table 6.1: The parameters to scale and their dimensions expressed with the fundamental quantities selected; F for newton, L for meter, and T for second.

Parametric variables	Symbols	Units	Dimensions in fundamental quantities
Mass	m	kg	$FL^{-1}T^2$
Height of the CoM	l	m	L
Viscous damping	f_ϕ	Nms/rad	FLT
Inertia of the flywheel along the s-axis	I_{W_s}	kgm^2	FLT^2
Inertia of the CMG along the g-axis	J_g	kgm^2	FLT^2
Angular speed of the flywheel	Ω	rad/s	T^{-1}

While the gravity applied on the ground is the same for the system and its scaled model, its dimension in fundamental quantities, LT^{-2}, says otherwise. With the latter giving the scaling relation, it needs to be equal to 1 for the gravity to remain constant. Therefore, the latter is constrained to be scale independent leading to $\alpha_L = \alpha_T^2$.

A second constraint arises when both systems are made of the same materials and thus have the same density. Therefore, a new relation to simplify the scaling factors is obtained: $\alpha_F = \alpha_L^3$ [38].

6.2 Dynamic scaling of the system

With the constraints applied on the dimensions in Tab.6.1, a table with the scaling factors of several parameters is build and depicted in Fig.6.1.

The objective for the scaled pendulum is to reduce the weight from $70\,kg$ to approximately $1\,kg$. Thus, with the mass scaling relation, the length factor is found.

$$m_{scaled\_pend} = \alpha_L^3 m_{pend}$$
$$\alpha_L = 0.2426$$

Therefore, the variables of the pendulum and CMG that need to be scaled, are computed using the relations established in Fig.6.1. In Tab.6.2 are gathered those parameters with their normal and scaled values as their scaling relations.

Quantity	Units	Scale Factor
Basic variables		
length	L	L
time	T	$L^{1/2}$
force	F	L^3
torque	FL	L^4
Motion variables		
displacement	L	L
velocity	LT^{-1}	$L^{1/2}$
acceleration	LT^{-2}	1
angular displacement	-	1
angular velocity	T^{-1}	$L^{-1/2}$
angular acceleration	T^{-2}	L^{-1}
Mechanical parameters		
mass	$FL^{-1}T^2$	L^3
stiffness	FL^{-1}	L^2
damping	$FL^{-1}T$	$L^{5/2}$
moment of inertia	FLT^2	L^5
torsional stiffness	FL	L^4
torsional damping	FLT	$L^{9/2}$

Table 1: Scaling rules that preserve geometric similarity. If a system is scaled in size by a factor L and its mechanical parameters are each scaled according to the table, then the motion of the scaled system can be found from the motion of the original unscaled system. The table is derived assuming uniform scaling in all dimensions (geometric similarity), and that the acceleration of gravity is invariant to scale.

Figure 6.1: Dynamic scaling factors for different physical quantities simplified with the two constraints aforementioned (Reproduced from [39]).

Table 6.2: The parameters with their normal and scaled values, and the scaling relations used to compute them.

Parametric variables	Symbols	Normal values	Scaling factors	Scaled values
Mass $[kg]$	m	70	L^3	1
Height of the CoM $[m]$	l	0.97	L	0.235
Viscous damping $[Nm\,s/rad]$	f_ϕ	362.25	$L^{9/2}$	0.62
Inertia of the flywheel along the s-axis $[kg\,m^2]$	I_{W_s}	3×0.06*	L^5	1.5E−04
Inertia of the CMG along the g-axis $[kg\,m^2]$	J_g	3×0.03*	L^5	7.6E−05
Angular speed of the flywheel $[rad/s]$	Ω	837.76	$L^{-1/2}$	1700

* The inertia are multiplied by three as there are three CMGs in the full-scale model.

The normalized expression of the viscous damping could have been used to compute it using the scaled values of the mass and height. As a reminder, in a paper by M. Cenciarini [29], they found that elderly have a viscous damping normalized by the body inertia of $5.5\,s^{-1}$. For a pendulum, the expression of the inertia is ml^2.

Using this relation, the viscous damping equals $0.3\,Nm\,s/rad$ which is half of the one obtained from the dynamic scaling relation. By looking at the damping ratio, the latter has been reduced to 0.43 by using this expression while with the scaled viscous damping, the ratio of 0.86 is conserved. The value of $0.62\,Nm\,s/rad$ is thus kept.

Also, it was decided to keep the same angular velocity of the flywheel. With the latter smaller than the one obtained with the scaling factor, the inertia of the flywheel and consequently the one of the CMG must increase.

For the controller to work with $\Omega = 8000\,rpm$, the inertias have become:

$$I_{W_s} = 5\text{E}{-}04 \qquad\qquad J_g = 2.5\text{E}{-}04$$

In the following development, the values of the parameters gathered in Tab.6.2 will be referred to as the *scaled parameters*. While those obtained to maintain the angular velocity Ω will be referred to as the *scaled parameters modified*. The latter differs from the first one by the value of Ω but also the inertia of the wheel I_{W_s} and the CMG J_g.

For the controller coefficients, the high-level parameter k_{vs} was obtained by matching as closely as possible the transient responses of the full-scale and scaled pendulum. The control diagram used did not include the low-level controller, and the result is depicted in Fig.11.3 in Appendix Section 11.3.

$$k_{vs} = 3.25$$

The PI controller coefficients of the scaled pendulum were determined in the same way than those of the full-scale pendulum, by trail and error. The values of the coefficients for both scaled pendulum are:

Scaled parameters:

$$k_P = 0.13 \qquad\qquad k_I = 0.1$$

Scaled parameters modified:

$$k_P = 0.87 \qquad\qquad k_I = 2$$

In Fig.6.2 is depicted the behaviour of the scaled pendulum initially tilted by 10 degrees with the scaled parameters and the ones modified.

One can see that the gimbal angular position almost reaches the singularity with the scaled parameters while with the modified ones, the amplitude of the peak is divided by 2. This situation is preferable and comes from an oversizing of the wheel's inertia.

The torques generated to bring the pendulum back are close in both cases.

The transient responses of the pendulum angular position show overshoots in both cases and a similar response time.

The answers of both versions to a perturbation with the potential field algorithm are depicted in Fig.11.4 in Appendix Section 11.4.

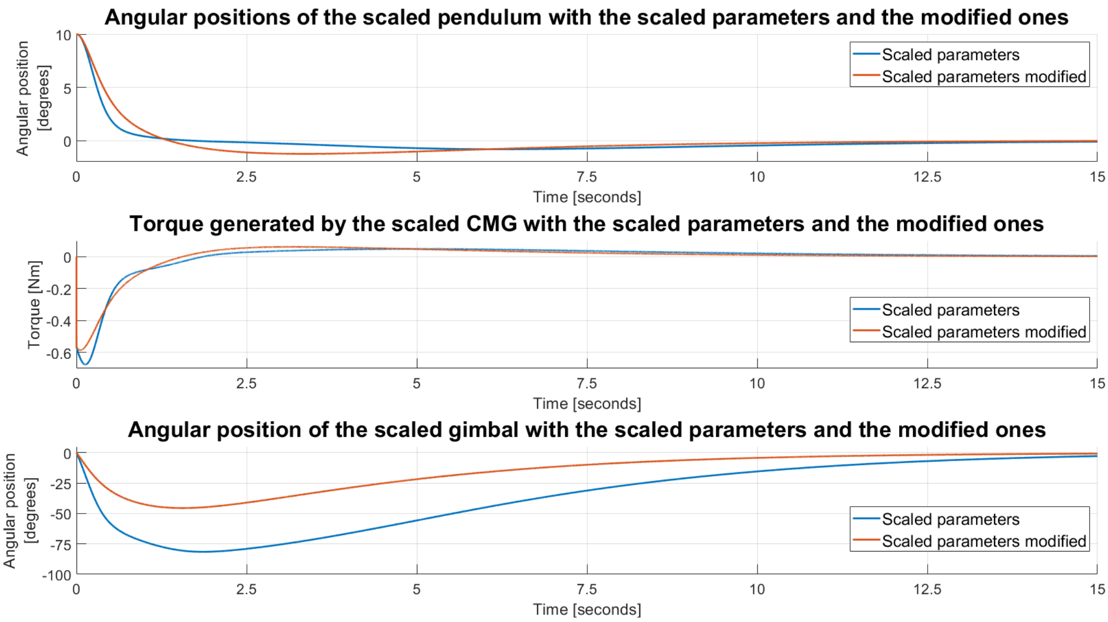

Figure 6.2: Comparison of the scaled pendulum controllers implemented with the scaled parameter and the modified ones.

6.3 Summary

In this chapter, the theory of dynamic scaling was introduced and the different scaling relations were derived based on two constraints. The first one was about the gravity applied on both systems that is the same at the surface of the earth. The second constraint regarded was the density of the full-scale and scaled systems that should be the same if the same materials are used.

With those relations and from the previous chapter, the parameters of the dynamic systems to control were scaled to respect a specification on weight, from 70kg to 1kg. Nevertheless, a second set of scaled values were derived as it was desired to keep the angular velocity of the flywheel constant, $\Omega = 8000$ rpm.

Then, the coefficients of the controller were obtained. The one of the virtual spring by matching the full-scale and scaled pendulums behaviours, and the other two by trail and error.

Finally, the values of the second set of parameters are gathered in tab.6.3 and will be used as constraints for the mechanical design in the next chapter.

Table 6.3: The selected scaled parameters used for the control of dynamic systems and later for the design.

Parametric variables	Symbols	Values	Units
Mass	m	1	kg
Height of the CoM	l	0.235	m
Viscous damping	f_ϕ	0.62	$Nm\,s/rad$
Inertia of the flywheel along the s-axis	I_{W_s}	5E−04	$kg\,m^2$
Inertia of the CMG along the g-axis	J_g	2.5E−04	$kg\,m^2$
Angular speed of the flywheel	Ω	8000	rpm
Virtual spring constant	k_{vs}	3.25	Nm/rad
Proportional constant of the PI controller	k_P	0.87	$Nm\,s/rad$
Integral constant of the PI controller	k_I	2	Nm/rad

Chapter 7

Mechanical design of the inverted pendulum and CMG components

With the different parameters characterizing the pendulum and CMG obtained, the mechanical design process can be conducted. In this chapter, the methodology taught in the course of *Machine Design*, LMECA2801 at UCLouvain, will be strictly followed. Moreover, the reference book of *Machine Component Design* will be used in the dimensioning process of mechanical parts [40].

Once the problem thoroughly stated, the specifications of the device will be reviewed. In the case of this master thesis, no functional graph is needed as the design choice is already made. Then, the most suitable design for the requirements will be selected and drawn by performing morphological graph analysis.

Then the internal loads will be computed to be used for the mechanical dimensioning.

7.1 Problem statement

The device to design is an inverted pendulum mounted with a Control Moment Gyro that aims to model the down-scaled human body. Its purpose is to prove that CMG technology is relevant to actively prevent incipient falls in the elderly without being cumbersome. Indeed, the technology developed by the team of Prof. Vallery at TUDelft takes the form of a wearable backpack-like with a set of CMGs [2].

7.2 Technical specifications of the device

Context:	Design of a CMG to prevent an inverted pendulum to fall	
Date		
Main Function		
10/07	MF1:	Maintain the pendulum vertically
Functional requirements: criteria and levels		
10/07	FR1.1:	Able to reorient the pendulum initially tilted by 10 degrees
10/07	FR1.2:	Able to reorient the pendulum under external perturbations up to 1.1 Nm (tilted up to by 10 degrees)
Constraints		
10/07	C1:	Use only one CMG
10/07	C2:	Limit range for the gimbal angular position
10/07	C3:	Reproduce human viscous damping on a reduced scale
10/07	C4:	Correspond to a down-scaled version of the human body
10/07	C5:	Material selection
Constraint Requirement: criteria and levels		
10/07	C1.1:	Flywheel inertia of 5E−04 $kg\,m^2$ along its spinning axis
10/07	C1.2:	CMG inertia of 2.5E−04 $kg\,m^2$ along the gimbal spinning axis
10/07	C1.3:	Flywheel angular velocity of 8000 rpm
10/07	C2.1:	Range for the angular position of ±60 degrees
10/07	C3.1:	Viscous damping of the 0.62 $Nm\,s/rad$
10/07	C4.1:	System overall weight of ±1 kg
10/07	C4.1:	Pendulum center of mass height of ±0.24 cm
10/07	C5.1:	Use of raw materials

7.3 Morphological graph

	1	2	3
CMG mounting	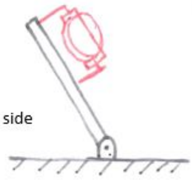 Lateral side	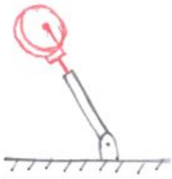 On top	
Gimbal shape	 U/N shape	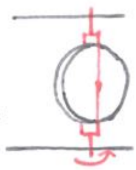 O shape	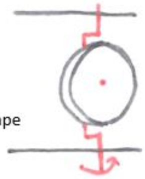 C shape
Motor transmission	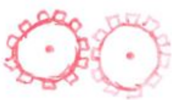 Gear	 Key hole on shaft	
Flywheel transmission	 Key	 Spline shaft	 Clamping screw

7.3.1 Definition of criteria and rating scale

Depending on the technical function, the following criteria will be applied to select the most appropriate design.

- **Alignment accuracy (3):** Accuracy of CMG rotation axis alignments.
- **Implementation (2):** Complexity of the system to design.
- **Bulk (1):** Space required by the function to integrate.
- **Conformity (3):** How close the function is to the device on which it is based.
- **Quality of the transmission (1):** Amount of mechanical play.

The assessment of the solutions is made with the following relative scale: $-$, 0, $+$

7.3.2 Fixation of the CMG on the pendulum

Table 7.1: Assessment of the solutions for the CMG mounting type.

Criteria	Lateral side	On top
Conformity (3)	0	$-$
Bulk (1)	0	$+$
Implementation (2)	0	$-$
Total	0	-4

Justifications:

- Conformity: The objective of this technology is to take the form of a wearable device like a backpack. Therefore, fixing the CMG on the side of the pendulum is more conform to the end goal of the technology than if it was placed at the tip of the pendulum. The CMG will be off-centered from the human head-toe axis like a backpack is.
- Bulk: With the CMG mounted at the tip of the pendulum, the design will have to be more compact and use fewer parts. Indeed, fixed on the side, the device will need additional parts to maintain it in place and aligned.
- Complexity: With the CMG placed on top of the pendulum, the complexity increases to respect the alignment and rigidity of the system as the available surface for the fixation is reduced or more complex to reach.

7.3.3 Selection of the gimbal shape

Table 7.2: Assessment of the solutions for the gimbal shape.

Criteria	U/N shape	O shape	C shape
Alignment accuracy (3)	0	$+$	0
Bulk (1)	0	$-$	$-$
Implementation (2)	0	$+$	0
Total	0	4	-1

Justifications

- Alignment accuracy: For the O-shape, the alignment of the shafts is optimal and ensured by two sets of bearings placed at the ends of rods. For the C-and U/N-shapes, one of the two shafts has single side support that would require mounting the wheel on the actuator axis which is not recommended because of the device size. The second option would be to place a larger set of bearings relatively close to each other to support and align the shafts.

- Bulk: Compared to the other design, the U/N-shape with its half gimbal requires fewer parts and is, therefore, less bulky. With the C-shape also corresponding to a half gimbal, the latter still requires almost as many parts as the O-shape design.

- Implementation: Both U/N-shape and C-shape are more complex to design because of the half gimbal used while the O-shape is fixed from both sides of both rotating axes.

7.3.4 Selection of the motors transmission

Table 7.3: Assessment of the solutions for the motors transmission.

Criteria	Gears	Key hole in the shaft
Implementation (2)	0	$-$
Bulk (1)	0	$+$
Total	0	-1

Justifications

- Implementation: While using gear is straightforward with the actuator on a different axis than the shaft, the direct transmission from the actuator to the shaft implies more constraints that can require the addition of an elastic coupling.

- Bulk: The actuator mounted on the shaft makes it more difficult but space is gained with both on the same axis.

7.3.5 Selection of the flywheel transmission

Table 7.4: Assessment of the solutions for the flywheel transmission.

Criteria	Key	Spline shaft	Clamping screw
Quality of the transmission (1)	0	$+$	$-$
Total	0	$+1$	-1

Justifications

- Quality of the transmission: The spline shaft is the design that offers lesser play because the contact surface is larger with the tooth meshing. It also has a superior load transmission than other techniques. The clamping screw is the design that has the most play while the use of a key reduces it, but the transmission quality is not as high as with the spline shaft and is more subject to wear and fatigue failure.

7.4 Concepts

For this section, three concepts of what could the CMG looks like and how it could be fixed on the pendulum were drawn and depicted in Fig.7.1-7.3.

The first concept in Fig.7.1 is a design with the CMG mounted on the side of the pendulum with an O-shape gimbal. The type of motor transmission for both shafts is gears, and a spline shaft is used for the flywheel transmission.

The second concept in Fig.7.2 is a design with the CMG mounted on top of the pendulum with a U/N-shape gimbal. Both types of motor transmissions are used, and the flywheel transmission is ensured with a spline shaft.

The third concept in Fig.7.3 is a design with the CMG mounted on the side of the pendulum with a C-shape gimbal. Both types of motor transmissions are used and the flywheel transmission is ensured with a key.

The assessment of the concepts uses the criteria and scale defined in the previous section.

Table 7.5: Assessment of the concepts presented in Fig.7.1-7.3.

Criteria	Concept 1	Concept 2	Concept 3
Alignment accuracy (3)	0	0	$-$
Implementation (2)	0	$-$	$-$
Bulk (1)	0	$+$	0
Conformity (3)	0	$-$	$+$
Quality of the transmission (1)	0	0	$-$
Total	0	-4	-3

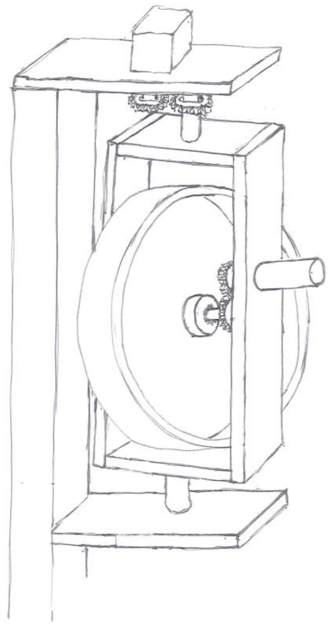

Figure 7.1: The first concept is made of the following functions: CMG mounted on the lateral side; an O-shape gimbal; motors transmissions with gears; and flywheel transmission with a spline shaft.

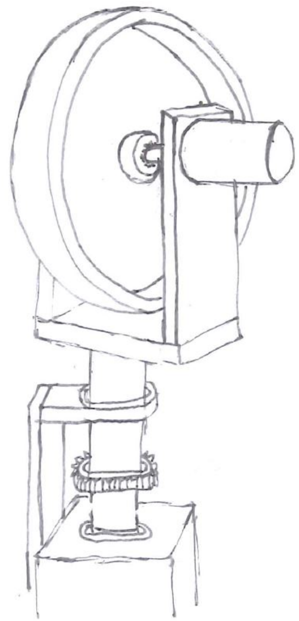

Figure 7.2: The second concept is made of the following functions: CMG mounted on top; a U-shape gimbal; both motor transmissions; and flywheel transmission with a spline shaft.

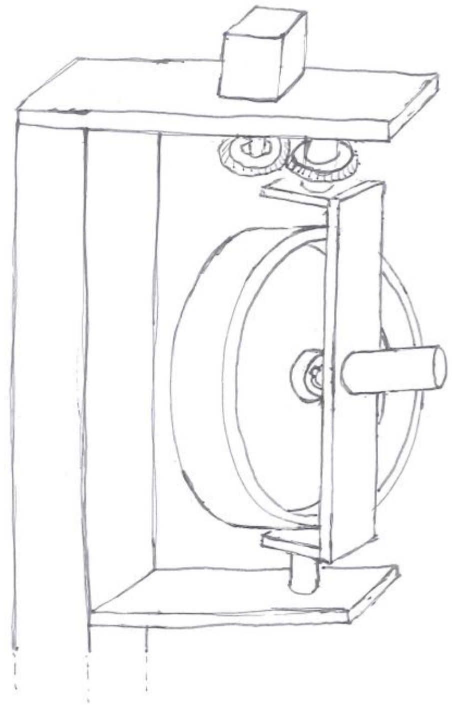

Figure 7.3: The third concept is made of the following functions: CMG mounted on the lateral side; a C-shape gimbal; both motor transmissions; and flywheel transmission with a key.

Justifications

- Alignment accuracy: The first two concepts are considered to have the same quality of alignment because of their use of 2 sets of bearings for the shafts. The third one has an alignment accuracy lower as the flywheel is directly mounted on the actuator.

- Implementation: The added complexity for the second concept lies in the alignment and fixation of the gimbal while for concept 3, the flywheel actuation is more complex.

- Bulk: From the drawings, concept 2 is the design that takes the fewer space. Concept 3 is considered as bulky as concept 1 because of the fixation type to the pendulum. Not much space is gained with the half gimbal in this configuration.

- Conformity: As explained in the previous justifications, the objective of this technology is to be worn as a backpack. Therefore the concept 2 with the CMG on top of the pendulum is not conform compared to concepts 1 and 2.

- Quality of the transmission: The use of spline shafts in concepts 1 and 2 allows the least play because the tooth surface meshed. Compared to concept 3, the use of a key increases the play between mechanical parts and is more subject to wear and fatigue failure.

7.5 Final solution

The final solution obtained after the assessment of the morphological chart and several concepts is as follow:

- The CMG is mounted on the lateral side of the pendulum.

- The gimbal is designed with an O-shape.

- The torque transmission of the actuator to the shafts is ensured by gears.

- The flywheel is actuated by the mean of a spline shaft.

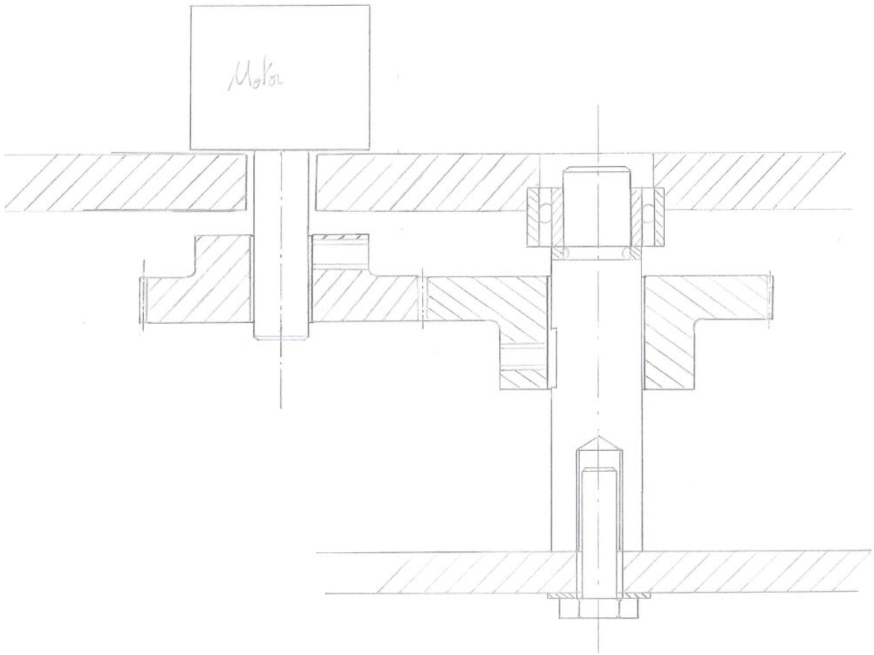

Figure 7.4: Technical drawing of the shaft at the top of the gimbal screwed to the frame. It is maintained and aligned by a ball bearing on this side and a gear attached with a clamping screw transmit the torque from the actuator. An adjustment disk is also used.

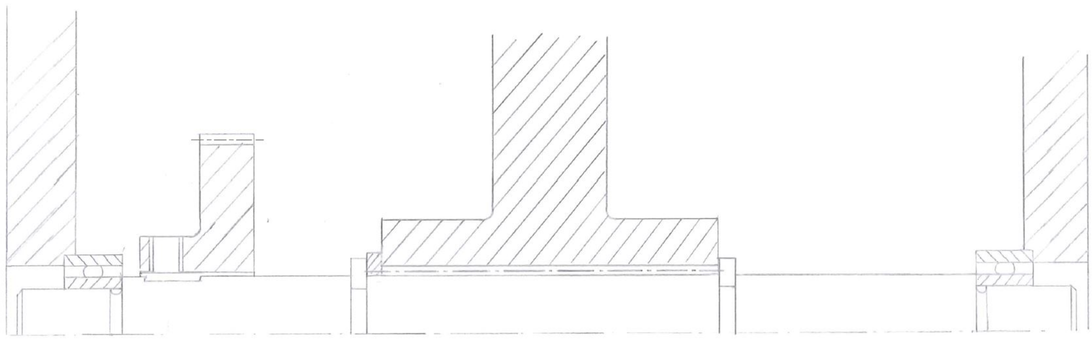

Figure 7.5: Technical drawing of the spline shaft with the flywheel maintained in position with two snap rings and an adjustment disk. It is maintained and aligned by a set of ball bearings at each side and a gear attached with a clamping screw transmit the torque from the actuator.

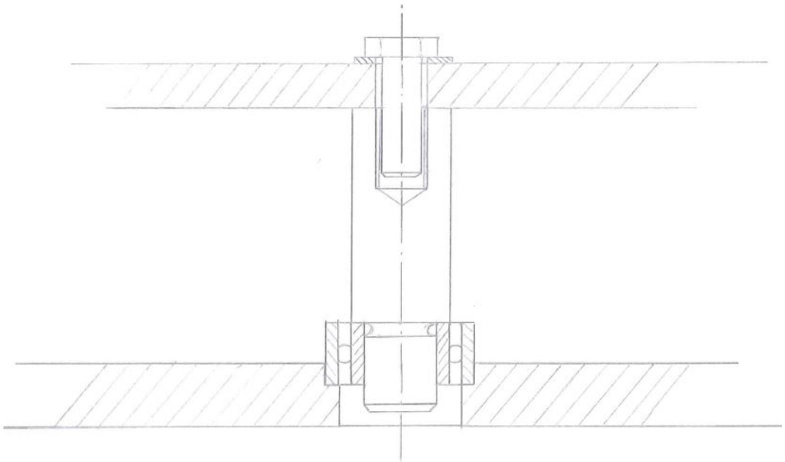

Figure 7.6: Technical drawing of the shaft at the bottom of the gimbal screwed to the frame. It is maintained and aligned by a ball bearing on this side.

7.6 Kinematic chain and free-body analysis

In Fig.7.7-7.8 are depicted the kinematic chain of the spline shaft and gimbal shaft respectively. The free-body analysis are depicted in Appendix Section 11.5-11.6.

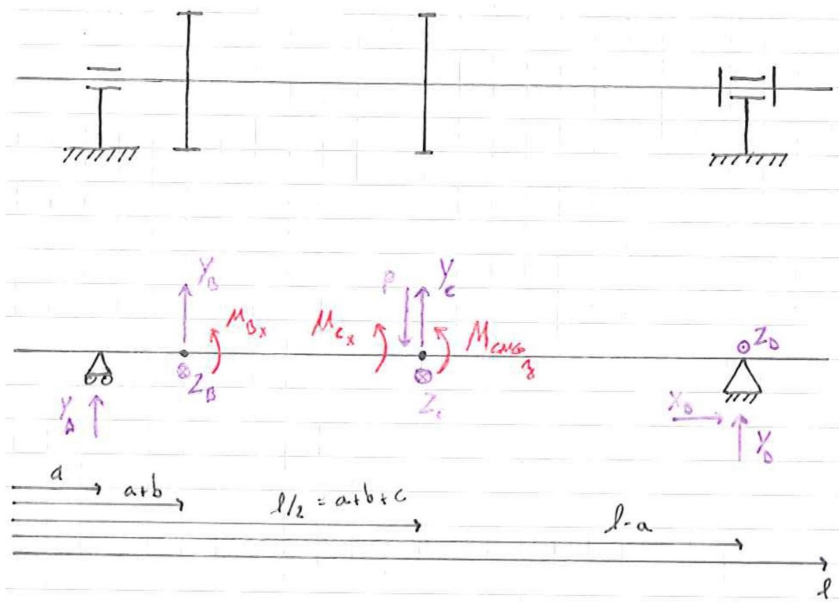

Figure 7.7: Kinematic chain of the spline shaft with: $a = 5\,mm$; $b = 5\,mm$; $c = 20\,mm$; $l = 60\,mm$

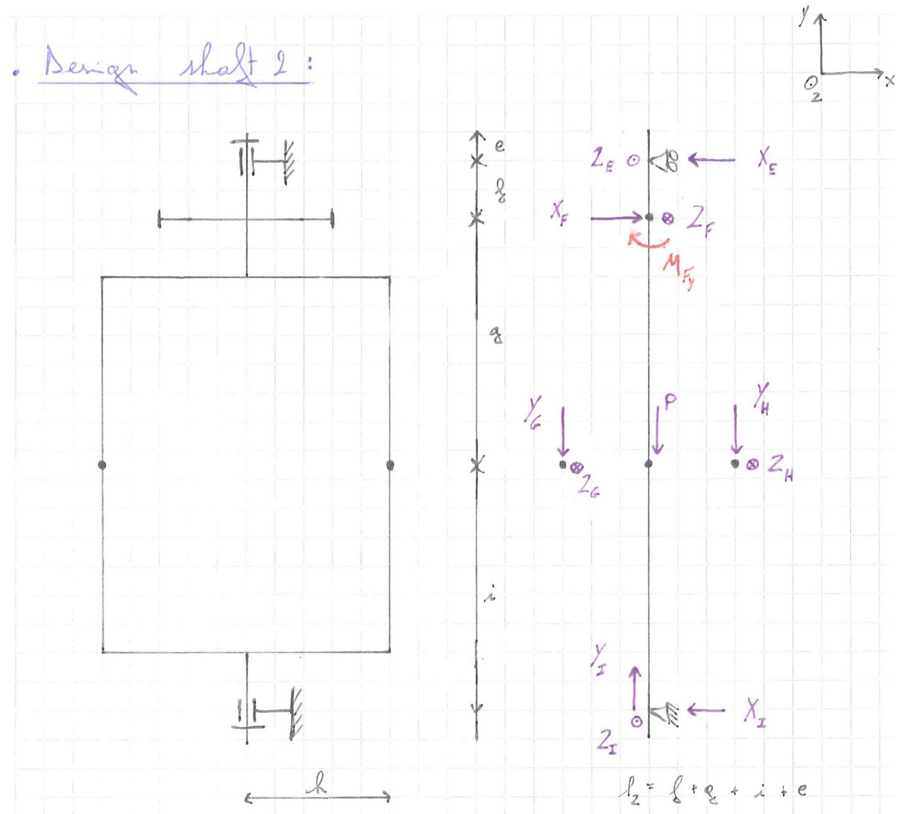

Figure 7.8: Kinematic chain of the gimbal shaft with: $e = 5\,mm$; $f = 5\,mm$; $g = 60\,mm$; $h = 25\,mm$; $i = 60\,mm$

With the relations derived from the equilibrium equations and the free-body analysis, the values of the different forces are computed. Nevertheless, there are two cases considered to compute the forces. One is when the gimbal is locked and the wheel is settling from rest to 8000 rpm; the other is when the wheel has reached its speed and the control of the CMG is activated, the torque generated to maintain the wheel velocity is then assumed negligible.

General parameters selection

The safety factor S_f was set to 2 because the environment in which the pendulum operates is controlled, and the loads are determined. Also, the material properties are well known justifying the choice of S_f.

From Tab.6.3, the inertia of one axis of the wheel is given and with it, the first sketch of its design was made to estimate its weight around 400 grams.

7.6.1 Spline shaft: loading diagram

To solve the equations, the radius of the shaft and the gear have both needed to be estimated to $0.005\,m$ and $0.01\,m$.

From Fig.6.2, one can see that for the pendulum initially tilted by 10 degrees, the generated torque is approximately equal to $0.6\,Nm$. Therefore, M_{CMGz} is equal to $\tau_{CMG} * S_f = 1.2\,Nm$

Also, the torque needed to reach 8000 rpm depends on the time the actuator has to accelerate the wheel. After trial and error with the actuator selection, the settling time is set to $30 seconds$. The torque M_{Cx} required to accelerate the flywheel up to 8000 rpm is equal to $0.028\,Nm$ and is obtained using the inertia I_{Ws}, the acceleration, and the safety factor.

The values of the forces are gathered in Tab.7.6 and the loading diagrams are depicted in Fig.7.9.

Force	Case 1 $[N]$	Case 2 $[N]$
Y_A	-2.37	22.04
Y_B	1.02	0
Y_C	2.91	3.92
Y_D	-1.56	-25.96
Z_A	1.12	0
Z_B	2.79	0
Z_C	-2.79	0
Z_D	-1.12	0

Table 7.6: Values of the different forces acting on the spline shaft stirring the flywheel in both considered cases.

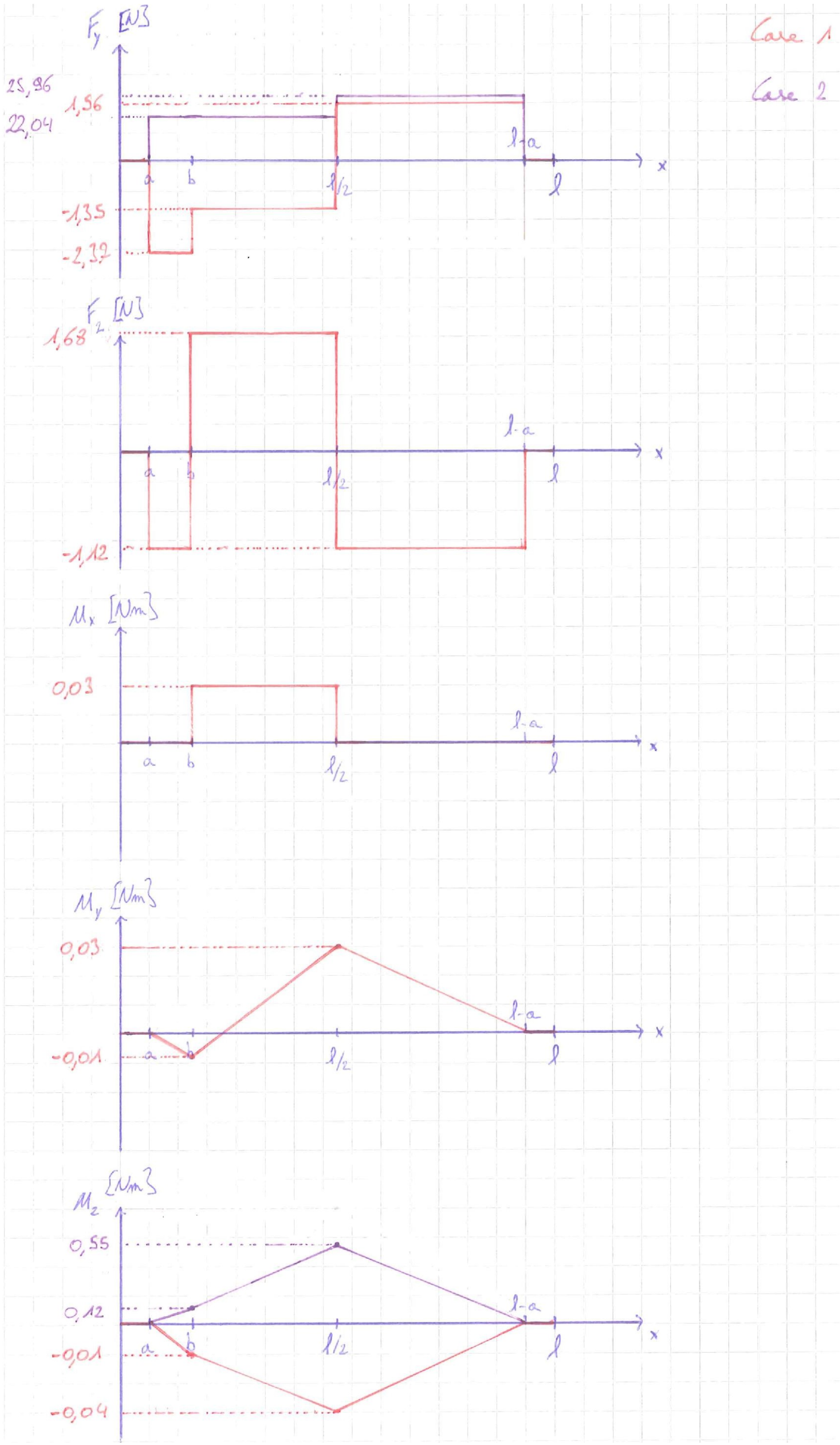

Figure 7.9: Loading diagram of the spline shaft with in red, case 1, and in purple, case 2.

7.6.2 Gimbal shaft: loading diagram

To solve the equations, the radius of the shaft and the gear have both needed to be estimated to $0.004\,m$ and $0.008\,m$.

From the same simulation with the results depicted in Fig.6.2, the torque τ_{GM} of the gimbal reached a value of $0.12\,Nm$. With the safety factor applied, M_{Fy} is equal to $0.24\,Nm$.

With a wheel weighing approximately 0.4 kg, the gimbal weight was assumed to 0.5 kg.

The values of the forces are gathered in Tab.7.7 and the loading diagrams are depicted in Fig.7.10.

Force	Case 1 $[N]$	Case 2 $[N]$
X_E	-2.74	-1.03
X_F	-3.06	10.92
X_I	-0.32	11.96
Y_G	-2.37	22.04
Y_H	-1.56	-25.96
Y_I	0.98	0.99
P	4.91	4.91
Z_E	-8.06	28.8
Z_F	-8.4	30
Z_G	1.12	-4
Z_H	-1.12	4
Z_I	-0.34	1.2

Table 7.7: Values of the different forces acting on the gimbal shaft in both considered cases.

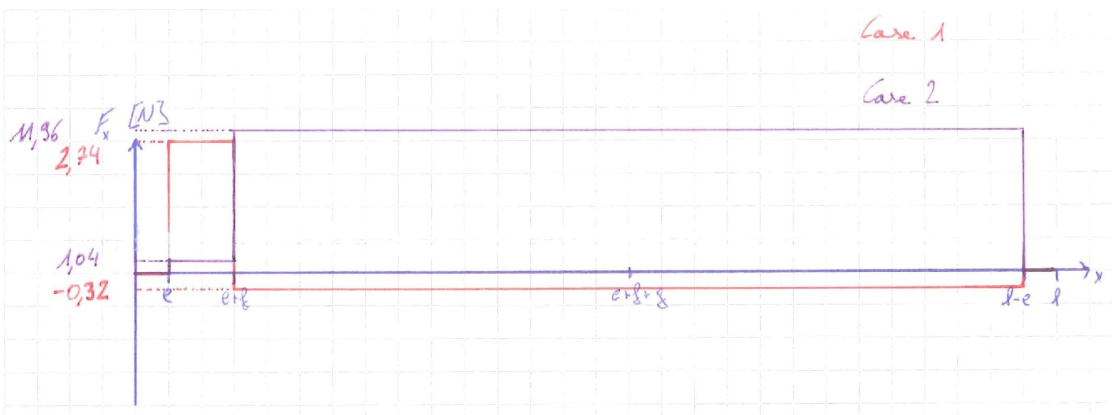

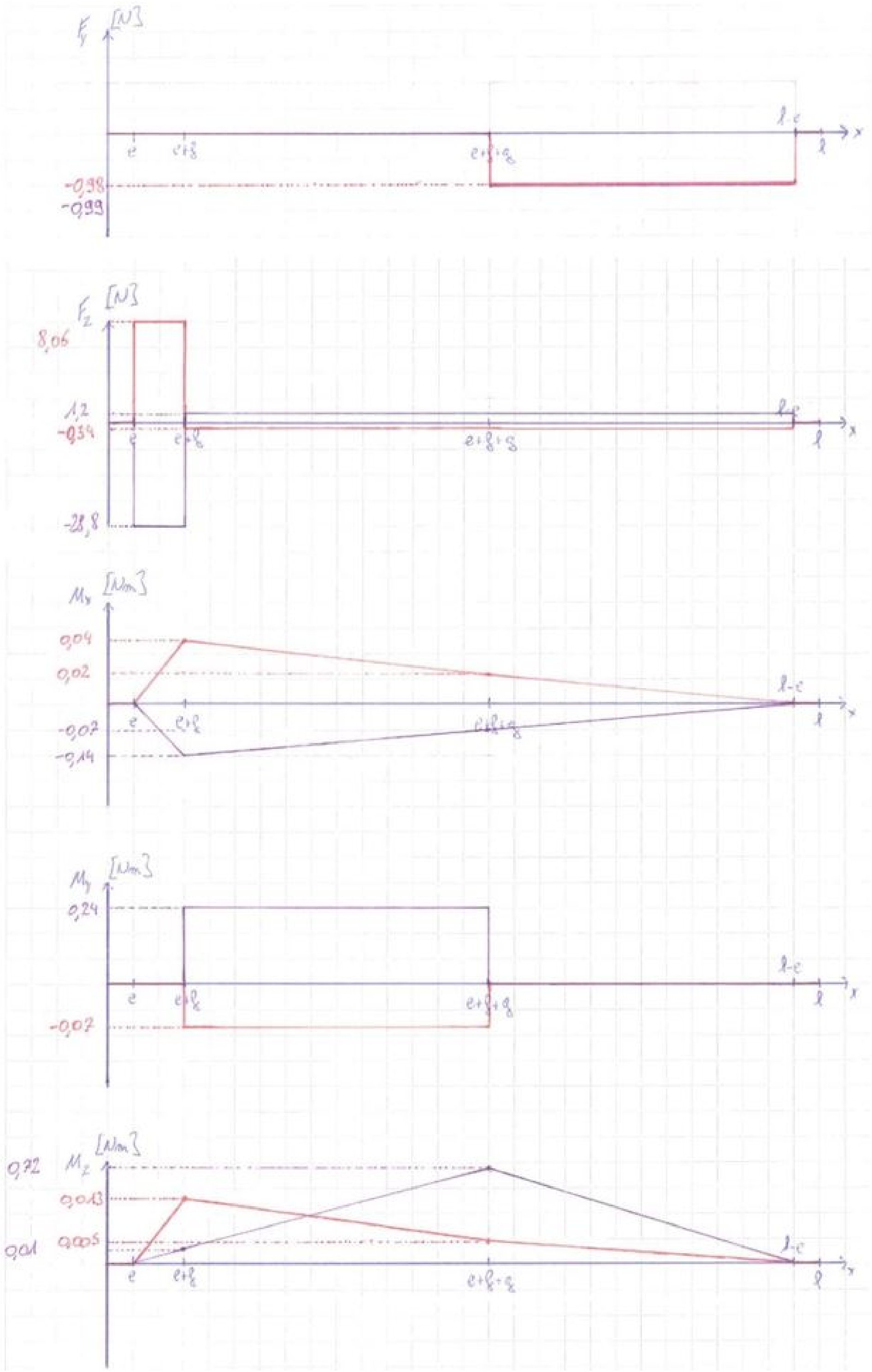

Figure 7.10: Loading diagram of the gimbal shaft with in red, case 1, and in purple, case 2.

7.7 Parts dimensioning

7.7.1 Spline shaft dimensioning

The material selected for the shaft is stainless steel 304A which is commonly used for this kind of application.

From the loading diagram, one can see that the momentums at the shoulders are equal to zero where the stress concentration usually is. Nevertheless, as drawn in Fig.7.5, the flywheel is axially maintained with two circlips which is acceptable as there are no axial forces applied. Therefore, the maximal stress location is at one of the two. For further developments, the momentums at $l/2$ are used as if they were applied at the circlip position.

Static load

The nominal bending stress is computed with the equation 4.8 p.138 from the reference book [40] and can be reduced to:

$$\sigma_{nom} = \frac{32\sqrt{M_y^2 + M_z^2}}{\pi D^3} = \frac{0.488}{D^3}$$

The nominal torsion stress is computed with the equation 4.4 p.135 of the same book and can be reduced to:

$$\tau_{nom} = \frac{16M_x}{\pi D^3} = \frac{0.142}{D^3}$$

The values of the momentums obtained in Case 1 are used here.

To resist in static, the Von Mises equivalent stress relation below is compared to the yield strength of the material giving the minimal diameter acceptable. The yield strength of stainless steel 304A is equal to 276 MPa. No safety factor is applied to it as one was already used on the forces and momentum.

$$\sigma_{yield} = \sqrt{\sigma_{max}^2 + 3\tau_{max}^2}$$

The maximal bending and torsion stresses are obtained from their nominal values by multiplying them with their respective stress concentration factors K_{t_b} and K_{t_t}.

From the drawing book "*Méthode active de dessin technique*" [41], the groove for a shaft with a diameter of 10 mm is 0.4 mm deep. The ratio between the shaft diameter D and the smaller diameter d is equal to 1.04. From the design book [40], the value for the stress concentration factors in bending and torsion are found in Fig.4.36 p.164 with a radius r the smallest possible.

$$K_{t\_b} = 3 \qquad\qquad K_{t\_t} = 2$$

The Von Mises relation can now be solved to find:

$$\begin{aligned} \sigma_{yield} &= \sqrt{\sigma_{max}^2 + 3\tau_{max}^2} \\ D &= \left(\frac{(\sigma_{nom} * K_{t\_b})^2 + 3 * (\tau_{nom} * K_{t\_t})^2}{\sigma_{yield}}\right)^{1/6} \\ &= 0.0018\ \mathrm{m} \end{aligned}$$

With the values from Case 2, the minimal diameter D is 0.0039.

Fatigue analysis

For the fatigue in bending, the endurance limit S_n is first computed with the following relation:

$$S_n = S_n' C_L C_G C_S C_T C_R$$

The parameter S_n' is the R.R. Moore endurance limit and is equal to half of the ultimate tensile strength. The load factor C_L and the gradient factor are equal to 1 in bending and for a shaft smaller than 10 mm. The surface factor C_s is equal to 0.9 to have the shaft commercially polished and the temperature factor C_T is equal to 1. To have a 99% reliability, the factor C_R is set to 0.814. The endurance limit is thus equal to:

$$\begin{aligned} S_n &= 286 * 1 * 1 * 0.9 * 1 * 0.814 \\ &= 210\ MPa \end{aligned}$$

For the fatigue analysis, the fatigue stress concentration factor K_f needs to be found. Using the relation 8.2 p.335 in the design book [40], their expression are obtained.

$$
\begin{aligned}
K_{f\_b} &= 1 + (K_{t\_b} - 1)q_b & K_{f\_t} &= 1 + (K_{t\_t} - 1)q_t \\
&= 1.92 & &= 1.54
\end{aligned}
$$

with $q_b = 0.46$ and $q_t = 0.54$. Now, the equivalent alternating stress σ_{ea} and the equivalent mean stress σ_{em} can be computed.

$$
\begin{aligned}
\sigma_{ea} &= K_{f\_b}\frac{32\sqrt{M_y^2 + M_z^2}}{\pi d^3} & \tau_{em} &= K_{f\_t}\frac{16M_x}{\pi d^3} \\
&= \frac{0.94}{d^3} & &= \frac{0.22}{d^3}
\end{aligned}
$$

To find the value of σ_{ea}, its ratio with σ_{em} equal to 4.27 is used in the fatigue diagram depicted in Fig.7.11. The design overload point is at 193 MPa.

With σ_{ea} found, the minimal diameter can be computed using:

$$
\begin{aligned}
\sigma_{ea} &= \frac{0.94}{d^3} = 193 * 10^6 \\
d &= 0.0017 \qquad \text{with} \quad D = 1.04\,d
\end{aligned}
$$

The minimal diameter D is thus 0.0018. The same procedure was repeated with the values of Case 2 and the minimal diameter for D is 0.0039.

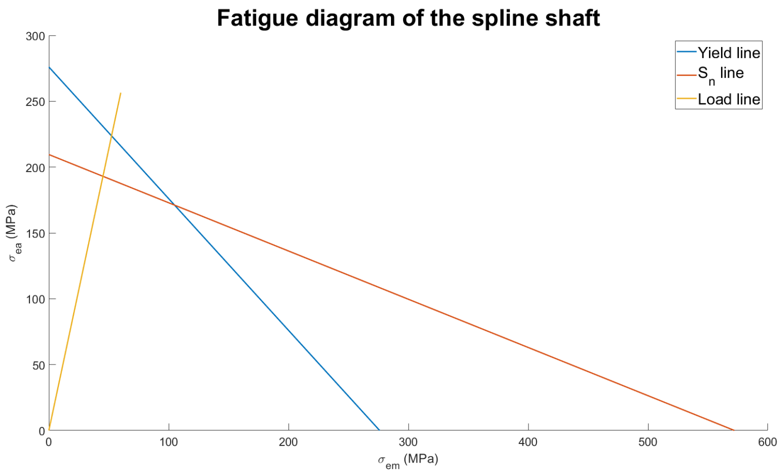

Figure 7.11: Fatigue diagram of the spline shaft using the values of Case 1.

Selection of the spline shaft

From the results, the shaft diameter must be greater than 4 mm which is less than what was initially assumed, thus its size can be reduced.

By looking in the manufacturer catalog, a spline shaft with a diameter of 8 mm is found as depicted in Fig.7.12 at Misumi. Its particularity is that the shaft comes with a flange that can be fixed with a clamping screw. Therefore, there is no more need for the two grooves for the circlips. Also, the shaft is two-side stepped with a smaller diameter of 6 mm.

Moreover, a wrench flat can be added for the spur gear to be fixed.

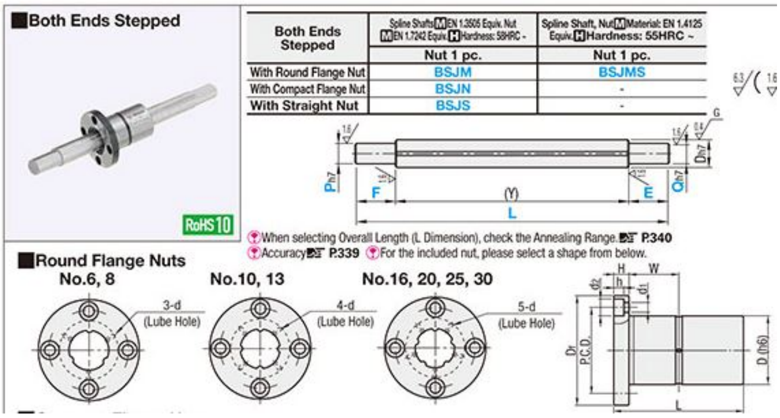

Figure 7.12: Screenshot from the catalog of the selected shaft.

7.7.2 Gimbal shaft dimensioning

The material selected for the shaft is stainless steel 304A which is commonly used for this kind of application.

From the loading diagram, one can see that the momentums at the shoulders are equal to zero where the stress concentration usually is. The static analysis is thus performed where the maximal stress location is, at $e + f + g$ where the spline shaft is fixed. The fatigue analysis makes no sense as the gimbal does not rotate constantly.

Static load

Using the same relations as in the previous section, the nominal bending stress is computed and can be reduced to:

$$\sigma_{nom} = \frac{32\sqrt{M_x^2 + M_z^2}}{\pi D^3} = \frac{0.21}{D^3}$$

The nominal torsion stress is computed with the equation 4.4 p.135 of the same book and can be reduced to:

$$\tau_{nom} = \frac{16 M_y}{\pi D^3} = 0$$

Unlike for the spline shaft, the momentums used in each stress equation are not the same because of the axes change. The values of the momentum obtained in Case 1 are used here.

To resist in static, the Von Mises equivalent stress relation below is compared to the yield strength of the material giving the minimal diameter acceptable. The yield strength of stainless steel 304A is equal to 276 MPa. No safety factor is applied to it as one was already used on the forces and momentum.

$$\sigma_{yield} = \sqrt{\sigma_{max}^2 + 3\tau_{max}^2}$$

Because there are no shoulder nor groove, the nominal values of the stresses are used as the maximal values in the equation above.

The Von Mises relation gives then:

$$\begin{aligned} \sigma_{yield} &= \sqrt{\sigma_{max}^2 + 3\tau_{max}^2} \\ D &= \left(\frac{\sigma_{nom}^2 + 3 * \tau_{nom}^2}{\sigma_{yield}} \right)^{1/6} \\ &= 0.0009 \text{ m} \end{aligned}$$

With the values from Case 2, the minimal diameter D is 0.003.

Selection of the gimbal shaft

From the results, the shaft diameter must be greater than 3 mm which is less than what was initially assumed and its size can be reduced.

Nevertheless, because of the shaft design, shape, and size, it was decided that this two-part shaft will be machined and not bought. Its diameter is reduced from 10 to 8 mm.

7.7.3 Bearings dimensioning

For the selection of the bearings, the design book [40] is used.

Bearings for the spline shaft

First, the radial and tangential forces F_r and F_t are identified. For the spline shaft, the position D has larger forces applied on and their expression is:

$$F_r = \sqrt{Y_D^2 + Z_D^2} \qquad\qquad F_t = X_D$$

These values can be recovered from Tab.7.6 and one can see that only Case 2 is considered for the selection of the bearings.

$$F_r = -25.96\,N \qquad\qquad F_t = 0\,N$$

For radial ball bearing, the relation 14.3 p.608 in the design book [40] is used. Because the ratio F_t/F_r is null, the pure radial equivalent load F_e is equal to F_r.

Then, the life in revolution L is computed based on the shaft angular velocity and the working hours. The design life was selected using table 14.4 p.609 of the design book [40] and set to 500 hours; instruments and apparatus for infrequent use.

$$\begin{aligned} L &= 8000 * 500 * 60 \\ &= 240.10^6\,rev \end{aligned}$$

Finally, the relation 14.5b p.609 of the design book [40] is used to compute the required value of the rated capacity C_{req}. For a reliability of 90%, the life adjustment reliability factor K_r is equal to 1, it was obtained from Figure 14.13 p.607. The application factor K_a is set to 1.2 (gearing-light impact applications) and obtained from table 14.3 p.609. For the last, the life corresponding to rated capacity L_R is set to 90.10^6 revolutions.

The required rated capacity is thus equal to:

$$\begin{aligned} C_{req} &= F_e K_a \left(\frac{L}{K_r L_R}\right)^{0.3} \\ &= 41.8\,N \end{aligned}$$

Bearings for the gimbal shaft

Following the same procedure, the expression of the radial and tangential forces are:

$$F_r = \sqrt{X_E^2 + Z_E^2} \qquad\qquad F_t = Y_E$$

These values can be recovered from Tab.7.6 and one can see that only Case 2 is considered for the selection of the bearings.

$$F_r = 28.82\,N \qquad\qquad F_t = 0\,N$$

For radial ball bearing, the relation 14.3 p.608 in the design book [40] is used. Because the ratio F_t/F_r is null, the pure radial equivalent load F_e is equal to F_r.

Then, the life in revolution L is computed based on the shaft angular velocity and the working hours. The design life was selected using table 14.4 p.609 of the design book [40] and set to 500 hours; instruments and apparatus for infrequent use. The angular speed was set to 3 rpm which is completely arbitrary as the gimbal does not rotate continuously.

$$\begin{aligned} L &= 3 * 500 * 60 \\ &= 90.10^3\,rev \end{aligned}$$

Finally, the relation 14.5b p.609 of the design book [40] is used to compute the required value of the rated capacity C_{req}. For a reliability of 90%, the life adjustment reliability factor K_r is equal to 1, it was obtained from Figure 14.13 p.607. The application factor K_a is set to 1.2 (gearing-light impact applications) and obtained from table 14.3 p.609. For the last, the life corresponding to rated capacity L_R is set to 90.10^6 revolutions.

The required rated capacity is thus equal to:

$$\begin{aligned} C_{req} &= F_e K_a \left(\frac{L}{K_r L_R}\right)^{0.3} \\ &= 4.35\,N \end{aligned}$$

Bearings selection

Based on the results, the bearings are selected in the catalog from Misumi and it was decided to use bearings designed with flange to reduce the distance between the two surfaces retaining it as depicted in Fig.7.13.

The same type of bearing with the reference SFL686ZZ will be used for the spline and gimbal shaft alignment.

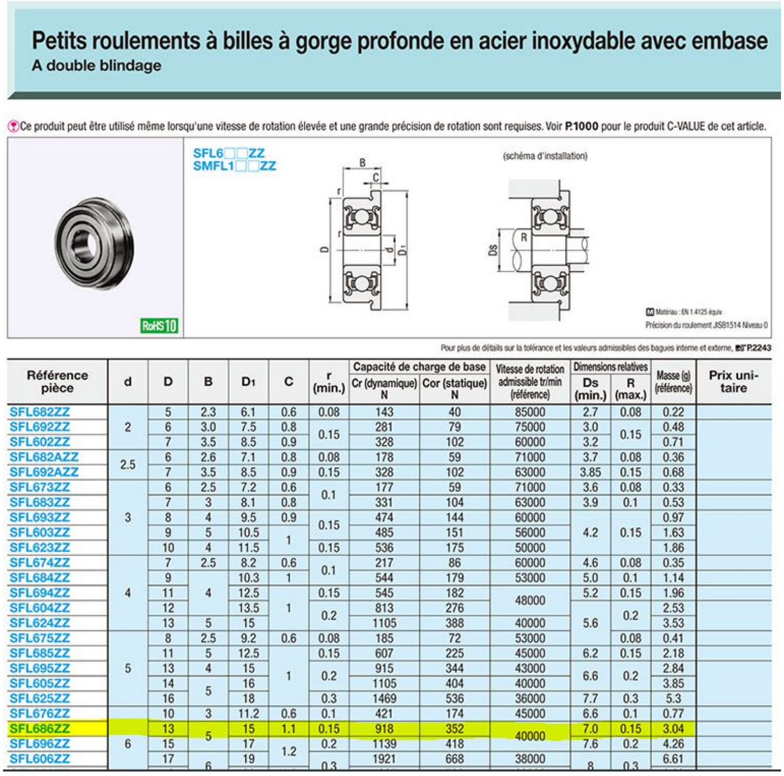

Référence pièce	d	D	B	D_1	C	r (min.)	Capacité de charge de base Cr (dynamique) N	Capacité de charge de base Cor (statique) N	Vitesse de rotation admissible tr/min (référence)	Dimensions relatives Ds (min.)	Dimensions relatives R (max.)	Masse (g) (référence)	Prix unitaire
SFL682ZZ		5	2.3	6.1	0.6	0.08	143	40	85000	2.7	0.08	0.22	
SFL692ZZ	2	6	3.0	7.5	0.8	0.15	281	79	75000	3.0	0.15	0.48	
SFL602ZZ		7	3.5	8.5	0.9		328	102	60000	3.2		0.71	
SFL682AZZ	2.5	6	2.6	7.1	0.8	0.08	178	59	71000	3.7	0.08	0.36	
SFL692AZZ		7	3.5	8.5	0.9	0.15	328	102	63000	3.85	0.15	0.68	
SFL673ZZ		6	2.5	7.2	0.6	0.1	177	59	71000	3.6	0.08	0.33	
SFL683ZZ		7	3	8.1	0.8		331	104	63000	3.9	0.1	0.53	
SFL693ZZ	3	8	4	9.5	0.9	0.15	474	144	60000			0.97	
SFL603ZZ		9	5	10.5	1		485	151	56000	4.2	0.15	1.63	
SFL623ZZ		10	4	11.5		0.15	536	175	50000			1.86	
SFL674ZZ		7	2.5	8.2	0.6	0.1	217	86	60000	4.6	0.08	0.35	
SFL684ZZ		9		10.3	1		544	179	53000	5.0	0.1	1.14	
SFL694ZZ	4	11	4	12.5		0.15	545	182	48000	5.2	0.15	1.96	
SFL604ZZ		12		13.5	1	0.2	813	276			0.2	2.53	
SFL624ZZ		13	5	15			1105	388	40000	5.6		3.53	
SFL675ZZ		8	2.5	9.2	0.6	0.08	185	72	53000		0.08	0.41	
SFL685ZZ		11	5	12.5		0.15	607	225	45000	6.2	0.15	2.18	
SFL695ZZ	5	13	4	15	1	0.2	915	344	43000	6.6	0.2	2.84	
SFL605ZZ		14	5	16			1105	404	40000			3.85	
SFL625ZZ		16		18		0.3	1469	536	36000	7.7	0.3	5.3	
SFL676ZZ		10	3	11.2	0.6	0.1	421	174	45000	6.6	0.1	0.77	
SFL686ZZ		13	5	15	1.1	0.15	918	352	40000	7.0	0.15	3.04	
SFL696ZZ	6	15		17	1.2	0.2	1139	418		7.6	0.2	4.26	
SFL606ZZ		17	6	19		0.3	1921	668	38000	8	0.3	6.61	

Figure 7.13: Screenshot from the catalogue of the selected type of bearings with the one chosen highlighted.

7.7.4 Actuators selection

Wheel actuator selection

The actuator needed for the flywheel should make the latter reach an angular velocity of 8000 rpm by applying a torque of $28mNm$ computed in Section 7.6.1. For such requirements, it is decided that the transmission ratio between the gears is equal to 1.

Therefore, by looking at the manufacturer catalogue, a brush DC motor is selected from Portescap. The latter has a maximal continuous torque of $33mNm$ and a maximal continuous speed of 10000 rpm. Also, a compatible magnetic encoder was selected from Portescap.

The datasheets of the selected motor, 25GST2R82-230E.1, and encoder, MR2, are depicted in Appendix Section 11.7.1.

Gimbal actuator selection

To actuate the gimbal, a servo or a stepper motor should be selected for their high torque and precise motions. For a gear ratio of 2 with the pinion on the actuator shaft, the motor should generate a torque of at least $120mNm$ as explained in Section 7.6.2.

From catalogs, a stepper from Trinamic is found. The latter has a stepper torque of $\pm100mNm$ up to 2000 pps, $600rad/s$, as depicted in Fig.7.15. This motor was selected even though the required torque was not reached because of dimension and supply constraints. Indeed, for an actuator generating a larger torque, the dimension goes from a square width of 28 mm to 42 mm which is considered too wide for the design of the CMG. Also, taking a bigger motor also increased the supply voltage to $24V$ and more. The specifications of the selected stepper are depicted in Fig.7.14.

Specifications	Parameter	Units	QSH2818	
			-32-07-006	-51-07-012
Rated Voltage	V_{RATED}	V	3.8	6.2
Rated Phase Current	I_{RMS_RATED}	A	0.67	0.67
Phase Resistance at 20°C	R_{COIL}	Ω	5.6	9.2
Phase Inductance (typ.)		mH	3.4	7.2
Holding Torque (typ.)		Ncm	6	12
		oz in	8.5	17.0
Detent Torque		Ncm		
Rotor Inertia		g cm²	9	18
Weight (Mass)		Kg	0.11	0.2
Insulation Class			B	B
Insulation Resistance		Ω	100M	100M
Dialectic Strength (for one minute)		VAC	500	500
Connection Wires		N°	4	4

Figure 7.14: Specification of the selected motor, QSH2818-51-07-012.

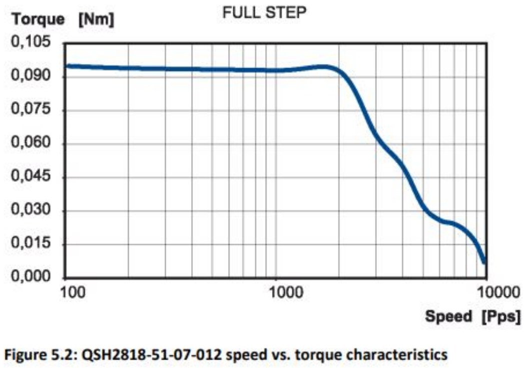

Figure 7.15: The torque generated in function of the speed for the selected motor.

7.7.5 Spur gears selections

Gears to actuate the spline shaft

With the motor and shaft selected, the bore diameters for the gear on the actuator is 3 mm and for the gear on the shaft 8 mm. Both gears should be fixed with a clamping screw and as small as possible.

For such characteristics, the choice of gear is limited and with the desire to have then as small as possible, they are found in the catalog of Misumi with a module of 0.5.

For the one on the shaft, with a bore diameter of 8 mm, the smallest pitch diameter is 26 mm for a width of 7 mm. The selected gear has for reference GEAB0.5-52-2-8 with an allowable transmission force of $0.22\,Nm$.

For the one on the actuator shaft, with a bore diameter of 3 mm, the tallest pitch diameter is 25 mm. The selected pinion has for reference GEABN0.5-50-2-B-3 with an allowable transmission force of $0.95\,Nm$. The ratio is thus 0.96 instead of 1.

The datasheet of the spur gears is available in Appendix Section 11.8.

From the datasheet of the DC motor in Appendix Section 11.7.1, the maximal load at 5 mm from the bearing is given, $12\,N$ radially and $68\,N$ axially. As spur gears are used, there will be no axial forces on the motor shaft. On the other hand, the radial force for Case 1 is computed from the torque transmitted with the following relations:

$$M_{Mx} = r_g Z_M \qquad\qquad Y_M = Z_M \tan\phi$$

With M_{Mx} the torque generated, r_g the radius of the gear, Z_M the tangential force acting on the gear, Y_M the radial force acting on the gear, and ϕ the pressure angle equal to 20 degrees. From the torque to accelerate the flywheel of $0.028\,Nm$, the tangential force Z_M is obtained with the gear radius and is equal to $2.15\,N$. The radial force is thus equal to

$$Y_M = 0.78\,N$$

There are no risks for the shaft of the actuator to break the bearings inside due to overloading.

Gears to actuate the gimbal shaft

With a bore diameter of 5 mm for the pinion on the stepper shaft and 8 mm for gear on the gimbal shaft, gears with a ratio of 2 must be found. By following the same procedure in the same catalog of gears, the gear and pinion for the torque transmission to the gimbal are selected.

The pinion reference is GEABN0.5-40-2-B-5 and has a pitch diameter of 20 mm with an allowable transmission force of $0.72\,Nm$.
The gear reference is GEABN0.5-80-2-B-8 and has a pitch diameter of 40 mm with an allowable transmission force of $1.65\,Nm$.

Unfortunately, the maximal load applied to the shaft was not given in the datasheet.

7.8 Summary

In this chapter, the different possible designs for the CMG and its fixation on the pendulum were studied through a morphological chart and the presentation of several concepts. Then, the selected design had its rotating part drawn.

From that, dimensions were assumed for the free-body and loading diagram analysis to obtain the different forces and momentums at stake.

With those parameters known, the design of the shafts, bearings, and gears was studied to finally select the actuators that will be used.

For the shaft actuating the wheel, a first static and then fatigue analysis was conducted to obtain the minimal shaft diameter equal to 4 mm. From catalogs, a commercial spline shaft with a flange was selected from Misumi.

For the shaft actuating the gimbal, only the static analysis was conducted as the shaft does not constantly rotate. The minimal diameter obtained for the shaft is equal to 3 mm. Because of the particular design of the shaft, it was decided that it will be machined.

For the bearings, the required rated capacity was computed for both shafts and are equal to $41.8\,N$ for the one holding the wheel and $4.35\,N$ for the one guiding the gimbal. Bearings with flange were selected from the catalog of Misumi for their compactness.

Then, based on the specifications of the dimensions and constraints, the motors were selected. To actuate the spline shaft, a brush DC motor from Portescap is used while for the gimbal, a stepper motor from Trinamic is found.

Finally, the gears to transmit the torque from the DC motor to the spline shaft and from the stepper to the gimbal shaft are obtained from the KHK gears catalog.

With the different dimensioned parts gathered in Tab.7.8, the complete drawing of the inverted pendulum and CMG system can be made on SolidWorks.

Part	Reference	Price [€]
Spline shaft	BSJMS8-60-F15-E5 -P6-Q6-FC5-A5	Unknown
Gimbal shaft	Machined	Unknown
Bearings	SFL686ZZ	4x 3.72
Flywheel actuator	25GST2R82-230E.1	191.07
Gimbal actuator	SH2818-51-07-012	45.15
Spur gear on the spline shaft	GEAB0.5-52-2-8	13.82
Spur gear on the DC motor shaft	GEABN0.5-50-2-B-3	13.61
Spur gear on the gimbal shaft	GEABN0.5-80-2-B-8	18.07
Spur pinion on the stepper shaft	GEABN0.5-40-2-B-5	12.22

Table 7.8: Summary of the selected part after the dimensioning of the latter with their reference and price if given.

Chapter 8

Technical drawing of the final solution

With all the selected parts in the previous chapter and the parameters obtained from dynamic scaling, the final design presented is drawn in SolidWorks. The result is depicted in Fig.8.1 and Fib.8.2 with parts that are bought designated by the red arrows and the ones machined by the blue arrows.

In the following chapter, a brief description of the parts bought that were not covered in the previous chapter is given then each machined part will be commented on. The plans of the parts machined are gathered in Appendix Section 11.9.

8.1 Commentary on the parts bought

A damping hinge is selected to support the pendulum and reproduce the viscous damping naturally present in the human body. This hinge is produced by Hanaya and its reference is 2000-0001-HNG R. The latter has a variable damping torque between 0.11 and 0.34 Nm. The plan of the latter is depicted in Appendix Section 11.8.1.

The angles are used to ensure the support but also the positioning of the pendulum fixations. They are bought from Misumi and three screw holes are made in them. The reference is $LRA3\_A40\_B33\_L30$ and the datasheet is depicted in Appendix Section 11.8.2.

Regarding the rest of the parts bought, they have already been covered in the previous chapter.

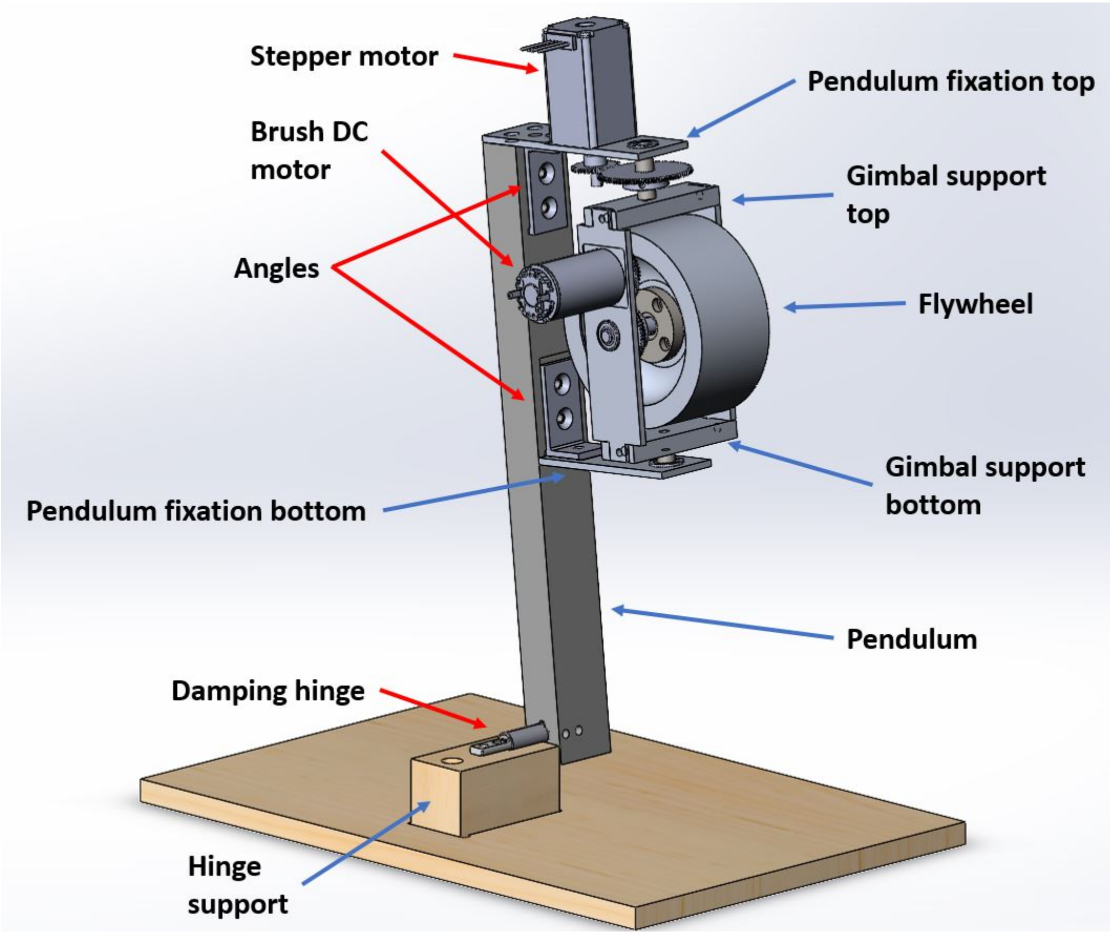

Figure 8.1: Assembly of the complete inverted pendulum mounted with a CMG. The parts identified on the drawing by a red arrow refers to bought materials and those designated by a blue arrow are those machined.

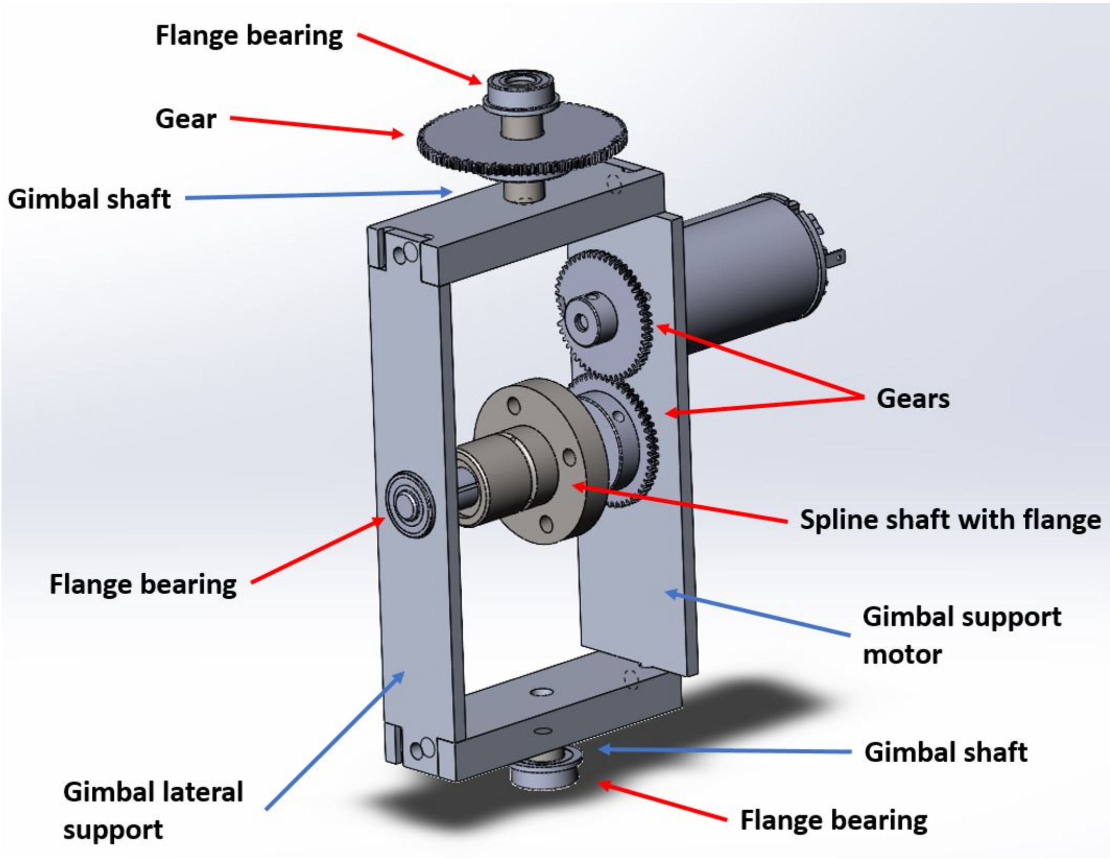

Figure 8.2: Assembly of the CMG without the flywheel. The parts identified on the drawing by a red arrow refers to bought materials and those designated by a blue arrow are those machined.

8.2 Commentary on the parts to machine

Hinge support

The hinge support as depicted in Fig.8.3 helps to support the hinge and the pendulum such that it is high enough for the edges of the beam not to touch the board. It is a basic block of wood as using raw material like aluminium for this part is considered as waste. The hinge is fixed with two screws and the non-rotating part is rested in the groove part of the block.

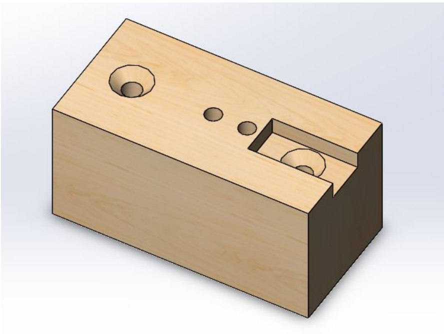

Figure 8.3: Hinge support

Pendulum

The pendulum is an aluminium beam of 15x30x270 mm and is supported by the hinge place in the hole and screws maintain it in place. Boring is made to align and place the angles. For those reasons, the beam needs to be machined.

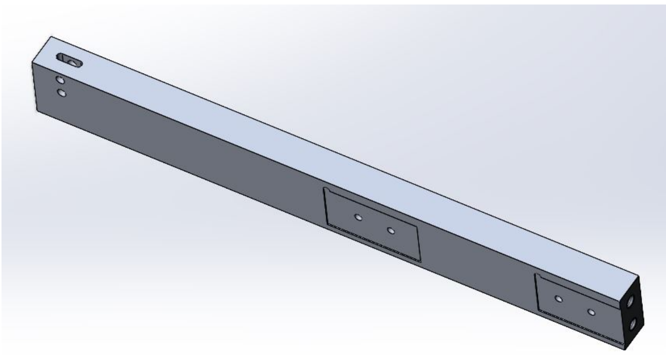

Figure 8.4: Pendulum

Pendulum fixation bottom

This part has for purpose to hold the CMG and maintain the gimbal axis aligned with the bearing. For that, it is better to machine it for enhanced accuracy on a 3 mm thick plate.

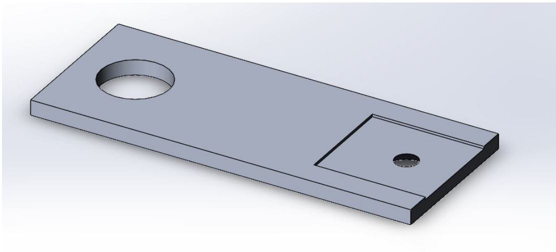

Figure 8.5: Pendulum fixation bottom

Pendulum fixation top

This part has the same purpose as the one above but also to hold the stepper motor actuating the gimbal with gears. For the required precision, it is better to machine it on a 3 mm thick plate.

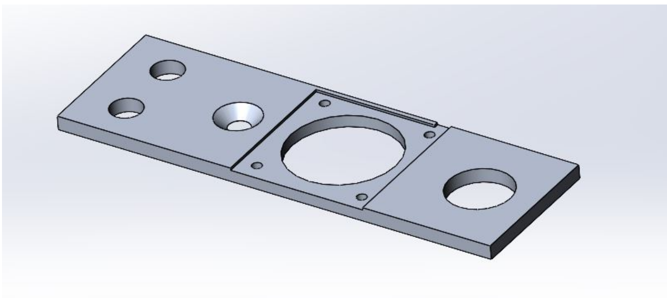

Figure 8.6: Pendulum fixation top

Flywheel

The main part of the CMG is machined as no manufacturer was found to make it. The wheel 40 mm wide has an outer diameter of 86 mm and an inner one of 66 mm. The four holes and the large bore diameter are for the wheel to be fixed on the flange of the spline shaft.

The reason for the inner corner to be rounded is to prevent unbalance due to fluid and materials caught on the lip [42].

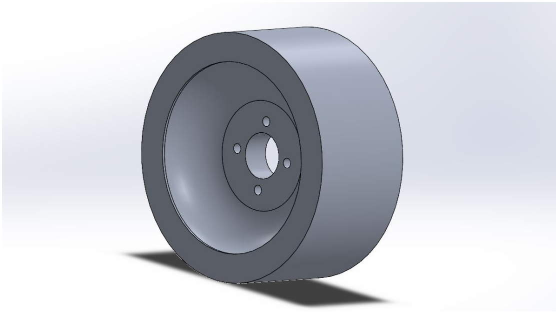

Figure 8.7: Flywheel

Gimbal support top

This part has the role of holding in place the gimbal together and is directly linked to the gimbal shaft. Because of its complexity, the hole to maintain the shaft in place and transfer efficiently the torque and the screw holes on the side, the part should be machined on a 8 mm thick plate.

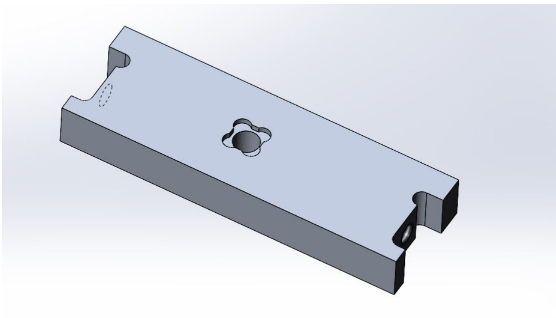

Figure 8.8: Gimbal support top

Gimbal support bottom

This part has the same role as the one above but does not need to be locked on the gimbal shaft as no torque is transmitted to it. Because of its complexity, no manufacturer was found to produce the part therefore it should be machined on a 8 mm thick plate.

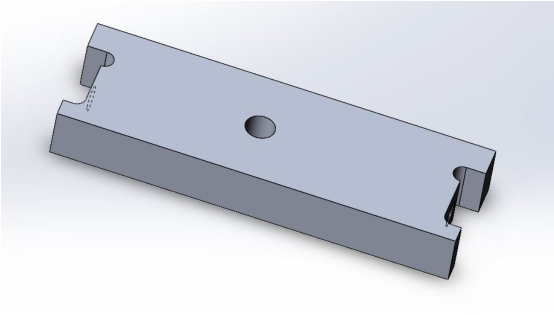

Figure 8.9: Gimbal support bottom

Gimbal lateral support

The gimbal lateral support plays a crucial role in aligning the spline shaft and also to the others gimbal supports. The 3 mm plate needs then to be machined.

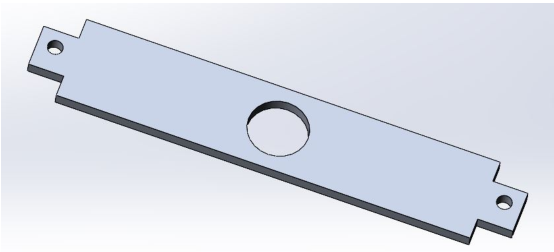

Figure 8.10: Gimbal lateral support

Gimbal support motor

This part has the same role as the one above but also holds the DC motor in place. With the required accuracy for alignment and placement, the part is machined on a 3 mm thick plate.

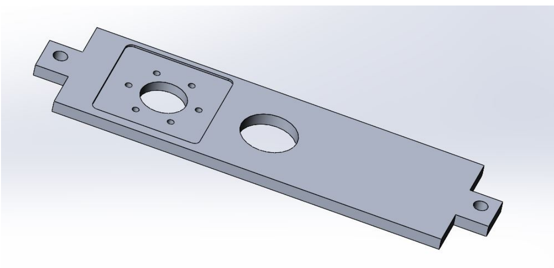

Figure 8.11: Gimbal support motor

Gimbal shaft

The gimbal shaft is a two-part rod of 8 mm that is clamped to the gimbal support top and bottom with a screw.

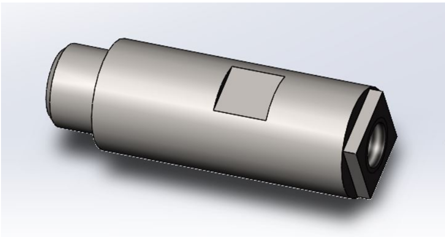

Figure 8.12: Gimbal shaft top

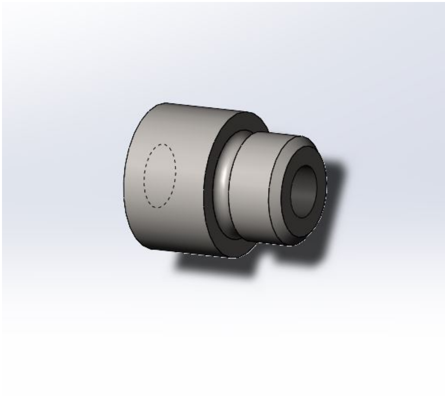

Figure 8.13: Gimbal shaft bottom

Chapter 9

Discussion of the results

The objective of this master thesis was to design a down-scaled inverted pendulum weighing 1 kg and from the 3D drawing on Solidworks depicted in Fig.9.1, one can see that the objective is met. Indeed, the pendulum weight is just above 1 kg and with its center of gravity at 24 cm as wanted from the dynamic scaling of the big pendulum.

From the control, it was shown that CMGs could be promising in the balance assistance field with their high torque generation. Also, because the work of this master thesis stopped at the mechanical design of the solution, no comparison between the model and its real capability can be made.

From the mechanical point of view, one can directly see from the solution the size of the CMG system compare to the height of the pendulum. I believe it is mostly due to the fact that it is the CMG that contributes the most in the overall weight of the system. Therefore, if the scale is increased, realistic proportions between the CMG system and the height of the center of mass should be observed.

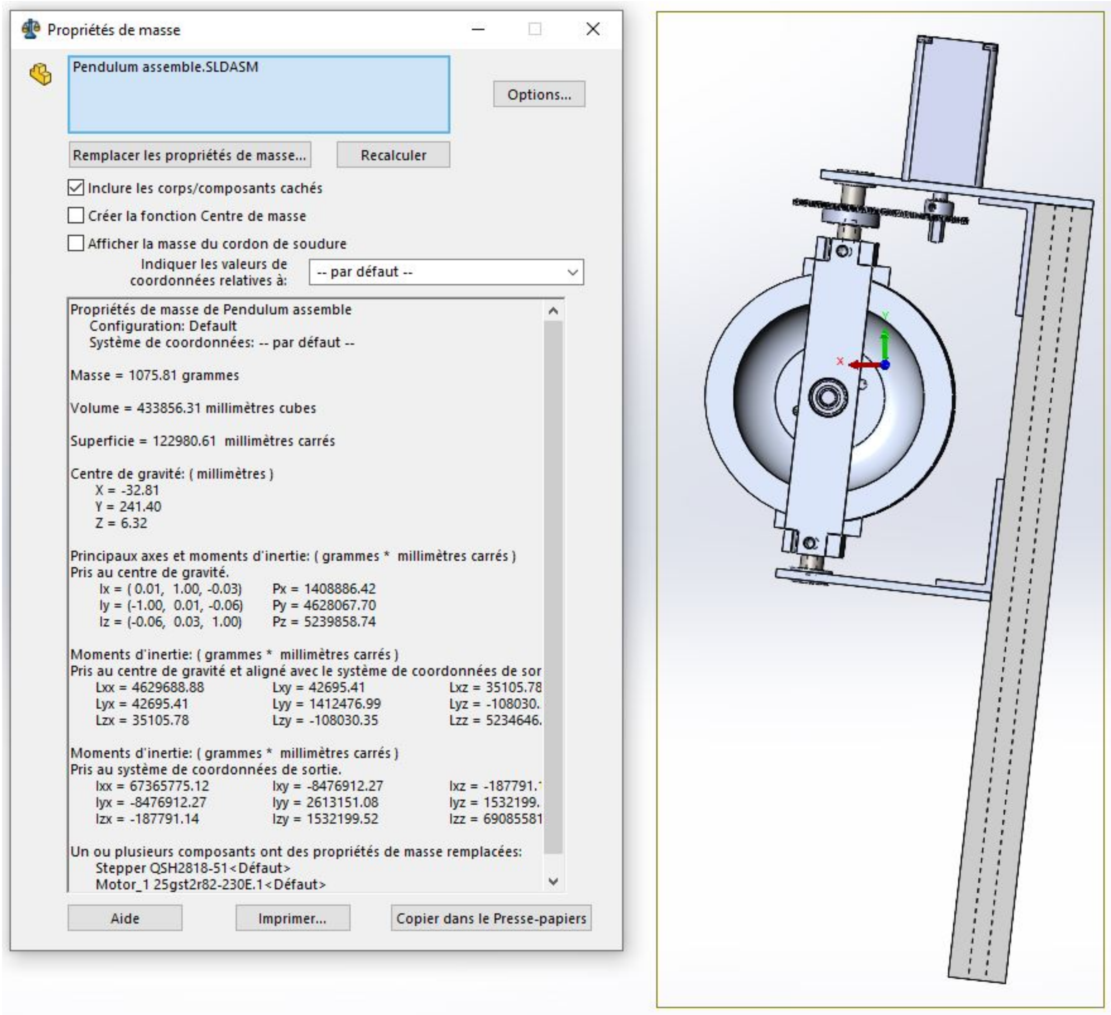

Figure 9.1: Image of the inverted pendulum mounted with a CMG with its mass properties displayed.

Chapter 10

Conclusion

The CMG technology has shown through this work it capability in assisting the balance of an inverted pendulum through numerical simulation. A complete mechanical design was made so that it is ready to assemble and physical measurements can be made.

Nevertheless, using a single CMG is costly in weight and space as a single wheel must generate the torque. Configuration of CMG said scissor-pair, the wheels are rotation in the opposite direction, are particularly interesting as they cancel each other their non effective torque, the sine part. In this case the pendulum had only one degree of freedom but once the system is transferred to a system having more than one DoF, this sine part will be added perturbation to the system. Therefore, by selecting the right configuration for both CMG, the torque generated will be only on one axis.

Moreover, when three or more CMG are used in a specific configuration, an algorithm called "Null motion" can be implemented. The drawback of the potential field algorithm was the added time for the system to reach its equilibrium position. This was cause by the fact that the gimbal was slowly rotating back which was generating a torque knocking off the pendulum. The null motion algorithm is able to find a way for the CMGs to reach a desired angular position without generate a single torque on the system. They all cancel each others torques.

Because the system aims at proving that the concept works, the design of the CMG was kept as simple as possible which made it bulky. If the technology should be integrated in a more end-design, some improvement could be made by integrating the motor actuating the wheel inside the gimbal. The same goes for the stepper actuating the gimbal, a better configuration could be found for the CMG to take less space. Finally, the wheel angular velocity should be increased as highly as possible to reduced the size of the latter.

Je souhaterais remercier les personnes qui m'ont accompagné dans la réalisation de ce travail de fin d'études:

Ma famille qui m'a soutenu pendant toute ma période académique et particulièrement pendant la réalisationde ce mémoire.

Mon promoteur, Monsieur Ronsse pour son assistance, son soutient et ses conseils tout au long de mon master.

Mes lecteurs pour le temps qu'ils accorderont à la lecture.

Chapter 11

Appendix

11.1 Complete derivation of the CMG dynamic equation

The different frames defined to solve the problem are:

- N the reference frame fixed on the ground $\{\hat{n}_u, \hat{n}_v, \hat{n}_w\}$
- B the pendulum reference frame $\{\hat{b}_u, \hat{b}_v, \hat{b}_w\}$
- G the gimbal reference frame $\{\hat{g}_s, \hat{g}_t, \hat{g}_g\}$
- W the wheel reference frame $\{\hat{w}_s, \hat{w}_t, \hat{w}_g\}$

The different variables defined to solve the problem are:

- ϕ, $\dot{\phi}$ the tilt angle and the angular velocity of the inverted pendulum respectively w.r.t the reference frame N
- γ, $\dot{\gamma}$ the tilt angle and the angular velocity of the gimbal respectively w.r.t the reference frame B
- Ω the angular velocity of the wheel w.r.t the reference frame G
- m the body mass
- l the distance from the hinge to the center of mass

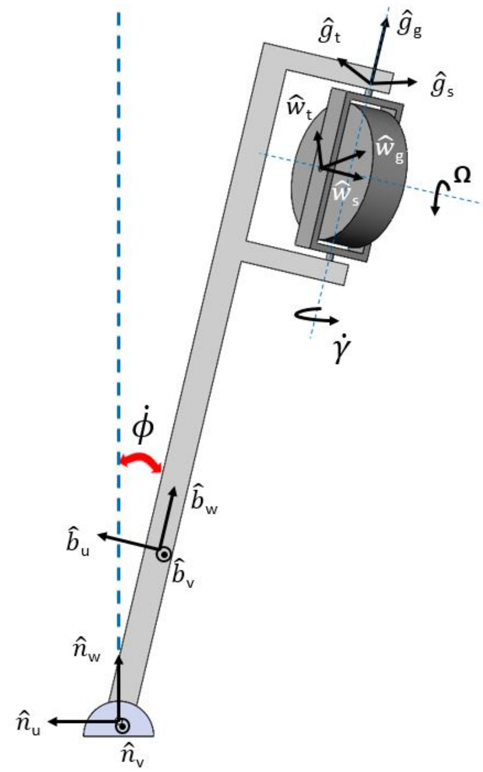

Figure 11.1: Lookalike illustration of what is to be prototyped, an inverted pendulum mounted with a CMG and its degrees of freedom. On this illustration, the different reference frames and variables (state, control or parametric) are represented.

Thus to obtain the torque, the angular moment of the CMG defined as the product of the inertia matrix and the angular velocity must be computed first.

The angular velocity vectors of the different frames can be defined with respect to the parent frame:

$$\boldsymbol{\omega}_{W/G} = \Omega\,\hat{\mathbf{g}}_{\mathbf{s}} \qquad \boldsymbol{\omega}_{G/B} = \dot{\gamma}\,\hat{\mathbf{g}}_{\mathbf{g}} \qquad \boldsymbol{\omega}_{B/N} = \dot{\phi}\,\hat{\mathbf{b}}_{\mathbf{v}} \tag{11.1}$$

and the inertia matrices of the gimbal and wheel in their respective frame:

$$[I_G] = {}^{G}[I_G] = diag(I_{G_s}, I_{G_t}, I_{G_g}) \quad [I_W] = {}^{W}[I_W] = diag(I_{W_s}, I_{W_t}, I_{W_g}) \tag{11.2}$$

The inertia matrices are diagonal because the coordinate frames G and W are aligned with the principal body frame axes. Also, the inertia parameters I_{W_t} and I_{W_g} are equal because of the symmetric geometry of the wheel about the axis $\hat{g}_s$.

Therefore, the inertia matrix of the wheel in the reference frame W is unchanged if expressed in the reference frame G, ${}^{W}[I_W] = {}^{G}[I_W]$.

The axis of the frame G expressed in frame B can be written where γ_0 is the initial gimbal angle.

$$\begin{aligned}
\hat{\mathbf{g}}_{\mathbf{s}(t)} &= \cos\left(\gamma_{(t)} - \gamma_0\right)\hat{\mathbf{g}}_{\mathbf{s}(t_0)} + \sin\left(\gamma_{(t)} - \gamma_0\right)\hat{\mathbf{g}}_{\mathbf{t}(t_0)} \\
\hat{\mathbf{g}}_{\mathbf{t}(t)} &= -\sin\left(\gamma_{(t)} - \gamma_0\right)\hat{\mathbf{g}}_{\mathbf{s}(t_0)} + \cos\left(\gamma_{(t)} - \gamma_0\right)\hat{\mathbf{g}}_{\mathbf{t}(t_0)} \\
\hat{\mathbf{g}}_{\mathbf{g}(t)} &= \hat{\mathbf{g}}_{\mathbf{g}(t_0)}
\end{aligned} \tag{11.3}$$

From those equations, the rotation matrix $[BG]$ to rotate from the frame G to B can be written as $[\hat{\mathbf{g}}_{\mathbf{s}}\,\hat{\mathbf{g}}_{\mathbf{t}}\,\hat{\mathbf{g}}_{\mathbf{g}}]$. With this relation, the inertia tensors defined in Eq.11.2 can be expressed in the frame B.

$$\begin{aligned}
{}^{B}[I_G] = [BG]\,{}^{G}[I_G]\,[BG]^T &= I_{G_s}\hat{\mathbf{g}}_{\mathbf{s}}\hat{\mathbf{g}}_{\mathbf{s}}^T + I_{G_t}\hat{\mathbf{g}}_{\mathbf{t}}\hat{\mathbf{g}}_{\mathbf{t}}^T + I_{G_g}\hat{\mathbf{g}}_{\mathbf{g}}\hat{\mathbf{g}}_{\mathbf{g}}^T \\
{}^{B}[I_W] = [BG]\,{}^{G}[I_W]\,[BG]^T &= I_{W_s}\hat{\mathbf{g}}_{\mathbf{s}}\hat{\mathbf{g}}_{\mathbf{s}}^T + I_{W_t}\hat{\mathbf{g}}_{\mathbf{t}}\hat{\mathbf{g}}_{\mathbf{t}}^T + I_{W_t}\hat{\mathbf{g}}_{\mathbf{g}}\hat{\mathbf{g}}_{\mathbf{g}}^T
\end{aligned} \tag{11.4}$$

The angular momentum of the inverted pendulum about its center of mass can be decomposed as:

$$\mathbf{H}_{CMG} = \mathbf{H}_G + \mathbf{H}_W \qquad\qquad \mathbf{H} = [I]\,\boldsymbol{\omega} \tag{11.5}$$

where $\mathbf{H}_G$ is the angular momentum of the gimbal and $\mathbf{H}_W$ is the angular momentum of the wheel. The angular momentum is defined as the product of the inertia matrix with the angular velocity of the body.

The different angular momentum can thus be computed, first for $\mathbf{H}_G$ and to be expressed in the reference frame N, the angular velocity of the gimbal in the latter frame is the sum of the ones of the gimbal with respect to the pendulum and of the pendulum with respect to the frame N.

$$\begin{aligned}
\mathbf{H}_G &= [I_G]\,\boldsymbol{\omega}_{G/N} && \text{with} \qquad \boldsymbol{\omega}_{G/N} = \boldsymbol{\omega}_{G/B} + \boldsymbol{\omega}_{B/N} \\
&= \left(I_{G_s}\hat{\mathbf{g}}_{\mathbf{s}}\hat{\mathbf{g}}_{\mathbf{s}}^T + I_{G_t}\hat{\mathbf{g}}_{\mathbf{t}}\hat{\mathbf{g}}_{\mathbf{t}}^T + I_{G_g}\hat{\mathbf{g}}_{\mathbf{g}}\hat{\mathbf{g}}_{\mathbf{g}}^T\right)\boldsymbol{\omega}_{B/N} + I_{G_g}\dot{\gamma}\,\hat{\mathbf{g}}_{\mathbf{g}} && \text{Using Eq.11.1-11.4}
\end{aligned}$$

To simplify the notation, the projection of $\boldsymbol{\omega}_{W/B}$ onto the G frame can be written as:

$$\begin{aligned}
\omega_s &= \hat{\mathbf{g}}_s^T\,\boldsymbol{\omega}_{B/N} \\
\omega_t &= \hat{\mathbf{g}}_t^T\,\boldsymbol{\omega}_{B/N} \\
\omega_g &= \hat{\mathbf{g}}_g^T\,\boldsymbol{\omega}_{B/N}
\end{aligned} \tag{11.6}$$

And thus $\mathbf{H}_G$ becomes

$$\mathbf{H}_G = I_{G_s}\omega_s\hat{\mathbf{g}}_\mathbf{s} + I_{G_t}\omega_t\hat{\mathbf{g}}_\mathbf{t} + I_{G_g}\left(\omega_g + \dot{\gamma}\right)\hat{\mathbf{g}}_\mathbf{g} \tag{11.7}$$

In the same manner $\mathbf{H}_W$ is computed

$$\begin{aligned}
\mathbf{H}_W &= [I_W]\,\boldsymbol{\omega}_{W/N} && \text{with} \quad \boldsymbol{\omega}_{W/N} = \boldsymbol{\omega}_{W/G} + \boldsymbol{\omega}_{G/B} + \boldsymbol{\omega}_{B/N} \\
&= I_{W_s}\left(\omega_s + \Omega\right)\hat{\mathbf{g}}_\mathbf{s} + I_{W_t}\omega_t\hat{\mathbf{g}}_\mathbf{t} + I_{W_t}\left(\omega_g + \dot{\gamma}\right)\hat{\mathbf{g}}_\mathbf{g} && \text{Using Eq.11.1-11.4}
\end{aligned} \tag{11.8}$$

In the further demonstrations, $\boldsymbol{\omega}_{B/N}$ will be written as $\boldsymbol{\omega}$ and it can also be defined in the gimbal frame G as

$${}^{G}\boldsymbol{\omega} = \omega_s\hat{\mathbf{g}}_\mathbf{s} + \omega_t\hat{\mathbf{g}}_\mathbf{t} + \omega_g\hat{\mathbf{g}}_\mathbf{g} \tag{11.9}$$

With the Eq.11.7-11.8 obtained, $\dot{H}$ can be computed and to do that the inertial derivatives of the different vectors $\{\hat{\mathbf{g}}_\mathbf{s}, \hat{\mathbf{g}}_\mathbf{t}, \hat{\mathbf{g}}_\mathbf{g}\}$ and those of the body angular velocity in the G frame $\{\omega_s, \omega_t, \omega_g\}$ are first obtained.

For the first set, the transport theorem is used and states that

> *Let N and B be two frames with a relative angular velocity vector of $\boldsymbol{\omega}_{B/N}$, and let $\boldsymbol{r}$ be a generic vector; then the derivative of $\boldsymbol{r}$ in the N frame can be related to the derivative of $\boldsymbol{r}$ in the B frame as* [21]
>
> $$\frac{{}^{N}d}{dt}(r) = \frac{{}^{B}d}{dt}(r) + \boldsymbol{\omega}_{B/N} \times r \tag{11.10}$$

Then, using Eq.11.10 with Eq.11.3-11.9

$$\begin{aligned}
\dot{\hat{\mathbf{g}}}_\mathbf{s} &= \frac{{}^{B}d}{dt}(\hat{\mathbf{g}}_\mathbf{s}) + \boldsymbol{\omega} \times \hat{\mathbf{g}}_\mathbf{s} & \dot{\hat{\mathbf{g}}}_\mathbf{t} &= \frac{{}^{B}d}{dt}(\hat{\mathbf{g}}_\mathbf{t}) + \boldsymbol{\omega} \times \hat{\mathbf{g}}_\mathbf{t} & \dot{\hat{\mathbf{g}}}_\mathbf{g} &= \frac{{}^{B}d}{dt}(\hat{\mathbf{g}}_\mathbf{g}) + \boldsymbol{\omega} \times \hat{\mathbf{g}}_\mathbf{g} \\
&= \dot{\gamma}\hat{\mathbf{g}}_\mathbf{t} + \omega_g\hat{\mathbf{g}}_\mathbf{t} - \omega_t\hat{\mathbf{g}}_\mathbf{g} & &= -\dot{\gamma}\hat{\mathbf{g}}_\mathbf{s} - \omega_g\hat{\mathbf{g}}_\mathbf{s} + \omega_s\hat{\mathbf{g}}_\mathbf{g} & &= 0 + \omega_t\hat{\mathbf{g}}_\mathbf{s} - \omega_s\hat{\mathbf{g}}_\mathbf{t} \\
&= (\dot{\gamma} + \omega_g)\hat{\mathbf{g}}_\mathbf{t} - \omega_t\hat{\mathbf{g}}_\mathbf{g} & &= -(\dot{\gamma} + \omega_g)\hat{\mathbf{g}}_\mathbf{s} + \omega_s\hat{\mathbf{g}}_\mathbf{g} & &= \omega_t\hat{\mathbf{g}}_\mathbf{s} - \omega_s\hat{\mathbf{g}}_\mathbf{t}
\end{aligned} \tag{11.11}$$

Whereas for the inertial derivative of the body angular velocities in the G frame, the Eq.11.6 is derived using Eq.11.1-11.11 are used.

$$\begin{aligned}
\dot{\omega}_s &= \dot{\hat{\mathbf{g}}}_s^T\boldsymbol{\omega} + \hat{\mathbf{g}}_s^T\dot{\boldsymbol{\omega}} & \dot{\omega}_t &= \dot{\hat{\mathbf{g}}}_t^T\boldsymbol{\omega} + \hat{\mathbf{g}}_t^T\dot{\boldsymbol{\omega}} & \dot{\omega}_g &= \dot{\hat{\mathbf{g}}}_g^T\boldsymbol{\omega} + \hat{\mathbf{g}}_g^T\dot{\boldsymbol{\omega}} \\
&= (\dot{\gamma} + \omega_g)\omega_t - \omega_t\omega_g + \hat{\mathbf{g}}_s^T\dot{\boldsymbol{\omega}} & &= -(\dot{\gamma} + \omega_g)\omega_s + \omega_s\omega_g + \hat{\mathbf{g}}_t^T\dot{\boldsymbol{\omega}} & &= \omega_t\omega_s - \omega_s\omega_t + \hat{\mathbf{g}}_g^T\dot{\boldsymbol{\omega}} \\
&= \dot{\gamma}\omega_t + \hat{\mathbf{g}}_s^T\dot{\boldsymbol{\omega}} & &= -\dot{\gamma}\omega_s + \hat{\mathbf{g}}_t^T\dot{\boldsymbol{\omega}} & &= \hat{\mathbf{g}}_g^T\dot{\boldsymbol{\omega}}
\end{aligned} \tag{11.12}$$

The inertial derivative of the angular momentum of the gimbal Eq.11.7 and of the wheel Eq.11.8 can now be computed using the results of Eq.11.11-11.12.

$$
\begin{aligned}
\dot{\mathbf{H}}_G &= I_{G_s}\left(\dot{\omega}_s\hat{\mathbf{g}}_\mathbf{s} + \omega_s\dot{\hat{\mathbf{g}}}_\mathbf{s}\right) + I_{G_t}\left(\dot{\omega}_t\hat{\mathbf{g}}_\mathbf{t} + \omega_t\dot{\hat{\mathbf{g}}}_\mathbf{t}\right) + I_{G_g}\left[\left(\dot{\omega}_g + \ddot{\gamma}\right)\hat{\mathbf{g}}_\mathbf{g} + \left(\omega_g + \dot{\gamma}\right)\dot{\hat{\mathbf{g}}}_\mathbf{g}\right] \\
&= I_{G_s}\left[\left(\dot{\gamma}\omega_t + \hat{\mathbf{g}}_s^T\dot{\boldsymbol{\omega}}\right)\hat{\mathbf{g}}_\mathbf{s} + \omega_s\left(\dot{\gamma} + \omega_g\right)\hat{\mathbf{g}}_\mathbf{t} - \omega_s\omega_t\hat{\mathbf{g}}_\mathbf{g}\right] \\
&\quad + I_{G_t}\left[\left(-\dot{\gamma}\omega_s + \hat{\mathbf{g}}_t^T\dot{\boldsymbol{\omega}}\right)\hat{\mathbf{g}}_\mathbf{t} - \omega_t\left(\dot{\gamma} + \omega_g\right)\hat{\mathbf{g}}_\mathbf{s} + \omega_s\omega_t\hat{\mathbf{g}}_\mathbf{g}\right] \\
&\quad + I_{G_g}\left[\left(\hat{\mathbf{g}}_g^T\dot{\boldsymbol{\omega}} + \ddot{\gamma}\right)\hat{\mathbf{g}}_\mathbf{g} + \left(\omega_g + \dot{\gamma}\right)\left(\omega_t\hat{\mathbf{g}}_\mathbf{s} - \omega_s\hat{\mathbf{g}}_\mathbf{t}\right)\right] \\
&= \hat{\mathbf{g}}_\mathbf{s}\left[I_{G_s}\left(\dot{\gamma}\omega_t + \hat{\mathbf{g}}_s^T\dot{\boldsymbol{\omega}}\right) - I_{G_t}\omega_t\left(\dot{\gamma} + \omega_g\right) + I_{G_g}\omega_t\left(\omega_g + \dot{\gamma}\right)\right] \\
&\quad + \hat{\mathbf{g}}_\mathbf{t}\left[I_{G_s}\omega_s\left(\dot{\gamma} + \omega_g\right) + I_{G_t}\left(\hat{\mathbf{g}}_t^T\dot{\boldsymbol{\omega}} - \dot{\gamma}\omega_s\right) - I_{G_g}\omega_s\left(\omega_g + \dot{\gamma}\right)\right] \\
&\quad + \hat{\mathbf{g}}_\mathbf{g}\left[-I_{G_s}\omega_s\omega_t + I_{G_t}\omega_s\omega_t + I_{G_g}\left(\hat{\mathbf{g}}_g^T\dot{\boldsymbol{\omega}} + \ddot{\gamma}\right)\right] \\
&= \hat{\mathbf{g}}_\mathbf{s}\left[\left(I_{G_s} - I_{G_t} + I_{G_g}\right)\dot{\gamma}\omega_t + I_{G_s}\hat{\mathbf{g}}_s^T\dot{\boldsymbol{\omega}} - \omega_t\omega_g\left(I_{G_t} - I_{G_g}\right)\right] \\
&\quad + \hat{\mathbf{g}}_\mathbf{t}\left[\left(I_{G_s} - I_{G_t} - I_{G_g}\right)\dot{\gamma}\omega_s + I_{G_t}\hat{\mathbf{g}}_t^T\dot{\boldsymbol{\omega}} + \omega_s\omega_g\left(I_{G_s} - I_{G_g}\right)\right] \\
&\quad + \hat{\mathbf{g}}_\mathbf{g}\left[I_{G_g}\left(\hat{\mathbf{g}}_g^T\dot{\boldsymbol{\omega}} + \ddot{\gamma}\right) + \omega_s\omega_t\left(I_{G_t} - I_{G_s}\right)\right]
\end{aligned}
$$

And for the wheel,

$$
\begin{aligned}
\dot{\mathbf{H}}_W &= I_{W_s}\left[\left(\dot{\omega}_s + \dot{\Omega}\right)\hat{\mathbf{g}}_\mathbf{s} + \left(\omega_s + \Omega\right)\dot{\hat{\mathbf{g}}}_\mathbf{s}\right] + I_{W_t}\left(\dot{\omega}_t\hat{\mathbf{g}}_\mathbf{t} + \omega_t\dot{\hat{\mathbf{g}}}_\mathbf{t}\right) + I_{W_t}\left[\left(\dot{\omega}_g + \ddot{\gamma}\right)\hat{\mathbf{g}}_\mathbf{g} + \left(\omega_g + \dot{\gamma}\right)\dot{\hat{\mathbf{g}}}_\mathbf{g}\right] \\
&= I_{W_s}\left[\left(\dot{\gamma}\omega_t + \hat{\mathbf{g}}_s^T\dot{\boldsymbol{\omega}} + \dot{\Omega}\right)\hat{\mathbf{g}}_\mathbf{s} + \left(\omega_s + \Omega\right)\left(\dot{\gamma} + \omega_g\right)\hat{\mathbf{g}}_\mathbf{t} - \left(\omega_s + \Omega\right)\omega_t\hat{\mathbf{g}}_\mathbf{g}\right] \\
&\quad + I_{W_t}\left[\left(-\dot{\gamma}\omega_s + \hat{\mathbf{g}}_t^T\dot{\boldsymbol{\omega}}\right)\hat{\mathbf{g}}_\mathbf{t} - \omega_t(\dot{\gamma} + \omega_g)\hat{\mathbf{g}}_\mathbf{s} + \omega_t\omega_s\hat{\mathbf{g}}_\mathbf{g}\right] \\
&\quad + I_{W_t}\left[\left(\hat{\mathbf{g}}_g^T\dot{\boldsymbol{\omega}} + \ddot{\gamma}\right)\hat{\mathbf{g}}_\mathbf{g} + \left(\omega_g + \dot{\gamma}\right)\omega_t\hat{\mathbf{g}}_\mathbf{s} - \left(\omega_g + \dot{\gamma}\right)\omega_s\hat{\mathbf{g}}_\mathbf{t}\right] \\
&= \hat{\mathbf{g}}_\mathbf{s}\left[I_{W_s}\left(\dot{\gamma}\omega_t + \hat{\mathbf{g}}_s^T\dot{\boldsymbol{\omega}} + \dot{\Omega}\right) - I_{W_t}\omega_t(\dot{\gamma} + \omega_g) + I_{W_t}\omega_t\left(\omega_g + \dot{\gamma}\right)\right] \\
&\quad + \hat{\mathbf{g}}_\mathbf{t}\left[I_{W_s}\left(\omega_s + \Omega\right)\left(\dot{\gamma} + \omega_g\right) + I_{W_t}\left(-\dot{\gamma}\omega_s + \hat{\mathbf{g}}_t^T\dot{\boldsymbol{\omega}}\right) - I_{W_t}\omega_s\left(\omega_g + \dot{\gamma}\right)\right] \\
&\quad + \hat{\mathbf{g}}_\mathbf{g}\left[-I_{W_s}\omega_t\left(\omega_s + \Omega\right) + I_{W_t}\omega_s\omega_t + I_{W_t}\left(\hat{\mathbf{g}}_g^T\dot{\boldsymbol{\omega}} + \ddot{\gamma}\right)\right] \\
&= \hat{\mathbf{g}}_\mathbf{s}\left[I_{W_s}\left(\dot{\gamma}\omega_t + \hat{\mathbf{g}}_s^T\dot{\boldsymbol{\omega}} + \dot{\Omega}\right)\right] \\
&\quad + \hat{\mathbf{g}}_\mathbf{t}\left[\left(I_{W_s} - 2I_{W_t}\right)\dot{\gamma}\omega_s + I_{W_t}\hat{\mathbf{g}}_t^T\dot{\boldsymbol{\omega}} + \left(I_{W_s} - I_{W_t}\right)\omega_s\omega_g + I_{W_s}\Omega\left(\omega_g + \dot{\gamma}\right)\right] \\
&\quad + \hat{\mathbf{g}}_\mathbf{g}\left[\left(I_{W_t} - I_{W_s}\right)\omega_s\omega_t - I_{W_s}\omega_t\Omega + I_{W_t}\left(\hat{\mathbf{g}}_g^T\dot{\boldsymbol{\omega}} + \ddot{\gamma}\right)\right]
\end{aligned}
\tag{11.13}
$$

Therefore, by summing $\dot{\mathbf{H}}_G$ and $\dot{\mathbf{H}}_W$ the rate of change of angular momentum of the CMG system is obtained which is equal to the external torque applied.

$$\dot{\mathbf{H}}_{CMG} = \dot{\mathbf{H}}_W \ + \dot{\mathbf{H}}_G$$

And to simplify the equations, the CMG system's inertial matrix J is defined as the sum of the inertial matrices of the gimbal and the wheel.

$$^G[J] = [I_G] + [I_W] = diag(J_s, J_t, J_g)$$

As the equations are long and to make it more readable, $\dot{\mathbf{H}}$ will be solved axis by axis.

$$\begin{aligned}
\dot{\mathbf{H}}\hat{\mathbf{g}}_{\mathbf{s}} &= I_{W_s}\left(\dot{\gamma}\omega_t + \hat{\mathbf{g}}_s^T\,\dot{\boldsymbol{\omega}} + \dot{\Omega}\right) \\
&\quad + \left(I_{G_s} - I_{G_t} + I_{G_g}\right)\dot{\gamma}\omega_t + I_{G_s}\hat{\mathbf{g}}_s^T\,\dot{\boldsymbol{\omega}} - \omega_t\omega_g\left(I_{G_t} - I_{G_g}\right) \\
&= I_{W_s}\dot{\Omega} + \left(J_s - I_{G_t} + I_{G_g}\right)\dot{\gamma}\omega_t + J_s\hat{\mathbf{g}}_s^T\,\dot{\boldsymbol{\omega}} + \omega_t\omega_g\left(I_{G_g} - I_{G_t}\right)
\end{aligned} \tag{11.14}$$

$$\begin{aligned}
\dot{\mathbf{H}}\hat{\mathbf{g}}_{\mathbf{t}} &= \left(I_{W_s} - 2I_{W_t}\right)\dot{\gamma}\omega_s + I_{W_t}\hat{\mathbf{g}}_t^T\,\dot{\boldsymbol{\omega}} + \left(I_{W_s} - I_{W_t}\right)\omega_s\omega_g + I_{W_s}\Omega\left(\omega_g + \dot{\gamma}\right) \\
&\quad + \left(I_{G_s} - I_{G_t} - I_{G_g}\right)\dot{\gamma}\omega_s + I_{G_t}\hat{\mathbf{g}}_t^T\,\dot{\boldsymbol{\omega}} + \omega_s\omega_g\left(I_{G_s} - I_{G_g}\right) \\
&= I_{W_s}\dot{\gamma}\Omega + \left(J_s - I_{G_t} - I_{G_g}\right)\dot{\gamma}\omega_s + J_t\hat{\mathbf{g}}_t^T\,\dot{\boldsymbol{\omega}} + \omega_s\omega_g\left(J_s - J_g\right) + I_{W_s}\omega_g\Omega - 2I_{W_t}\omega_s\dot{\gamma}
\end{aligned} \tag{11.15}$$

$$\begin{aligned}
\dot{\mathbf{H}}\hat{\mathbf{g}}_{\mathbf{g}} &= \omega_s\omega_t\left(I_{W_t} - I_{W_s}\right) - I_{W_s}\omega_t\Omega + I_{W_t}\left(\hat{\mathbf{g}}_g^T\,\dot{\boldsymbol{\omega}} + \ddot{\gamma}\right) \\
&\quad + I_{G_g}\left(\hat{\mathbf{g}}_g^T\,\dot{\boldsymbol{\omega}} + \ddot{\gamma}\right) + \omega_s\omega_t\left(I_{G_t} - I_{G_s}\right) \\
&= J_g\left(\hat{\mathbf{g}}_g^T\,\dot{\boldsymbol{\omega}} + \ddot{\gamma}\right) + \omega_s\omega_t\left(J_t - J_s\right) - I_{W_s}\omega_t\Omega
\end{aligned} \tag{11.16}$$

Further simplifications can be done by solving Eq.11.6 as $\boldsymbol{\omega}_{B/N}$ is known and defined in Eq.11.1. Thus Eq.11.12 can also be rewritten using the new expressions of ω_s, ω_t and ω_g with Eq.11.3 where γ_0 is assumed equal to 0°.

$$\begin{aligned}
\omega_s &= \hat{\mathbf{g}}_s^T\,\boldsymbol{\omega}_{B/N} & \omega_t &= \hat{\mathbf{g}}_t^T\,\boldsymbol{\omega}_{B/N} & \omega_g &= \hat{\mathbf{g}}_g^T\,\boldsymbol{\omega}_{B/N} \\
&= \dot{\phi}\sin(\gamma) & &= \dot{\phi}\cos(\gamma) & &= 0
\end{aligned} \tag{11.17}$$

$$\begin{aligned}
\dot{\omega}_s &= \dot{\gamma}\omega_t + \hat{\mathbf{g}}_s^T\,\dot{\boldsymbol{\omega}} & \dot{\omega}_t &= -\dot{\gamma}\,\omega_s + \hat{\mathbf{g}}_t^T\,\dot{\boldsymbol{\omega}} & \dot{\omega}_g &= \hat{\mathbf{g}}_g^T\,\dot{\boldsymbol{\omega}} \\
&= \dot{\phi}\dot{\gamma}\cos(\gamma) + \ddot{\phi}\sin(\gamma) & &= -\dot{\phi}\dot{\gamma}\sin(\gamma) + \ddot{\phi}\cos(\gamma) & &= 0
\end{aligned} \tag{11.18}$$

Also to express as much as possible the equations with the inertial components of the gimbal plus wheel system, in Eq.11.14 $(-I_{W_t} + I_{W_g})\dot{\gamma}\omega_t$ is added which is possible as $I_{W_t} = I_{W_g}$ because of the wheel geometry. Moreover, because the flywheel is actuated at a constant angular velocity, $\dot{\Omega}$ is null. After simplifications of Eq.11.14-11.15-11.16 using Eq.11.17-11.18, $\dot{\mathbf{H}}_{CMG}$ is obtained.

$$\begin{aligned}\dot{\mathbf{H}}_{CMG} = &\hat{\mathbf{g}}_{\mathbf{s}}\left[(J_s - J_t + J_g)\,\dot{\gamma}\dot{\phi}\cos(\gamma) + J_s\ddot{\phi}\sin(\gamma)\right]\\ &+\hat{\mathbf{g}}_{\mathbf{t}}\left[I_{W_s}\dot{\gamma}\Omega + (J_s - J_t - J_g)\,\dot{\gamma}\dot{\phi}\sin(\gamma) + J_t\ddot{\phi}\cos(\gamma)\right]\\ &+\hat{\mathbf{g}}_{\mathbf{g}}\left[J_g\ddot{\gamma} + \dot{\phi}^2\sin(\gamma)\cos(\gamma)\,(J_t - J_s) - I_{W_s}\Omega\dot{\phi}\cos(\gamma)\right]\end{aligned} \tag{11.19}$$

Moreover, because the angular speed of the wheel Ω is of several order of magnitude higher than the angular speeds $\dot{\gamma}$ and $\dot{\phi}$ of the gimbal and the body respectively. The equation above thus become,

$$\begin{aligned}\dot{\mathbf{H}}_{CMG} = &\hat{\mathbf{g}}_{\mathbf{s}}\left[(J_s - J_t + J_g)\,\dot{\gamma}\dot{\phi}\cos(\gamma) + J_s\ddot{\phi}\sin(\gamma)\right]\\ &+\hat{\mathbf{g}}_{\mathbf{t}}\left[I_{W_s}\dot{\gamma}\Omega\right]\\ &+\hat{\mathbf{g}}_{\mathbf{g}}\left[J_g\ddot{\gamma} - I_{W_s}\Omega\dot{\phi}\cos(\gamma)\right]\end{aligned} \tag{11.20}$$

The torque needed to actuate the gimbal corresponds to the component along the $\hat{\mathbf{g}}_{\mathbf{g}}$-axis of $\dot{\mathbf{H}}_{CMG}$ from Eq.11.20 and defined as τ_{GB}.

$$\tau_{GB} = J_g\ddot{\gamma} - I_{W_s}\Omega\dot{\phi}\cos(\gamma) \tag{11.21}$$

Finally, from the component along the $\hat{\mathbf{g}}_{\mathbf{t}}$-axis of $\dot{\mathbf{H}}_{CMG}$ from Eq.11.20, the expression of the torque generated by the CMG, τ_{CMG}, is given.

$$\tau_{CMG} = I_{W_s}\dot{\gamma}\Omega$$

To couple the dynamic equations of the pendulum with the one of the CMG, the expression above must be transposed from frame G to frame B such that:

$$\begin{aligned}\tau_B &= \tau_{CMG}\sin(\gamma)\hat{\mathbf{b}}_{\mathbf{u}} + \tau_{CMG}\cos(\gamma)\hat{\mathbf{b}}_{\mathbf{v}}\\ &= \tau_{CMG}\sin(\gamma)\hat{\mathbf{b}}_{\mathbf{u}} + \tau_{inv\_pend}\,\hat{\mathbf{b}}_{\mathbf{v}}\end{aligned} \tag{11.22}$$

It is also interesting to note that the bigger the angle of the gimbal orientation is, the higher the angular speed would have to be for a similar torque.

$$\dot{\gamma} = \frac{\tau_{inv\_pend}}{I_{W_s}\Omega\cos(\gamma)} \tag{11.23}$$

11.2 State space matrices and transfer functions of the MIMO blocks

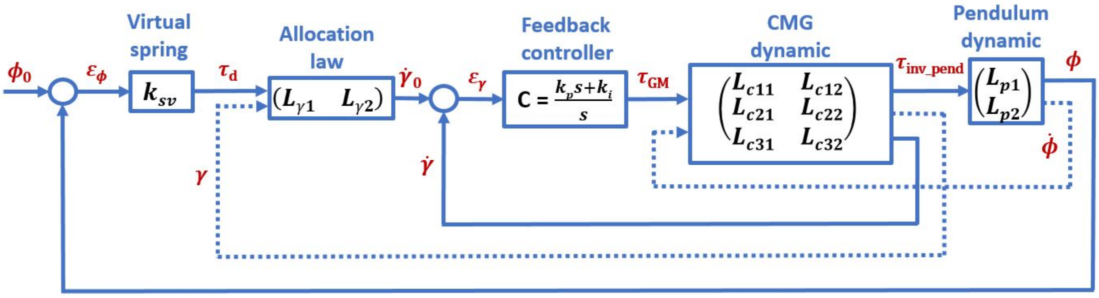

Figure 11.2: Representation of the linearized control diagram with their transfer functions

11.2.1 Linearization of the inverted pendulum block

The equation to linearize is the equation obtained in section 4.1 reminded bellow. The state variables are ϕ and $\dot{\phi}$ and their setpoint are $[0; 0]$. The command u is the torque τ_d.

$$ml^2\ddot{\phi} - mgl\sin(\phi) = \tau_{inv\_pend} - f_\phi\dot{\phi}$$

As reminded in Fig.11.2, this bloc only has one input, u, and two outputs x. The state space matrices and the two transfer functions are given here-under.

$$A = \begin{bmatrix} 0 & 1 \\ g/l & -f_\phi/(m * l^2) \end{bmatrix} \qquad B = \begin{bmatrix} 0 \\ \frac{1}{m*l^2} \end{bmatrix} \qquad C = \begin{bmatrix} 1 & 0 \\ 0 & 1 \end{bmatrix} \qquad D = 0$$

$$L_{p1} = \frac{0.01518}{s^2 + 5.5\,s - 10.11}$$
$$L_{p2} = \frac{0.01518\,s}{s^2 + 5.5\,s - 10.11}$$

11.2.2 Linearization of the CMG block

The equation to linearize is the equation obtained in section 4.1 reminded bellow. The state variables are γ and $\dot{\gamma}$ and their setpoint are $[0; 0]$. The command u is the torque τ_{GM} and the angular speed of the pendulum $\dot{\phi}$.

$$\tau_{GM} = J_g \ddot{\gamma} - I_{W_s} \Omega \dot{\phi} \cos(\gamma)$$

As reminded in Fig.11.2, this bloc has two inputs, u, and three outputs y, $[\tau_d; \gamma; \dot{\gamma}]$. The state space matrices and the six transfer functions are given hereunder.

$$A = \begin{bmatrix} 0 & 1 \\ 0 & 0 \end{bmatrix} \qquad B = \begin{bmatrix} 0 & 0 \\ \frac{1}{J_g} & \frac{I_{W_s}}{J_g}\Omega \end{bmatrix} \qquad C = \begin{bmatrix} 0 & I_{W_s}\Omega \\ 1 & 0 \\ 0 & 1 \end{bmatrix} \qquad D = 0$$

$$L_{c11} = \frac{1676\, s}{s^2} \qquad L_{c12} = \frac{8.422\text{E}04\, s}{s^2}$$
$$L_{c21} = \frac{33.33}{s^2} \qquad L_{c22} = \frac{1676}{s^2}$$
$$L_{c31} = \frac{33.33\, s}{s^2} \qquad L_{c32} = \frac{1676\, s}{s^2}$$

11.2.3 Linearization of the allocation law block

The equation to linearize is the equation obtained in section 4.1 reminded bellow to which the attractive gradient is added. The state variable is $\dot{\gamma}$ and the command u is the torque τ_d and the angular position of the gimbal γ.

$$\dot{\gamma} = \frac{\tau_d}{I_{W_s}\Omega \cos(\gamma)} + k_{att}\,\gamma$$

As reminded in Fig.11.2, this bloc has two inputs, u, and one output x. With its setpoint at 0, the cosine can be rounded to 1 and angular speed is thus proportional to the torque and the angular position.

$$\dot{\gamma} = \frac{1}{I_{W_s}\Omega}\tau_d + k_{att}\,\gamma$$

The transfer function expression is thus straightforward.

$$L_{\gamma 1} = 0.01989 \qquad L_{\gamma 2} = 0.4$$

11.3 Matching of the full-scale and scaled pendulum dynamics

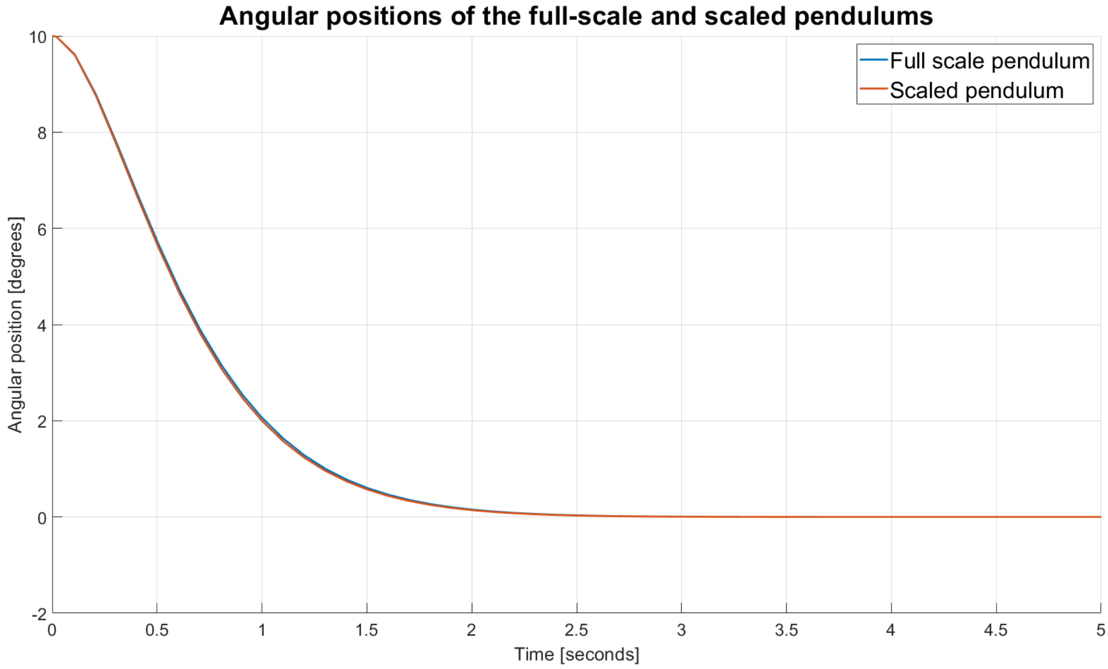

Figure 11.3: Matching of the full-scale and scaled pendulum dynamics.

11.4 Scaled pendulum control under an external perturbation with both sets of scaled parameter

One can see in Fig.11.4 that both versions of the scaled pendulum with the field potential algorithm can handle a perturbation of $0.45\,Nm$ during 0.1 second. The non-minimum of phase behaviour can also be seen in the transient responses of the gimbal angular velocity and generated torque.

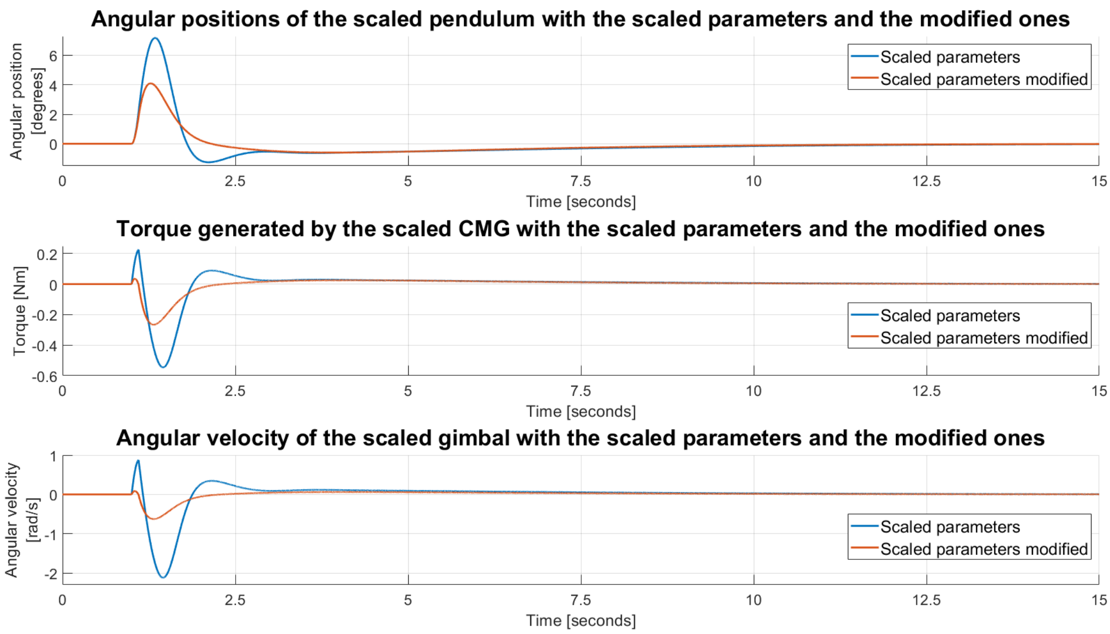

Figure 11.4: Responses of the controllers to an external perturbation for both sets of scaled parameters.

11.5 Free body analysis of the spline shaft

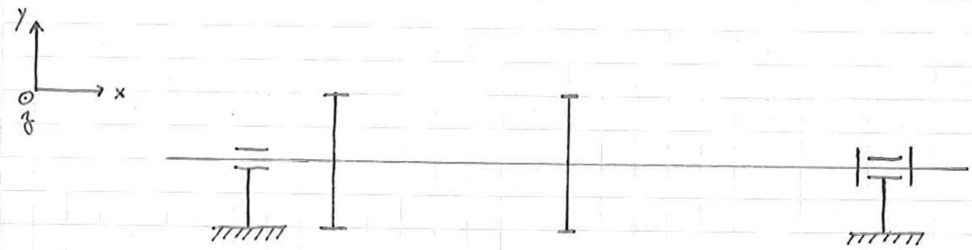

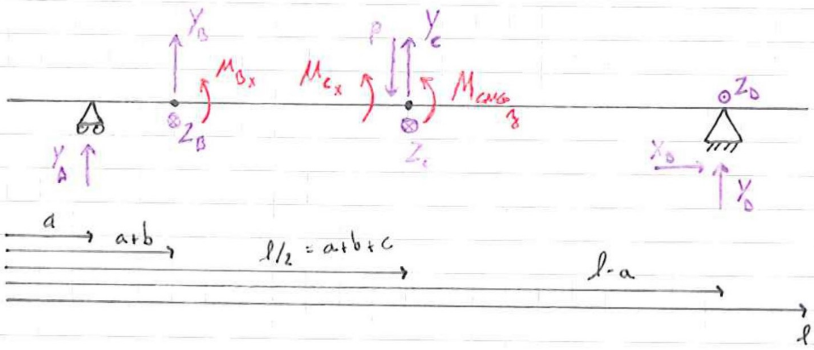

Equilibre des forces :

$$\Sigma F_x = 0 : \quad X_D = 0$$

$$\Sigma F_y = 0 : \quad Y_A + Y_B + Y_C - P + Y_D = 0$$

$$\Sigma F_z = 0 : \quad Z_B + Z_C = Z_D$$

par rapport au point $l/2$

$$\Sigma M_x = 0 : \quad M_{B_x} + M_{C_x} = 0$$

$$\Sigma M_y = 0 : \quad c Z_B + (b+c) Z_D = 0$$

$$\Sigma M_z = 0 : \quad M_{CMG_z} - c Y_B - (b+c) Y_A + (c+b) Y_D = 0$$

Forces internes :

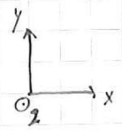

(1)

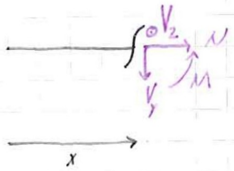

$N = 0$; $V_y = 0$; $V_z = 0$

$M = 0$

(2)

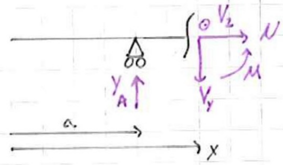

$N = 0$; $V_z = 0$

$V_y = Y_A$

$M_x = 0$; $M_y = 0$; $M_z = (x-a)\, Y_A$

(3)

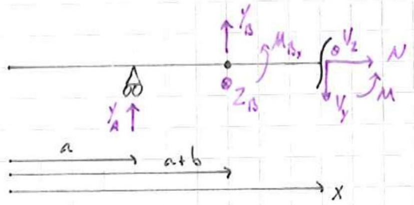

$N = 0$

$V_y = Y_A + Y_B$ $\quad V_z = Z_B$

$M_x = M_{B_x}$

$M_y = (x-a-b)\, Z_B$

$M_z = (x-a)\, Y_A + (x-a-b)\, Y_B$

(4)

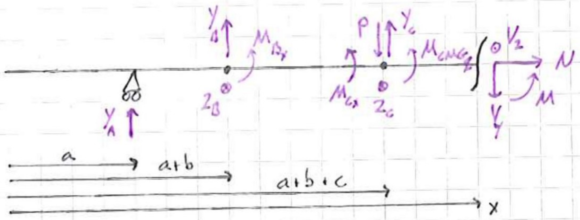

$N = 0$

$V_y = Y_A + Y_B + Y_C - P$

$V_z = Z_C + Z_B$

$M_x = M_{B_x} + M_{C_x}$ $\quad M_y = (x-a-b-c)\, Z_C + (x-a-b)\, Z_B$

$M_z = (x-a-b-c)(Y_C - P) + (x-a-b)\, Y_B + (x-a)\, Y_A - M_{CMG_z}$

(5)

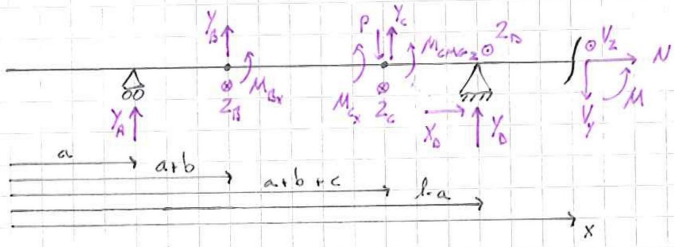

$N = X_D$

$V_y = Y_D + Y_C - P + Y_B + Y_A$

$V_z = Z_C + Z_B - Z_D$

$M_x = M_{B_x} + M_{C_x}$ $\quad M_y = (x-a-b-c)\, Z_C + (x-a-b)\, Z_B - (x-l+a)\, Z_D$

$M_z = (x-a)\, Y_A + (x-a-b)\, Y_B + (x-a-b-c)(Y_C - P) + (x-l+a)\, Y_D - M_{CMG_z}$

11.6 Free body analysis of the gimbal shaft

- Design shaft 2 :

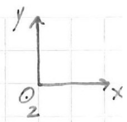

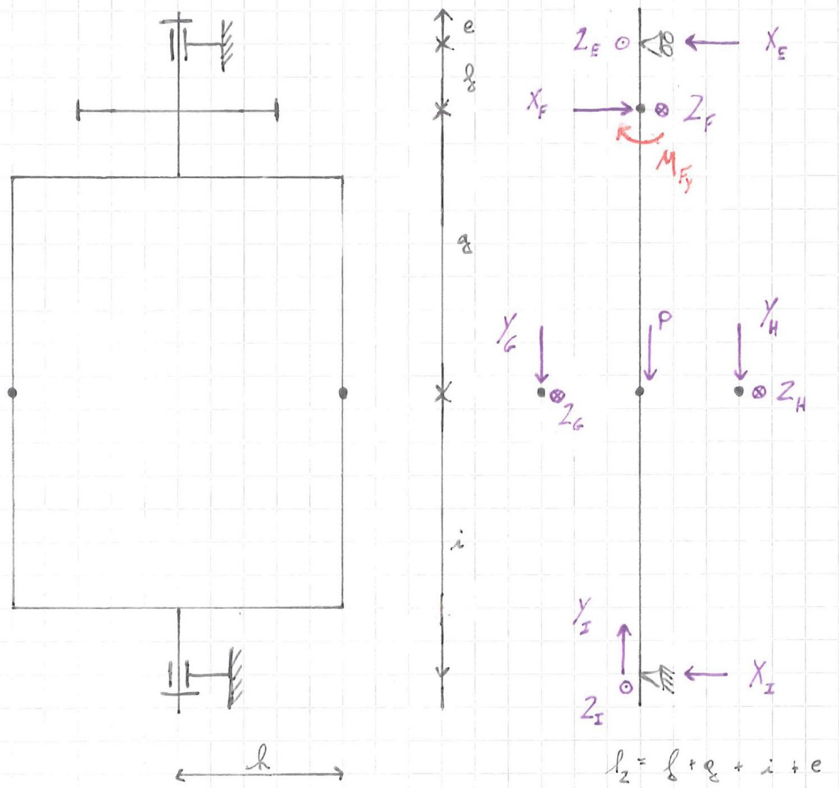

Equilibre des forces et moments:

$\Sigma F_x = 0 : \quad X_F - X_E - X_I = 0$

$\Sigma F_y = 0 : \quad Y_I - Y_G - Y_H - P = 0$

$\Sigma F_z = 0 : \quad Z_F + Z_H + Z_G = Z_E + Z_I$

par rapport au point l_2

$\Sigma M_x = 0 : \quad (i+g) Z_F + i Z_H + i Z_G = (i+g+f) Z_E$

$\Sigma M_y = 0 : \quad h Z_H = M_{F_y} + h Z_G$

$\Sigma M_z = 0 : \quad -h Y_H + h Y_G - (i+g) X_F + (i+g+f) X_e = 0$

Forces internes :

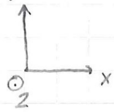

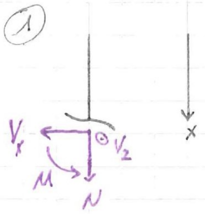

$N = V_x = V_y = 0$

$M = 0$

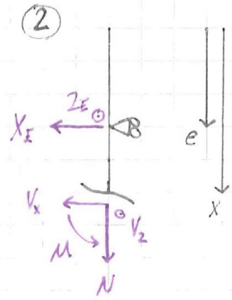

$N = 0 \qquad V_z = -Z_E$

$V_x = -X_E \qquad M_y = 0$

$M_x = -(x-e)Z_E$

$M_z = -(x-e)X_E$

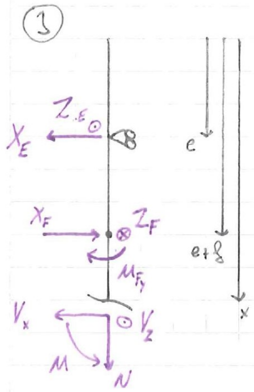

$N = 0 \qquad M_z = (x-e-\ell)X_F - (x-e)X_E$

$V_x = X_F - X_E$

$V_z = Z_F - Z_E$

$M_x = (x-e-\ell)Z_F - (x-e)Z_E$

$M_y = M_{F_y}$

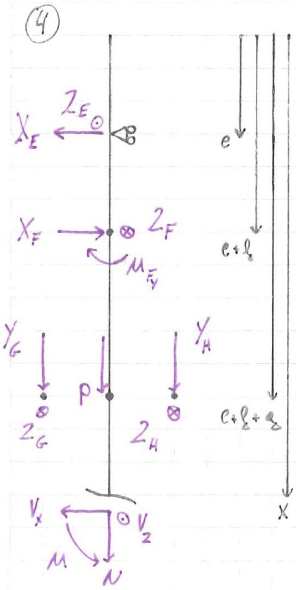

$N = -Y_G - P - Y_H \qquad V_z = Z_H + Z_F + Z_G - Z_E$

$V_x = X_F - X_E$

$M_y = M_{F_y} - \ell Z_H + \ell Z_G$

$M_x = (x-e-\ell)Z_F + (x-e-\ell-g)(Z_H + Z_G) - (x-e)Z_E$

$M_z = \ell Y_H - \ell Y_G + (x-e-\ell)X_F - (x-e)X_E$

11.7 Plans and datasheets of the parts bought

11.7.1 Datasheets of the actuators selected to actuate the spline shaft and its encoder

Brush DC Motors **Portescap**

25GST2R82 Ø 25 mm • Graphite-Copper commutation • 33 mNm

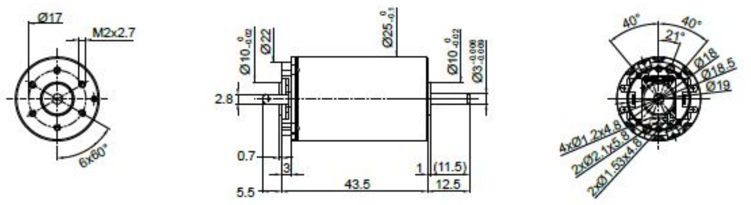

Dimensions in mm.

Electrical Data	Symbol	25GST2R82 •••• .1 228E	230E	216P	216E	Unit
1 Nominal Voltage	V	18	18	24	35	Volt
2 No-Load Speed	n_0	11,125	11,450	10,320	7,850	rpm
3 No-Load Current	I_0	110.0	110.0	70.0	40.0	mA
4 Terminal Resistance	R	1.6	1.3	3.3	12.5	Ω
5 Output Power	$P_{2max.}$	23.8	26.0	24.0	23.3	W
6 Stall Torque	mNm	172 (24.36)	206 (29.18)	160 (22.66)	118 (16.72)	mNm (oz-in)
7 Efficiency	h_{max}	81	83	81	78	%
8 Max Continuous Speed	$n_{e\,max.}$	10,000	10,000	10,000	10,000	rpm
9 Max Continuous Torque	$M_{e\,max.}$	30 (4.68)	33 (4.68)	30 (4.25)	30 (4.25)	mNm (oz-in)
10 Max Continuous Current	$I_{e\,max.}$	2.10	2.30	1.45	0.75	A
11 Back-EMF Constant	k_E	1.60	1.56	2.30	4.40	mV/rpm
12 Torque Constant	k_M	15.30	14.90	22.00	42.00	mNm/A
13 Motor Regulation	R/k^2	6.9	5.9	6.8	7.10	10^3/Nms
14 Friction Torque	T_F	1.68 (0.24)	1.64 (0.24)	1.54 (0.22)	1.68 (0.24)	mNm (oz-in)
15 Rotor Inductance	L	0.10	0.10	0.10	0.80	mH
16 Mechanical Time Constant	τ_m	6.9	5.9	6.8	7.1	ms
17 Rotor Inertia	J	10.00	10.00	10.00	10.00	g-cm^2

General Data			
18 Thermal Resistance (rotor/body)	R_{th1}/R_{th2}	6/13	°C/W
19 Thermal Time Constant (rotor/stator)	t_{w1}/t_{w2}	10/450	S
20 Operating Temperature Range:	motor	-30°C to 85°C (-22°F to 185°F)	°C (°F)
	rotor	100°C (212°F)	°C (°F)
21 Shaft Load Max.:		With ball bearings	
(5 mm. from bearing)	-radial	12.0 (43.2)	N (oz)
	-axial	68 (244.59)	N (oz)
22 Shaft Play:	-radial	<0.03 (0.0012)	mm (inch)
	-axial	0.15 (0.0059)	mm (inch)
23 Weight	g	111 (3.92)	g (oz)
24 Commutation Segment	-	9	segment

Execution Table

Gearbox	Single Shaft	E9	HEDS	MR2
R32	1	2	4	Upon Request
R22HT	24	25	Upon Request	Upon Request

No Load Speed vs. Torque

▶ Motor shaft rotates CW when seen from motor front face when +ve and -ve supply is given to respective terminals.

 107

MR2

Integrated Magnetic Encoder

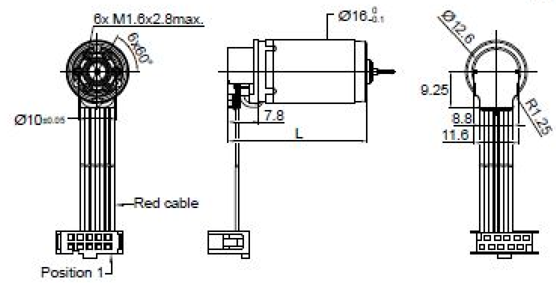

Dimensions in mm.

	Electrical Data		Characteristics @ 22° C	Unit
1	Number of Lines Available		512, 500, 400, 256, 250, 200, 160, 128, 100, 80, 64, 50, 40, 32, 20, 16, 8, 4	LPR
2	Supply Voltage		5 ± 10%	Volt
3	Supply Current	Typical/Maximum	20/25	mA
4	Rise Time		60	ns
5	Fall Time		60	ns
6	Maximum Count Frequency		1.28	MHz
7	Electrical Phase Shift		90 ± 45	degree
8	Duty Cycle		50 ± 15	%
9	Maximum Speed @ 512		37,500	rpm
10	Operating Temperature Range:		-25 to +85 (-13 to +185)	°C (°F)
11	Weight		Varies by motor size. Contact us.	g (oz)

Available on Motor Types*	12G88	13N88	16G88	16N98	17S98	17N98
Length with motor mm (in)	33.8 (1.33)	34.35 (1.35)	35.8 (1.41)	33.2 (1.31)	23.9 (0.94)	31.1 (1.22)

Available on Motor Types*	22N98	25GST
Length with motor mm (in)	39.35 (1.55)	53.9 (2.12)

Output signals:

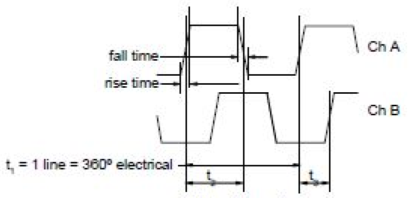

t_2 / t_1 = duty cycle
t_3 = shift phase

Encoder Connections	
1	Motor+
2	Vcc
3	Channel A
4	Channel B
5	GND
6	Motor -
7	Channel Z

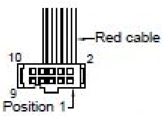

Connector 10 poles type Quickie II or equivalent DIN 41651 A (UL E68080)

11.8 Datasheet of the selected spur gears

Spur Gear

Pressure Angle 20°, Module 0.5 Shaft Bore Configurable Type

RoHS10

Type		M Material	S Surface Treatment	A Accessory
Straight Bore	Straight Bore + Tap			
-	GEABN	EN 1.1191 Equiv.	-	Set Screw (EN 1.7220 Equiv. Black Oxide)
-	GEABB		Black Oxide	
-	GEABG		Electroless Nickel Plating	
GEAHB	GEAB	Free-Cutting Brass Bar	-	
-	GEABS	EN 1.4301 Equiv.	-	Set Screw (EN 1.4301 Equiv.)

Shaft Bore Specifications (Selectable Gear Shapes)

Straight Bore (Shape A, Shape B, Shape K) | Straight Bore + Tap (Shape B, Shape K)

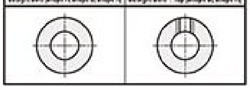

Set Screw is not included in Un-tapped Type products.

Gear Shape

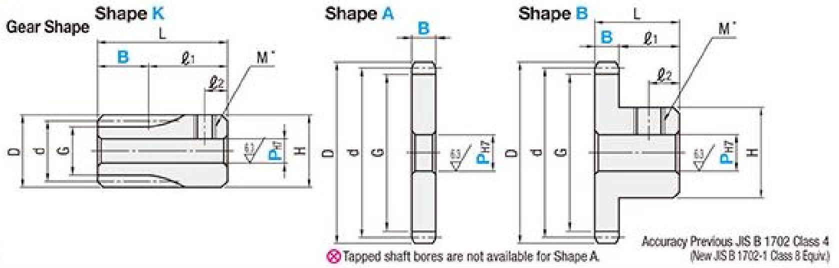

Tapped shaft bores are not available for Shape A.

Accuracy Previous JIS B 1702 Class 4 (New JIS B 1702-1 Class 8 Equiv.)

For alterations on tooth width and hub dimensions, see P.1513.

Part Number Type	Module	Number of Teeth	B	Gears Shape	Shaft Bore Dia. PH7 (1mm Increment) Straight Bore / Straight Bore + Tap	d Reference Dia.	D Tip Dia.	G Root Dia.	H	L	ℓ1	ℓ2	M (Coarse)	*1. Allowable Transmission Force (N·m) Bending Strength EN 1.1191 Equiv.	Free-Cutting Brass Bar	EN 1.4301 Equiv.	Unit Price Straight Bore GEAHB	Straight Bore + Tap GEABN (x1.0) GEABB (x1.1) GEABG (x1.2)	GEAB	GEABS
Straight Bore (Shape A, Shape B, Shape K) GEAHB; Straight Bore + Tap (Shape B, Shape K) GEABN GEABB GEABG GEAB GEABS	0.5	15	8	K	3~5	7.5	8.5	6.25	9	18	10	3	M3	0.72	0.16	0.41				
		16				8	9	6.75						0.79	0.17	0.45				
		18			3~6, 6.35	9	10	7.75	10					0.95	0.21	0.54				
		20				10	11	8.75	11					1.12	0.24	0.64				
		20	3	A	3~5	10	11	8.75	8.5	8				0.42	0.09	0.24				
		24			3~6, 6.35	12	13	10.75	10					0.54	0.12	0.31				
		25				12.5	13.5	11.25						0.58	0.13	0.33				
		26				13	14	11.75						0.61	0.13	0.35				
		28				14	15	12.75						0.68	0.15	0.39				
		30				15	16	13.75						0.74	0.16	0.42				
		32				16	17	14.75						0.80	0.17	0.46				
		35				17.5	18.5	16.25						0.91	0.20	0.52				
		36				18	19	16.75						0.94	0.20	0.54				
		40	2	B		20	21	18.75		7	5	2.5		0.72	0.16	0.41				
		42				21	22	19.75						0.76	0.17	0.43				
		45				22.5	23.5	21.25						0.83	0.18	0.48				
		48				24	25	22.75						0.90	0.20	0.51				
		50				25	26	23.75						0.95	0.21	0.54				
		*52			5~12	26	27	24.75	20					0.99	0.22	-				-
		*60				30	31	28.75						1.18	0.26					
		*70				35	36	33.75						1.42	0.31					
		*80				40	41	38.75						1.65	0.36					
		*100				50	51	48.75						2.13	0.46					
		*120				60	61	58.75						2.59	0.56					

* marked number of teeth is not available for GEABS. Shaft Bore Dia. 6.35 is available.

*1 Allowable Transmission Forces in the table are reference values calculated with prescribed conditions. For conditions, see P. 1498.

Ordering Example

Part Number	-	Number of Teeth	-	B	-	Gear Shape	-	P
GEAB0.5	-	20	-	3	-	B	-	3
GEAHB0.5	-	30	-	3	-	A	-	6
GEABS0.5	-	16	-	8	-	K	-	5

11.8.1 Plan of the damping hinge

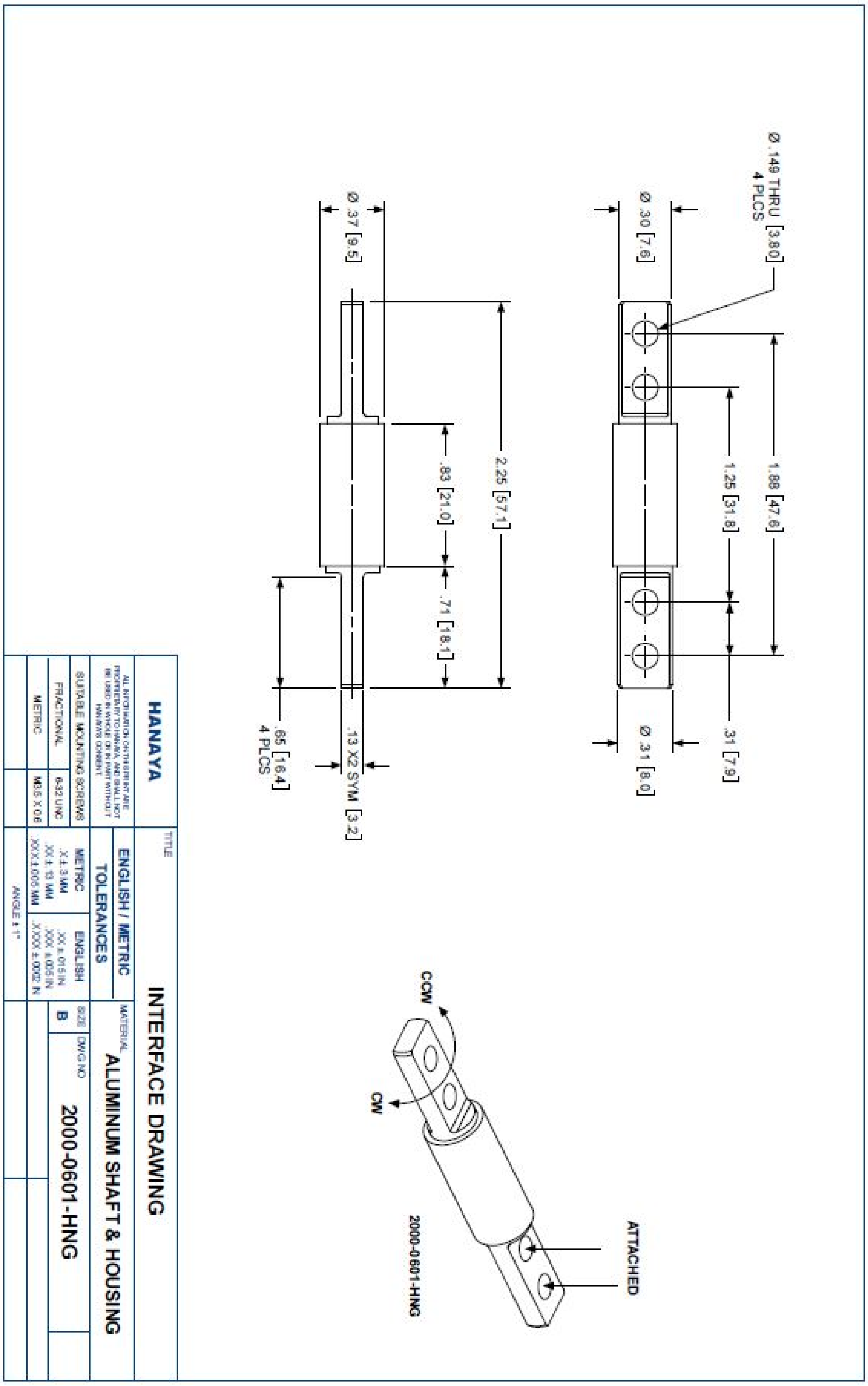

11.8.2 Datasheet and plan of the angle

Équerres en L en aluminium

Pas de rayon, dimension configurable

■Équerres en L en aluminium
- Aucun rayon

RoHS10

Type	Matériau
LRA	EN AW-6063 équiv.

Les plus longues extrusions de L ont des extrémités "comme sciées".

Pour LRA6, R intérieur=6 quand A ou B est de 61mm ou plus. Pour LRA12, R intérieur=12 quand A ou B est de 101mm ou plus.

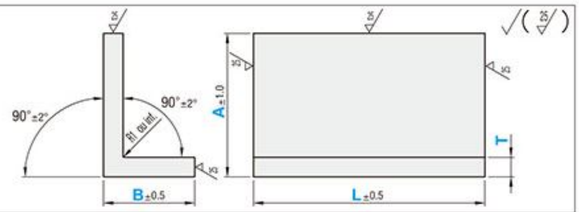

Référence pièce		Tolérance	Incrément de 1mm		
Type	T	T	A	B	L
LRA	3	±0.6	20~40	20~40	20~300
	5		20~50	20~50	
	6	±0.7	20~70	20~70	
	8		20~75	20~75	
	10	±0.8	20~95	20~95	
	12		50~125	50~125	50~300
	14		50~130	50~130	
	18		100~155	100~155	

Ordering Example

Référence pièce	-	A	-	B	-	L
LRA10	-	A85	-	B60	-	L130

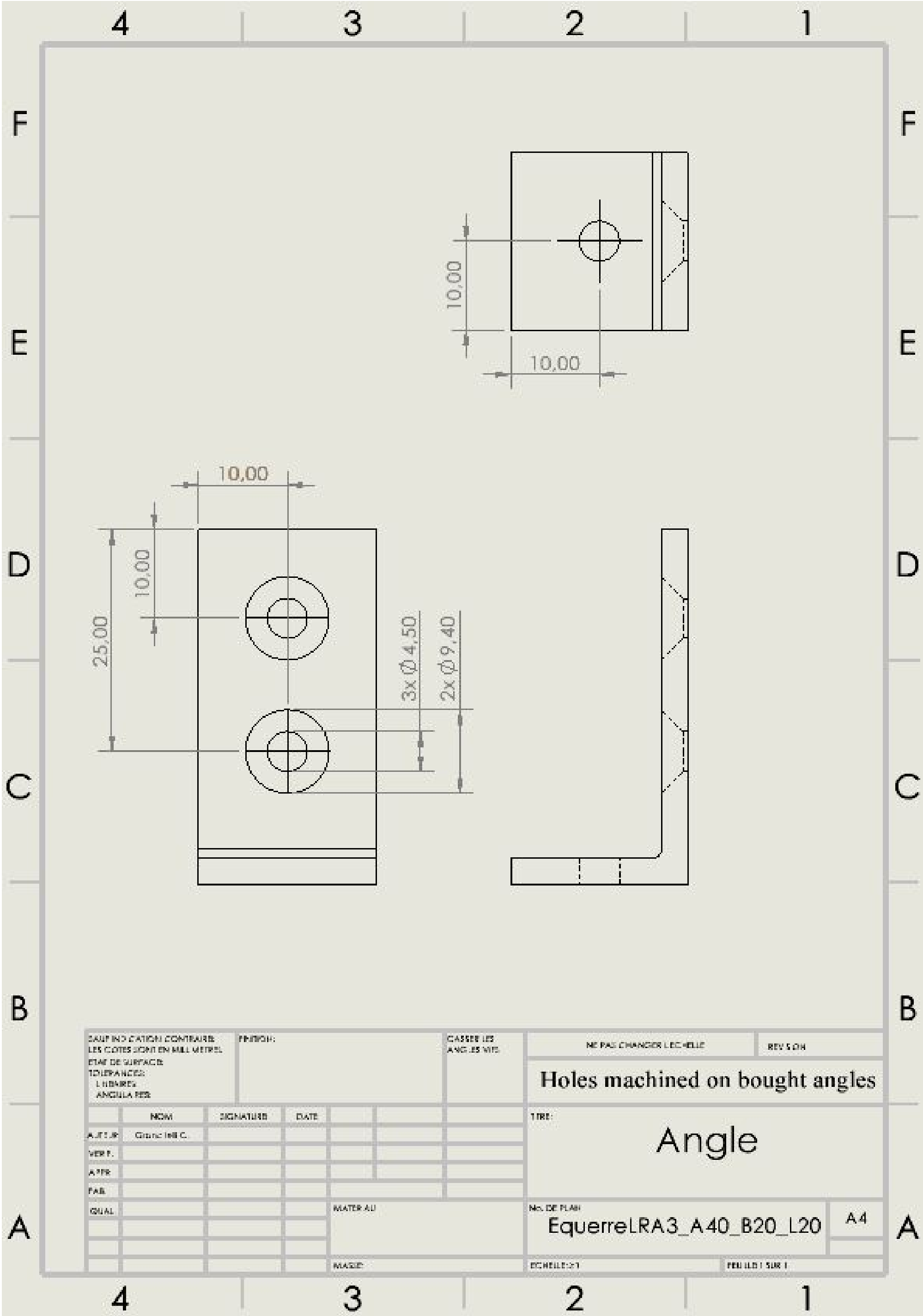
10,00
10,00
10,00
10,00
25,00
3x Ø4,50
2x Ø9,40
Holes machined on bought angles
Angle
EquerreLRA3_A40_B20_L20
A4

11.9 Plans of the different parts to machine

11.9.1 Hinge support

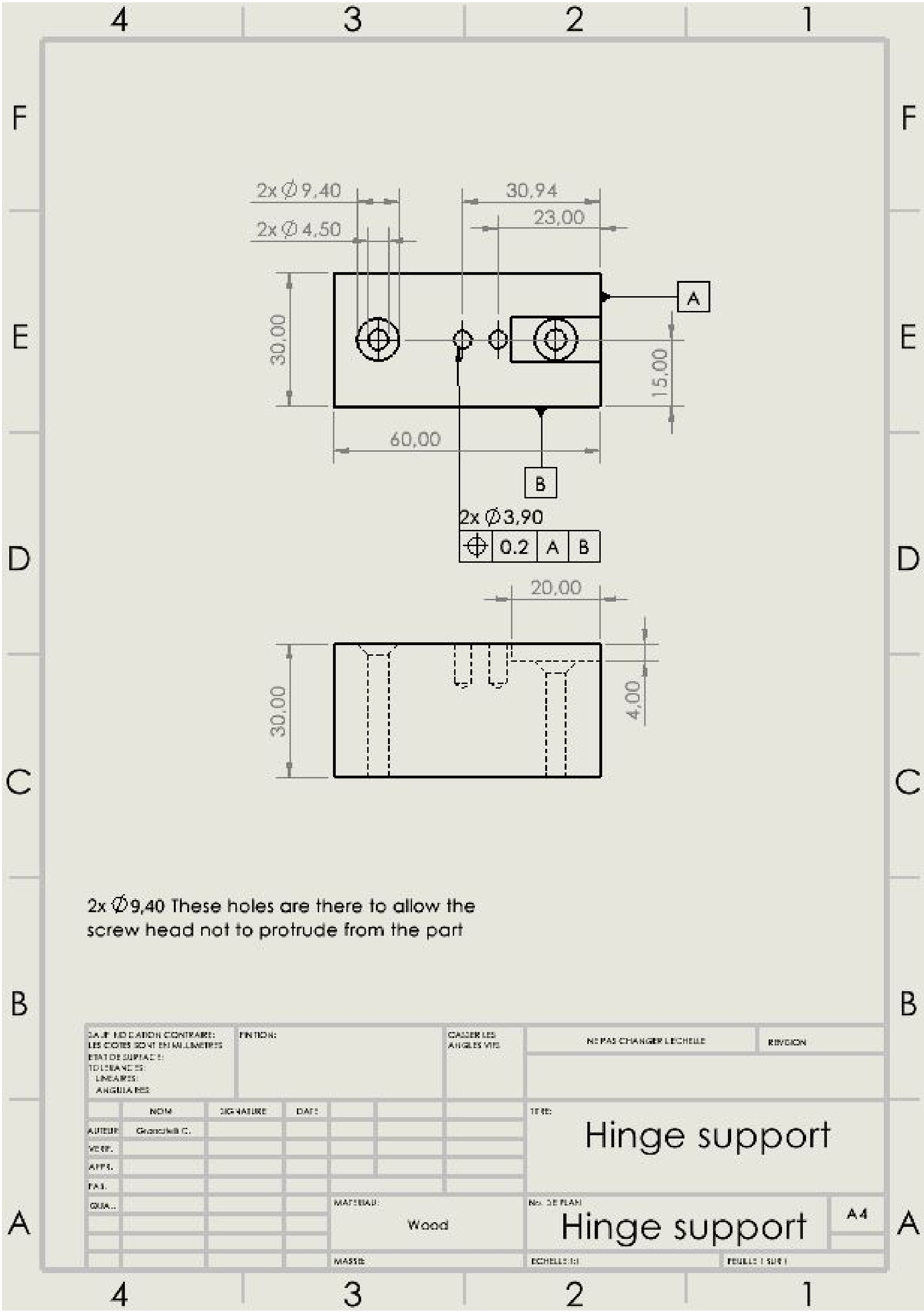

11.9.2 Pendulum

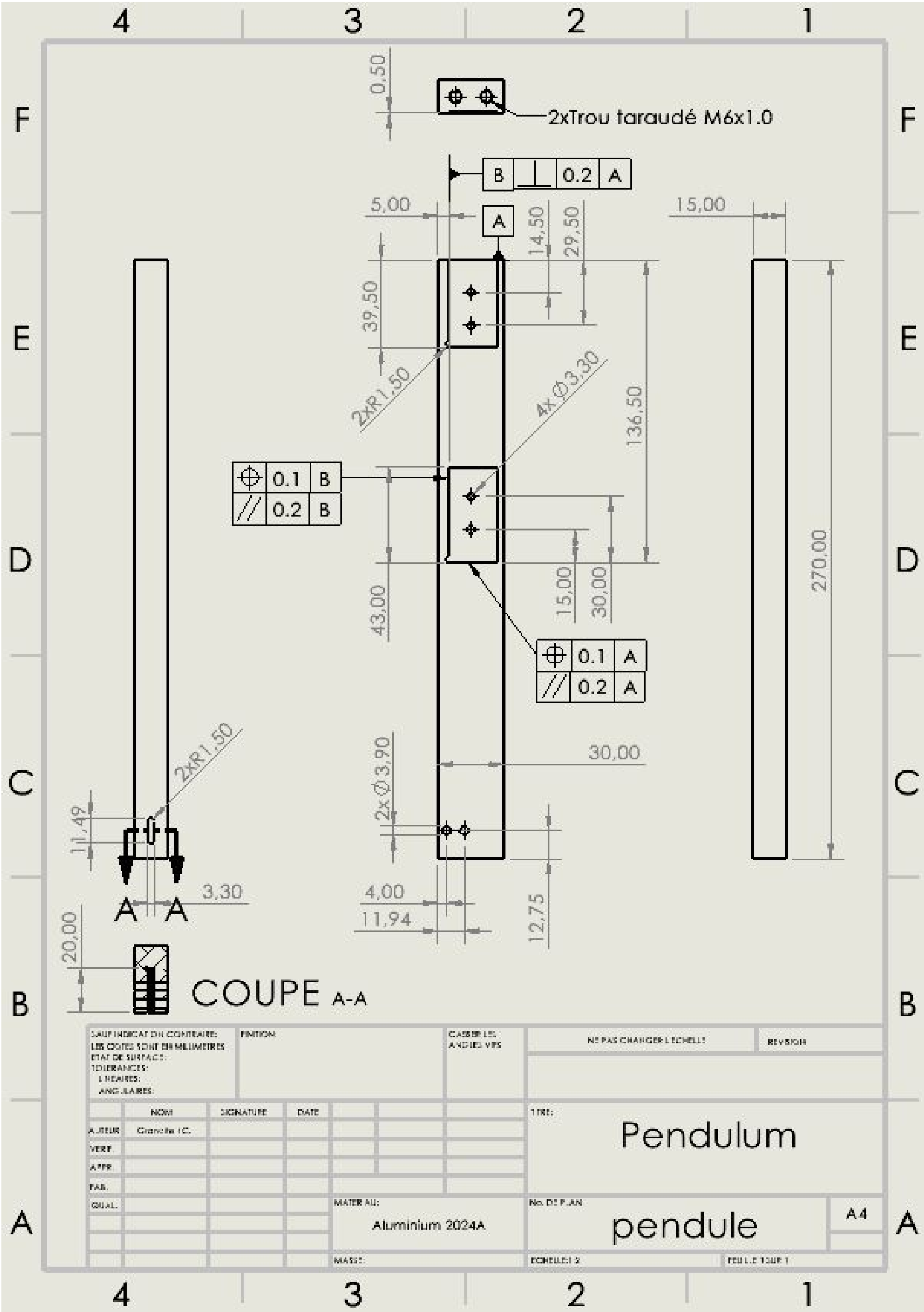

11.9.3 Pendulum fixation bottom

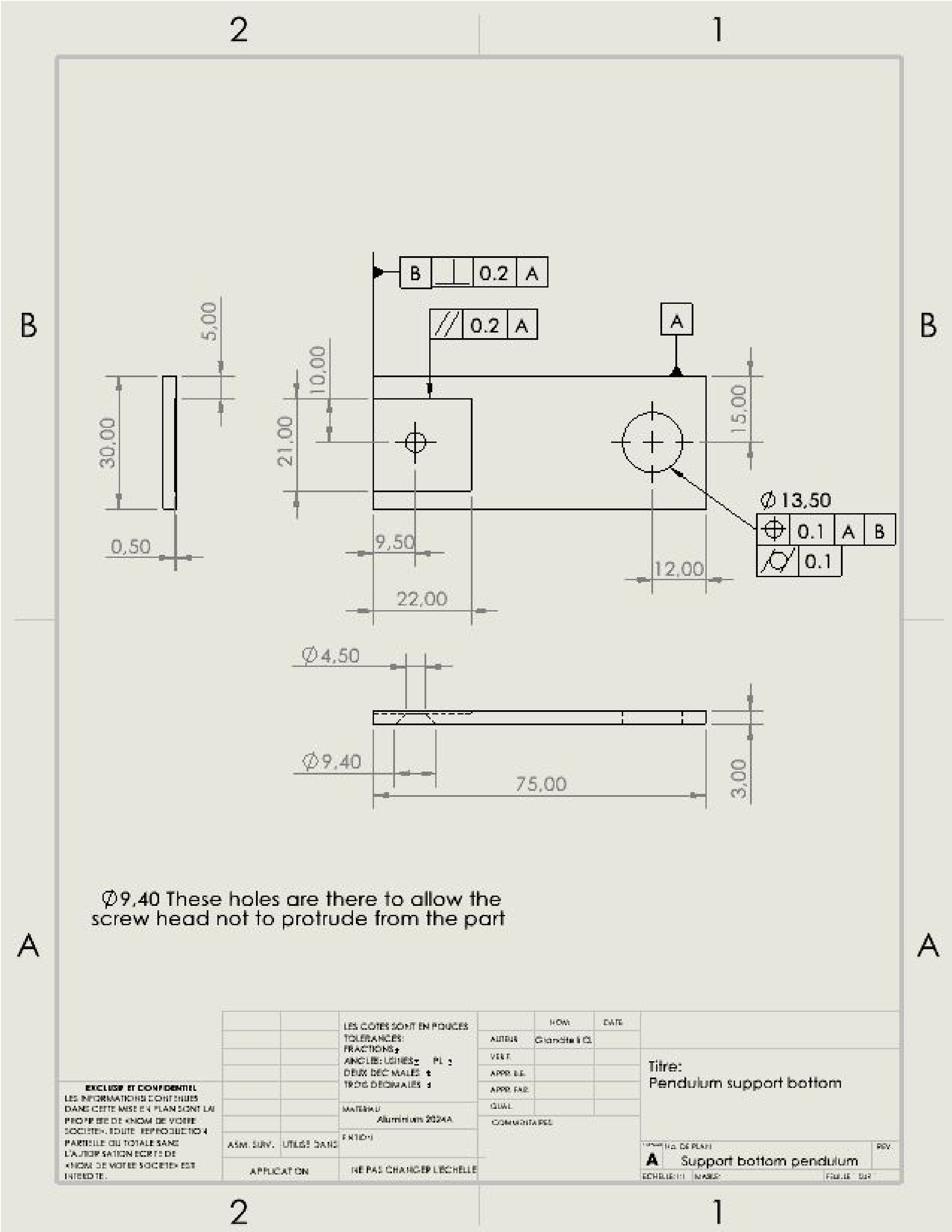

11.9.4 Pendulum fixation top

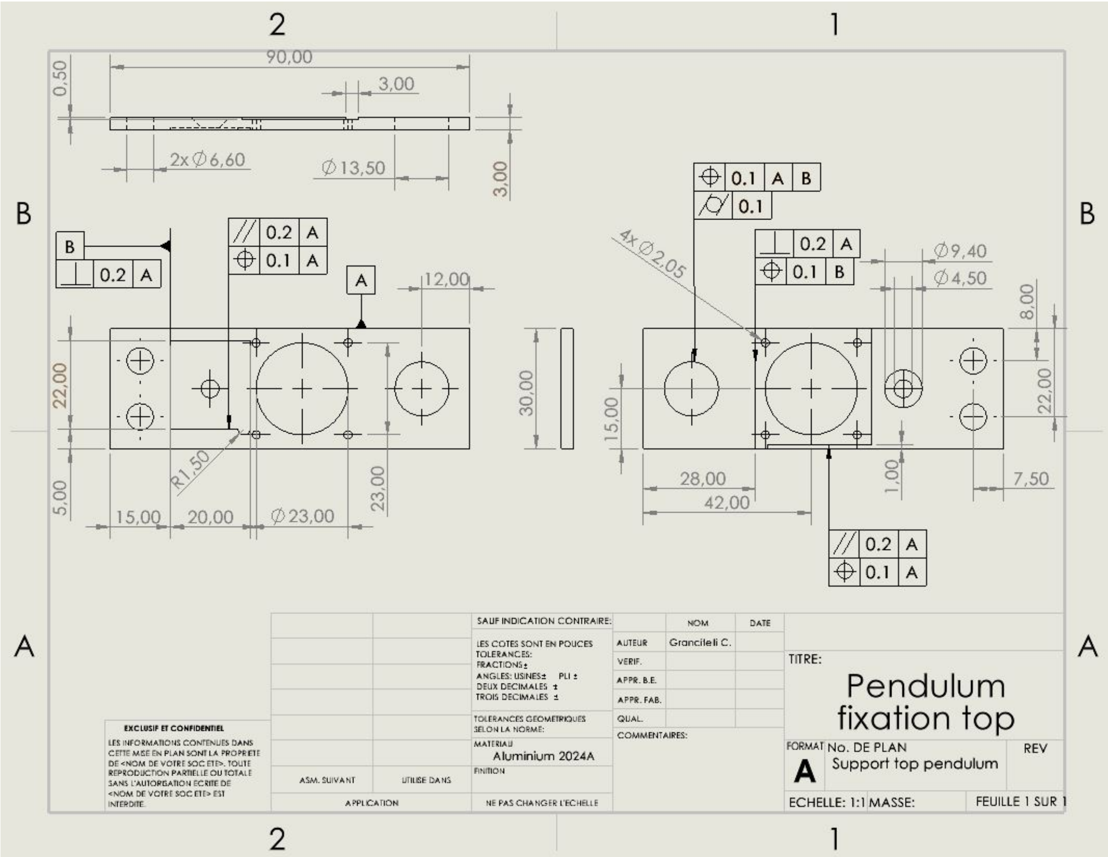

11.9.5 Flywheel

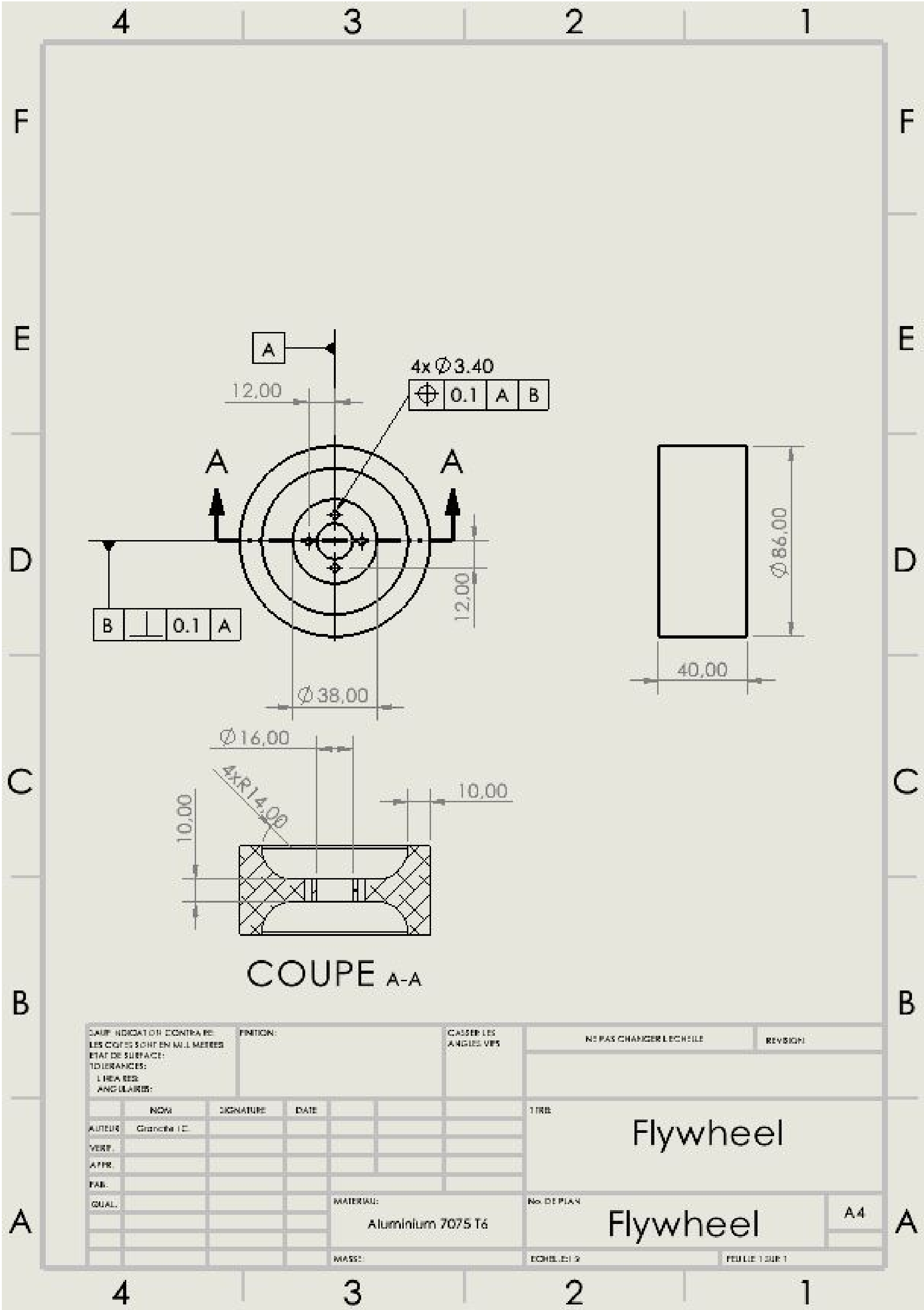

11.9.6 Gimbal support top

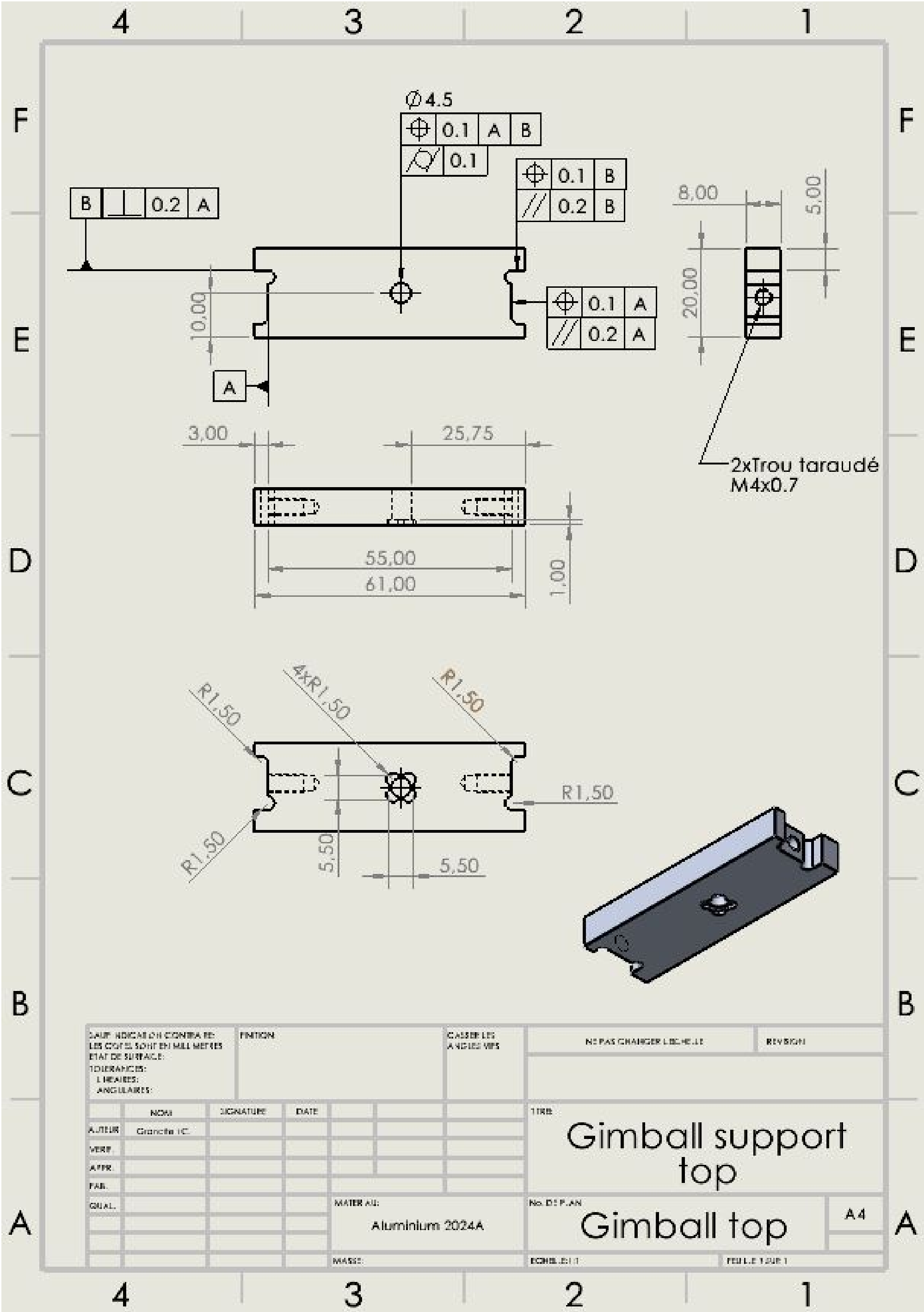

11.9.7 Gimbal support bottom

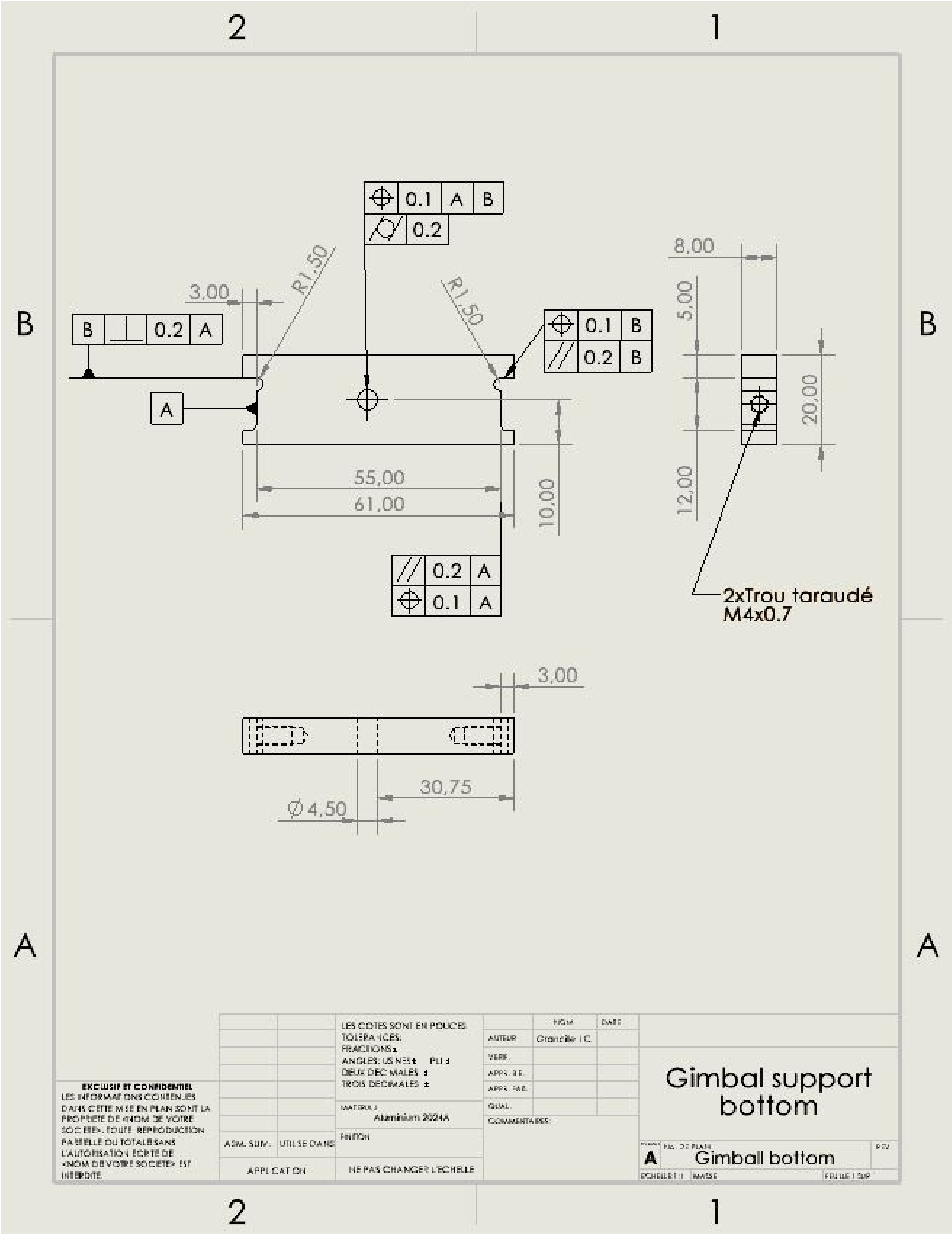

11.9.8 Gimbal lateral support

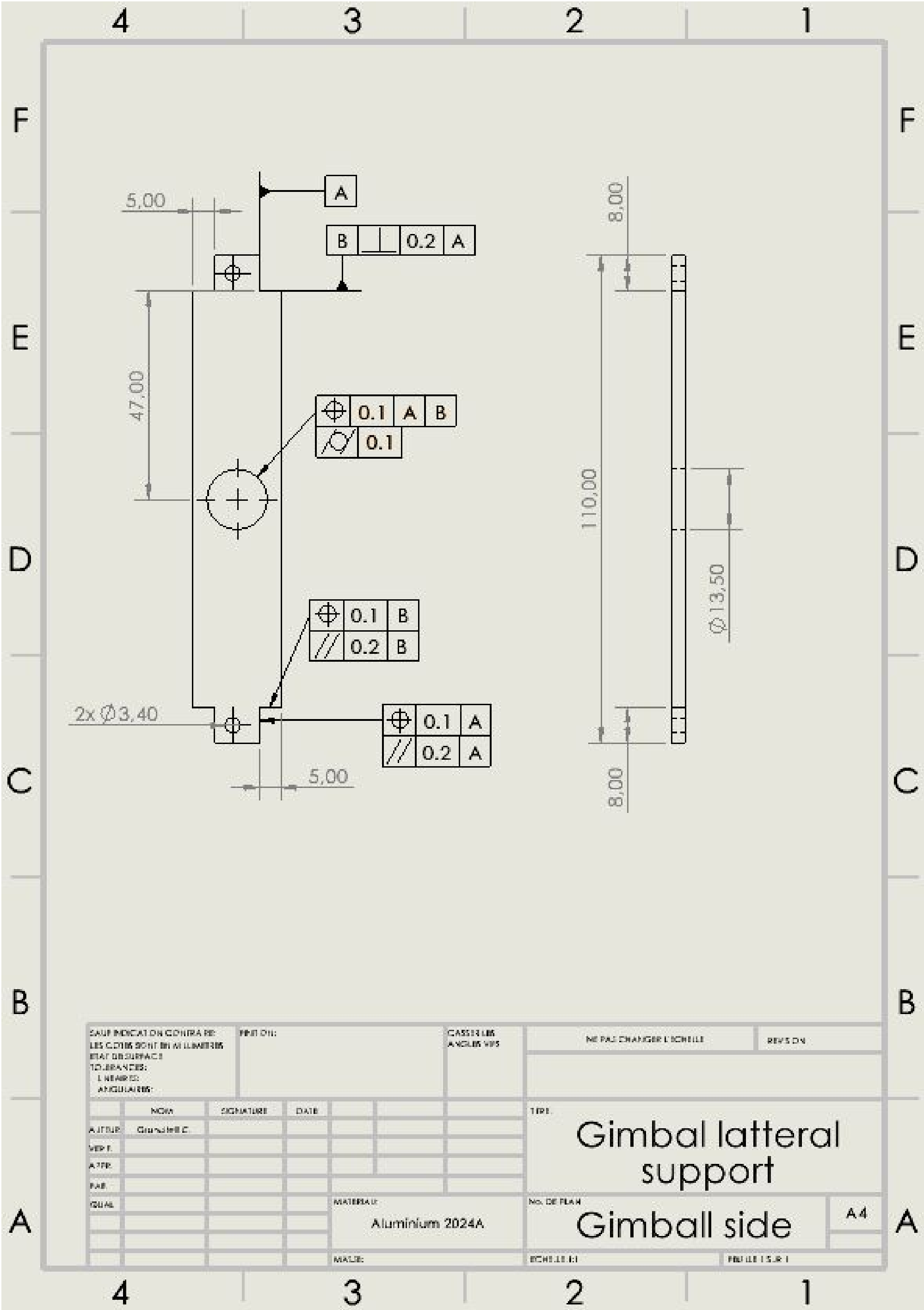

11.9.9 Gimbal support motor

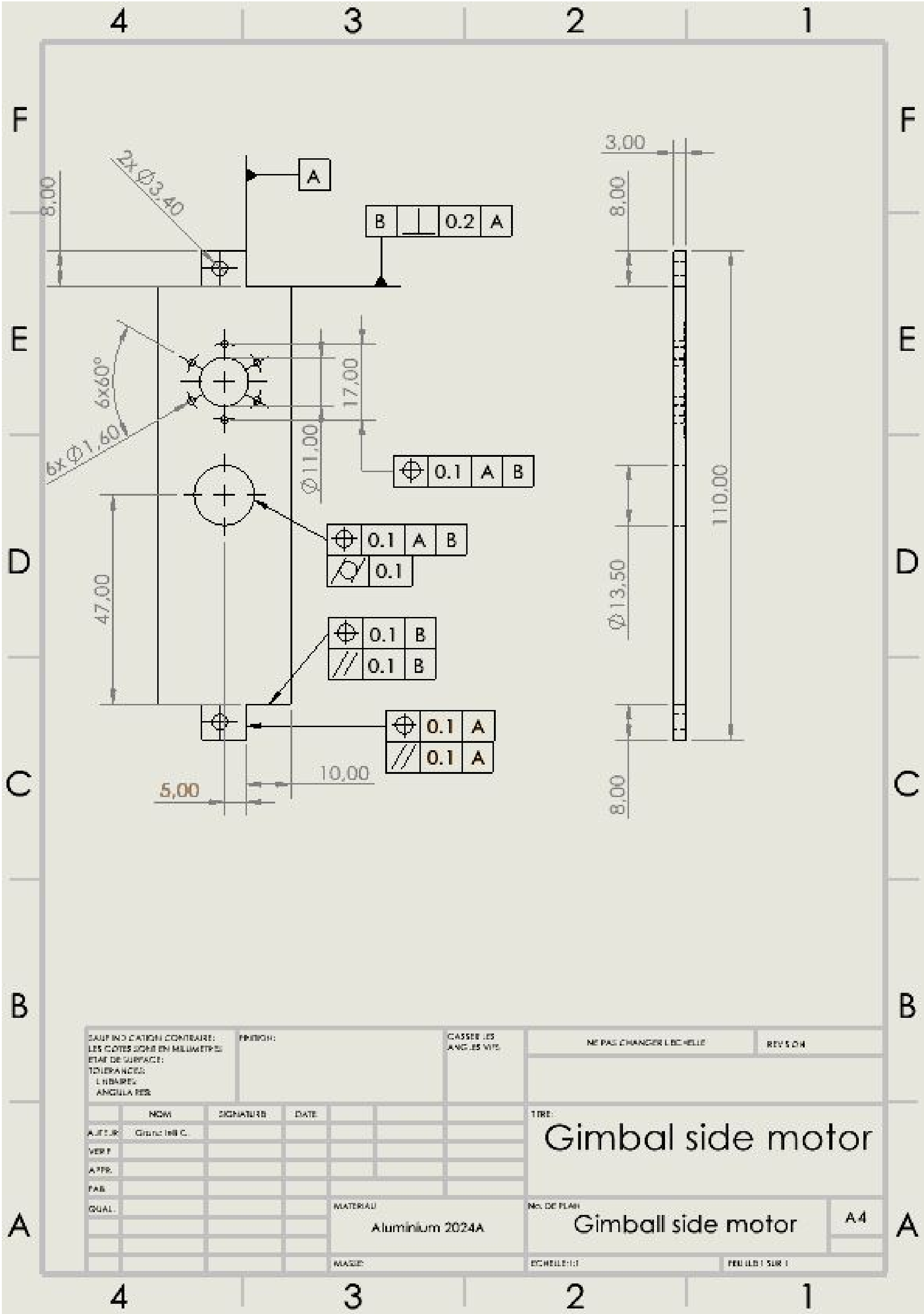

11.9.10 Gimbal shaft

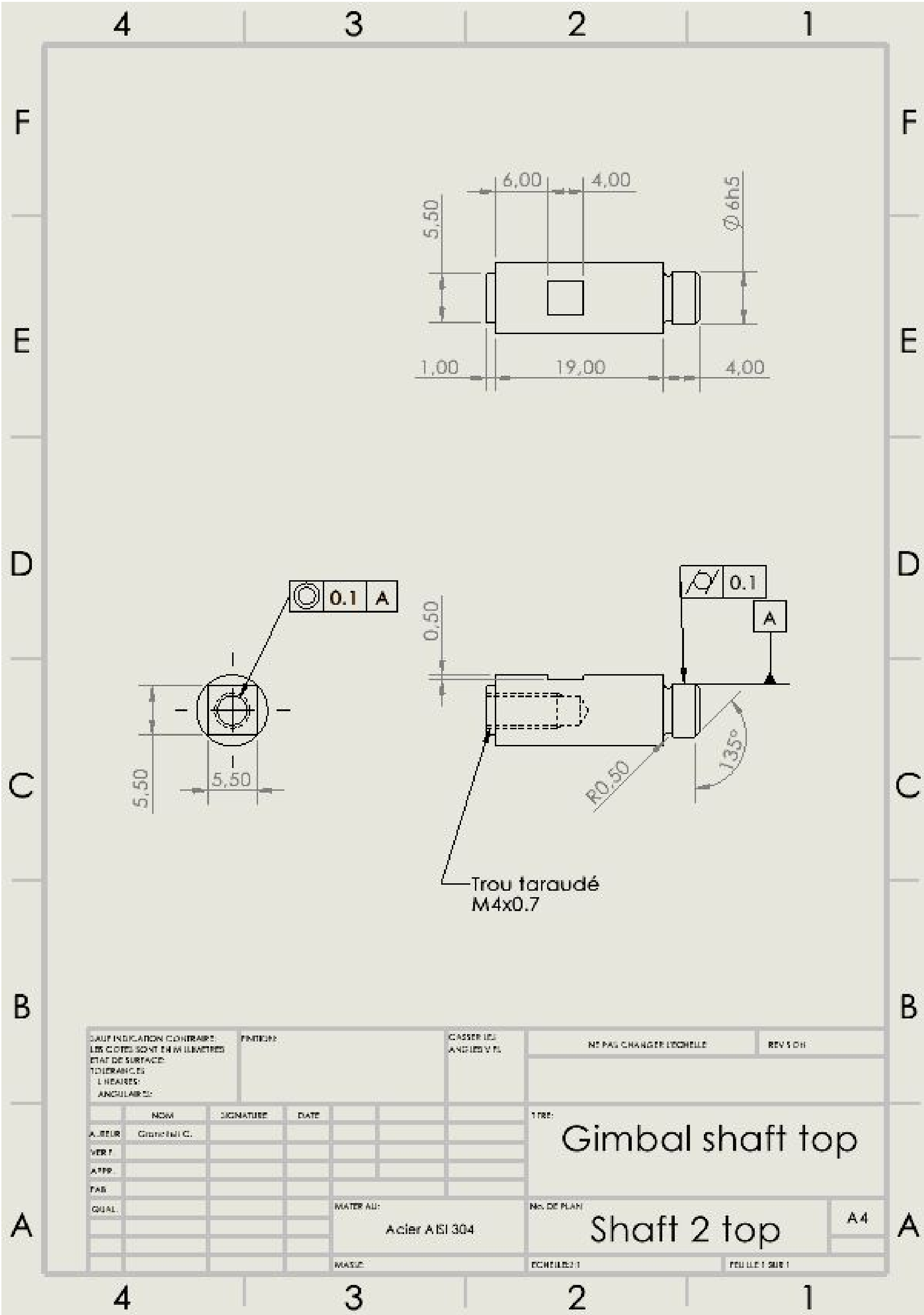

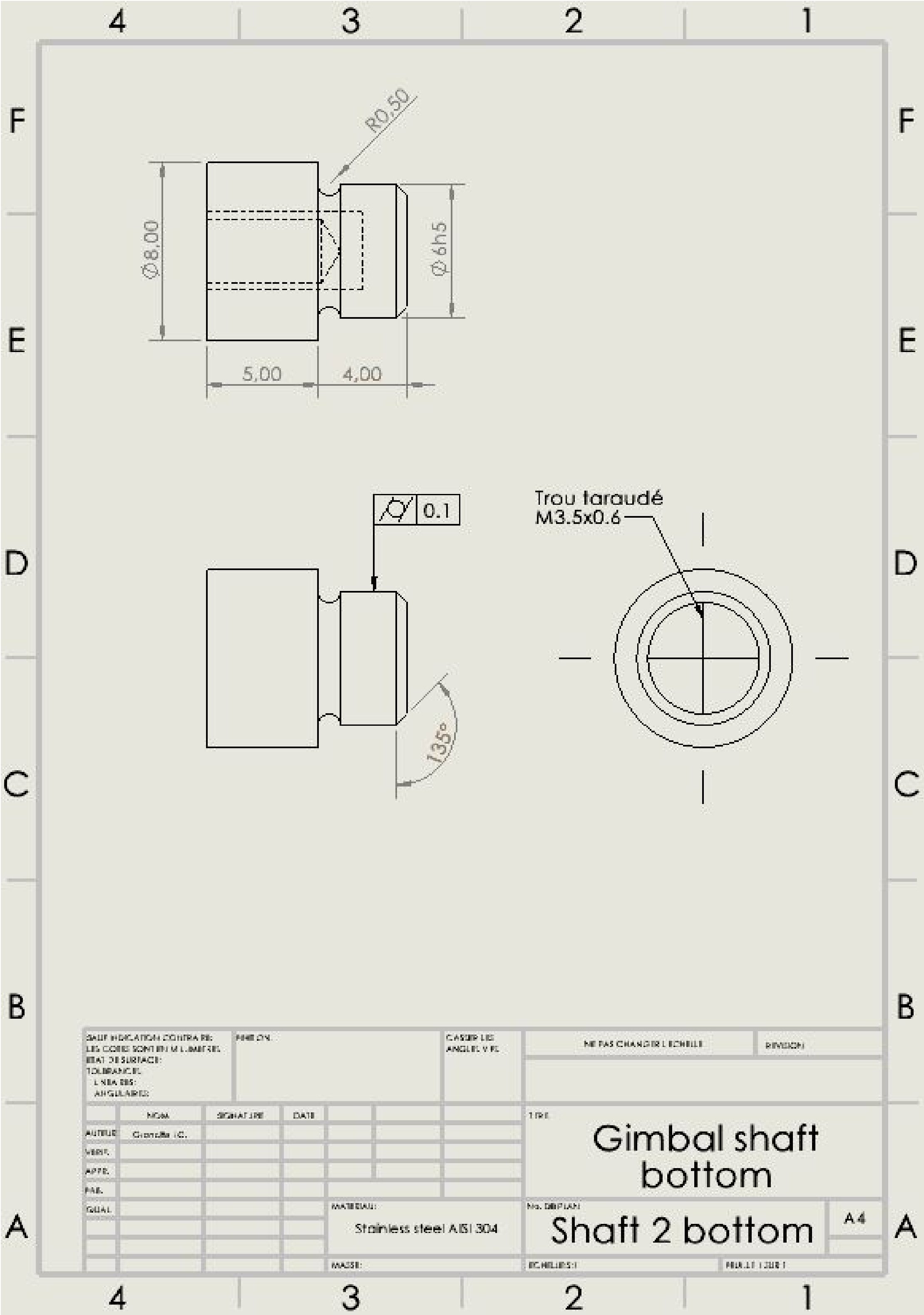
R0,50
Ø8,00
Ø6h5
5,00
4,00
0.1
Trou taraudé
M3.5x0.6
135°
Gimbal shaft
bottom
Shaft 2 bottom
Stainless steel AISI 304
A4

Chapter 12

Bibliography

[1] Ren and Peng. "Research of fall detection and fall prevention technologies: a systematic review". In: *IEEE* (2019).

[2] Heike Vallery. *Gyroscopic balance assistance.* URL: https://www.tudelft.nl/en/3me/about/departments/biomechanical-engineering/research/dbl-delft-biorobotics-lab/gyroscopic-balance-assistance/. (accessed: 16.08.2021).

[3] Hemmatpour; Ferrero; Montrucchio; and Rebaudengo. "A review on fall prediction and prevention system for personal devices: evaluation and experimentatal results". In: *Advances in Human-Computer Interaction* (2019).

[4] Y. Celik; S. Stuart; W.L. Woo; and A. Godfrey. "Gait analysis in neurological populations: Progression in the use of wearables". In: *Medical Engineering & Physics* vol.87 (2021), pp. 9–29. DOI: 10.1016/j.medengphy.2020.11.005.

[5] ReWalk. *What is the ReWalk Exoskeleton?* URL: https://rewalk.com/. (accessed: 19.08.2021).

[6] Neuro-bionics. *Ekso NR.* URL: https://neuro-bionics.eu/fr/ekso-fr/. (accessed: 19.08.2021).

[7] C. Ross Ethier and Craig A. Simmons. *Introductory Biomechanics From Cells to Organisms.* Cambridge texts in Biomedical Engineering. Cambridge University Press, 2018. ISBN: 978-0-521-84112-2.

[8] Oliver Jones. *Walking and gaits.* Nov. 2020. URL: https://teachmeanatomy.info/lower-limb/misc/walking-and-gaits/. (accessed: 08.08.2021).

[9] Felix E. Zajac; Richard R. Neptune; and Steven A. Kautz. "Biomechanics and muscle coordination of human walking Part I: Introduction to concepts, power transfer, dynamics and simulations". In: *Gait and Posture* vol.16 (2002), pp. 215–232. DOI: 10.1016/s0966-6362(02)00068-1.

[10] Marcus G. Pandy and Thomas P. Andriacchi. "Muscle and Joint Function in Human Locomotion". In: *Annual Review of Biomedical Engineering* vol.12 (2010). DOI: 10.1146/annurev-bioeng-070909-105259.

[11] Dennis W. Klima and Ethan Hood. "Gait and Balance Assessment of Older Adults". In: *Current Geriatrics Reports* vol.9 (2020), pp. 154–162. DOI: https://doi.org/10.1007/s13670-020-00327-5.

[12] BTS Bioengineering. *G-WALK*. URL: https://www.btsbioengineering.com/products/g-walk-inertial-motion-system/. (accessed: 19.08.2021).

[13] Move Monitor. *McRoberts*. URL: https://www.mcroberts.nl/products/movemonitor/. (accessed: 19.08.2021).

[14] Honda. *Walking assist*. URL: https://global.honda/innovation/robotics/WalkingAssist.html. (accessed: 19.08.2021).

[15] Jiajia Yao; Takashi Sado; Wenli Wang; Jiawen Gao; Yichao Zhao; Qi Qi; and Mukul Mukherjee. "The Kickstart Walk Assist System for improving balance and walking function in stroke survivors: a feasibility study". In: *Journal of neuroengineering and rehabilitation* (2021). DOI: https://doi.org/10.1186/s12984-020-00795-y.

[16] Airbus. *Control momentum gyroscopes*. URL: https://www.airbus.com/space/spacecraft-equipment/avionics/control-momentum-gyros.html. (accessed: 19.08.2021).

[17] Sea Keeper. *technology*. URL: https://www.seakeeper.com/technology/. (accessed: 19.08.2021).

[18] Space Systems Design Studio. *CONTROL MOMENT GYROSCOPE (CMG) ROVER*. URL: https://www.spacecraftresearch.com/cmg-rover. (accessed: 19.08.2021).

[19] Oliver Russell. *Transparent Girl Walking Silhouette*. URL: https://www.russelloliver.co.uk/silhouette/transparent-girl-walking-silhouette/. (accessed: 12.02.2021).

[20] L. Zonetti; A. Camargo; J. Sartori; D. de Sousa; and L. Nunes. "A demonstration of dry and viscous damping of an oscillating pendulum". In: *European Journal of Physics* vol.20 (1999), pp. 85–88. DOI: 10.1088/0143-0807/20/2/004.

[21] H. Schaub and J. Junkins. *Analytical Mechanics of Space Systems*. 2nd ed. AIAA Education Series. American Institute of Aeronautics and Astronautics, 2009. ISBN: 978-1-60086-721-7.

[22] D. Lemus; J. van Frankenhuyzen; and H. Vallery. “Design and evaluation of a balance assistance control moment gyroscope”. In: *Journal of Mechanisms and Robotics* vol.9 (2017). DOI: 10.1115/1.4037255.

[23] Wikipedia. *Euler-Lagrange equation*. URL: https://en.wikipedia.org/wiki/Euler-Lagrange_equation. (accessed: 19.08.2021).

[24] Herng-Chia Chiu; Hsing-Yi Chang; Lih-Wen Mau; Ti-Kai Lee; and Hong-Wen Liu. “Height, Weight, and Body Mass Index of Elderly Persons in Taiwan”. In: *Journal of Gerontology: Medical Sciences* vol.55A (2000), pp. M684–M690. DOI: 10.1093/gerona/55.11.m684.

[25] Kamal Kothiyal and Samuel Tettey. “Anthropometry for Design for the Elderly”. In: *International Journal of Occupational Safety And Ergonomics* vol.7 (2001), pp. 15–34. DOI: 10.1080/10803548.2001.11076474.

[26] Margaret A. McDowell; Cheryl D. Fryar; Cynthia L. Ogden; and Katherine M. Flegal. “Anthropometric Reference Data for Children and Adults: United States, 2003–2006”. In: *National Center for Health Statistics* vol.7 (2008).

[27] R. Motmans. *Body dimensions of the Belgian population*. 2006. URL: http://www.dinbelg.be/vieillardsmixte.htm. (accessed: 11.08.2021).

[28] Karine Jacquet. *Les hommes et les femmes ont-ils le même centre de gravité ?* 2017. URL: https://www.science-et-vie.com/corps-et-sante/les-hommes-et-les-femmes-ont-ils-le-meme-centre-de-gravite-7864. (accessed: 11.08.2021).

[29] Massimo Cenciarini; Patrick J. Loughlin; Patrick J. Sparto; and Mark S. Redfern. “Stiffness and Damping in Postural Control Increase With Age”. In: *IEEE Transactions On Biomedical Engineering* vol.57 (2010), pp. 267–275. DOI: 10.1109/TBME.2009.2031874.

[30] Wikipedia. *Damping*. 2021. URL: https://en.wikipedia.org/wiki/Damping. (accessed: 13.08.2021).

[31] X. Roser and M. Sghedoni. “Control moment gyroscopes (CMG’s) and their application in future scientific missions”. In: *Proceedings of the 3rd ESA International Conference on Spacecraft Guidance, Navigation and Control Systems*. Noordwijk, the Netherlands, Nov. 2010, pp. 523–528.

[32] Samuel C. Johnson. “Design of a control moment gyroscope attitude actuation system for the attitude control subsystem proving ground”. PhD thesis. Air force institute of technology, Ohio, 2013.

[33] I. R. Nourbakhsh; D. Scaramuzza; and R. Siegwart. *Introduction to autonomous mobile robots*. Intelligent robotics and autonomous agents series. MIT press, 2011. ISBN: 978-0-262-01535-6.

[34] Hyun-Ho Seo; Hyochoong Bang; Yee-Jin Cheon. "Steering law of control moment gyros using artificial potential function approach". In: *Acta Astronautica* vol.157 (2019), pp. 374–389. DOI: 10.1016/j.actaastro.2018.05.054.

[35] Jhelum Chakravorty. "Singularity avoidance in single gimbal CMG using the theory of potential functions". In: (Jul. 2012). DOI: 10.1109/WCICA.2012.6358045.

[36] T. Guojin Z. Qian H. Haibing. "Saturation avoidance method for control moment gyros during spacecraft attitude maneuvers". In: (May 2015), pp. 1796–1801. DOI: 10.1109/CCDC.2015.7162210.

[37] J.D. Muñoz and Frederick Leve. "Artificial potential steering for angular momentum exchange devices". In: *Advances in the Astronautical Sciences* vol.143 (2012), pp. 991–1001.

[38] Bruce D. Miller. "Dynamic Legged Robots for Use in Multiple Regimes: Scaling, Characterization and Design for Multi-Modal Robotic Platforms". In: *The Florida State University College Of Engineering* (2013).

[39] Marc Raibert and Jessica K. Hodgins. "Animation of Dynamic Legged Locomotion". In: *Computer Graphics* vol.25, issue 4 (1991), pp. 349–358. DOI: https://doi.org/10.1145/127719.122755.

[40] Robert C. Juvinall and Kurt M. Marshek. *Machine Component Design*. 5th ed. John Wiley & Sons, Inc., 2012. ISBN: 978-1-118-09226-2.

[41] C. Hazard; A. Ricordeau; C. Corbet. *Méthode active de dessin technique*. Casteilla, 2003. ISBN: 978-2-7135-2399-1.

[42] USAF Samuel C. Johnson 2Lt. "DESIGN OF A CONTROL MOMENT GYROSCOPE ATTITUDE ACTUATION SYSTEM FOR THE ATTITUDE CONTROL SUBSYSTEM PROVING GROUND". In: *AIR FORCE INSTITUTE OF TECHNOLOGY* (2013).

UNIVERSITÉ CATHOLIQUE DE LOUVAIN
École polytechnique de Louvain
Rue Archimède, 1 bte L6.11.01, 1348 Louvain-la-Neuve, Belgique | **www.uclouvain.be/epl**